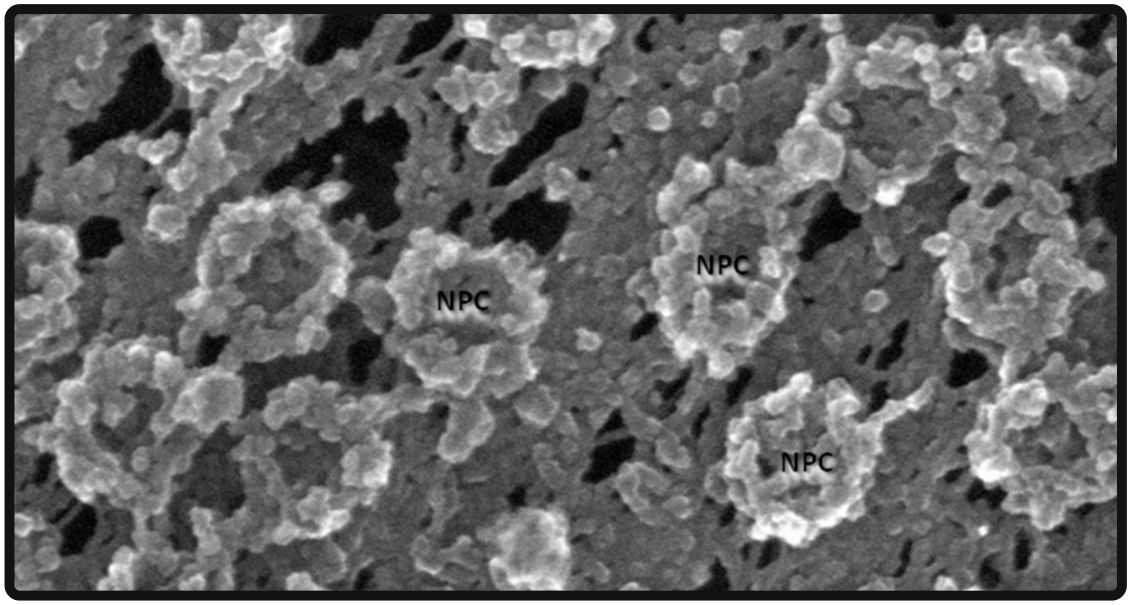

Towards an Artificial Replication of the Nuclear Pore Complex

Achieving Selective Molecular Transport Through Solid State Nanopores

Master's thesis in Nanotechnology

JESPER MEDIN

DEPARTMENT OF CHEMISTRY AND CHEMICAL ENGINEERING

CHALMERS UNIVERSITY OF TECHNOLOGY
Gothenburg, Sweden 2022
www.chalmers.se

Master's thesis 2022

Towards an Artificial Replication of the Nuclear Pore Complex

Achieving Selective Molecular Transport
Through Solid State Nanopores

JESPER MEDIN

CHALMERS
UNIVERSITY OF TECHNOLOGY

Department of Chemistry and Chemical Engineering
Division of Applied Chemistry
Dahlin Research Group
Chalmers University of Technology
Gothenburg, Sweden 2022

Towards an artificial replication of the nuclear pore complex
Achieving selective molecular transport through solid state nanopores
JESPER MEDIN

Supervisor: B. Santoso, Department of Chemistry and Chemical Engineering
Examiner: A. B. Dahlin, Department of Chemistry and Chemical Engineering

Master's Thesis 2022
Department of Chemistry and Chemical Engineering
Division of Applied Chemistry
Dahlin Research Group
Chalmers University of Technology
SE-412 96 Gothenburg
Telephone +46 31 772 1000

Cover: SEM image of a nuclear envelope with several nuclear pore complexes. Image reproduced from Goldberg [1]. Copyright 2017. Published by Elsevier Ltd.

Typeset in LaTeX
Gothenburg, Sweden 2022

Towards an artificial replication of the nuclear pore complex
Achieving selective molecular transport through solid state nanopores
JESPER MEDIN
Department of Chemistry and Chemical Engineering
Chalmers University of Technology

Abstract

The nuclear pore complex acts as a selective barrier between the nucleus and the cytoplasm of a eukaryotic cell, allowing for selective and active transport of biomolecules across the nuclear envelope. The selectivity of the transport is facilitated by shuttle proteins that are able to bind specifically to cargo proteins, actively guide them through the nuclear envelope, and release them on the other side.

In this work, an artificial replication of the nuclear transport using poly(methacrylic acid) (PMAA) and poly(N-(2-hydroxyethyl) acrylamide) (PHEAA) as a shuttle and barrier respectively was developed to allow for selective transport of macromolecules through solid-state nanopores. PHEAA was grafted from gold by atom transfer radical polymerisation (ATRP). In water, hydrated "polymer brushes" have been reported to serve as entropic barriers against proteins and other macromolecules.

Intermolecular interaction studies using surface plasmon resonance (SPR) and quartz crystal microbalance dissipation (QCM-D) showed that PMAA was able to interact with PHEAA and insert itself into the brush. Further, the interaction was shown to be controllable by changing the pH. This changed PMAA from a protonated state where it could continuously form and break hydrogen bonds with the PHEAA brush, to a charged state where it could not.

Fluorescence imaging showed that PMAA with covalently attached fluorescent cargo could undergo pH dependent diffusion through nanopores covered with PHEAA. At a pH of 7.5 PMAA was charged and would be blocked by the polymer brush. At a pH of 4.0 PMAA was protonated and would diffuse through the nanopore and carry the fluorescence cargo with it to the other side. This demonstrated that the artificial system could mimic the key features of the nuclear pore complex and selectively transport molecular cargo across a solid state nanopore.

Keywords: artificial biology, nanotechnology, polymer brushes, soft matter

Acknowledgements

I would first like to thank my supervisor Bagus Santoso who has provided valuable guidance and suggestions for both the experimental work and the writing of this thesis through our meetings. I would also like to thank Gustav Ferrand-Drake del Castillo, John Andersson and Justas Svirelis who have always provided interesting discussions and provided insight in the research I was conducting. I would also like to give a big thanks to Julia Järlebark and Radhika Vattikunta, who helped me in fabricating the nanostructures used in the experimental work.

Furthermore, I would like to thank my examiner Andreas Dahlin for providing helpful discussions and for sharing insights on how to advance the project, and how to take the project beyond the scope of the master's thesis. I would finally like to thank the Excellence Initiative Nano steering group for giving me a chance to continue my research in this field as an Excellence PhD student.

I thank you all for this spring, and I look forward to continuing working with you.

Jesper Medin, Gothenburg, June 2022

List of Acronyms

Below is the list of acronyms that have been used throughout this thesis listed in alphabetical order:

ARGET	Activators Regenerated by Electron Transfer
ATRP	Atom Transfer Radical Polymerisation
BSA	Bovine Serum Albumin
CAS	Cellular Apoptosis Susceptibility Protein
CRP	Controlled Radical Polymerisation
DMSO	Dimethyl Sulfoxide
FG	Phenylalanine-Glycine
FG-Nups	Nucleoporins with Phenylalanine-Glycine repeats
FTIR	Fourier Transform Infrared Specroscopy
GDP	Guanosine Diphosphate
GTP	Guanosine Triphosphate
Im_{α}	Importin α
Im_{β}	Importin β
$Im_{\alpha\beta}$	Im_{α}-Im_{β} Heterodimer
Kaps	Karyopherins
NLS	Nuclear Localisation Sequence
NPC	Nuclear Pore Complex
Nups	Nucleoporins
PAAM	poly(acrylamide)
PBS	Phosphate Buffered Saline
PDI	Polydispersity Index
PEG	Poly(ethylene glycol)
PMAA	poly(methacrylic acid)
PNIPAM	poly(N-isopropylacrylamide)
PHEAA	poly(N-(2-hydroxyethyl)acrylamide)
QCM	Quartz Crystal Microbalance
QCM-D	QCM with Dissipation Monitoring
Ran	Ras-related Nuclear Protein
RanGDP	GDP-bound Ran
RanGTP	GTP-bound Ran
SI	Surface-initiated
SPR	Surface Plasmon Resonance
TIR	Total Internal Reflection

Nomenclature

Below is the nomenclature of a select few important variables that have been used throughout this thesis in chronological order.

Parameters

k_{act}	ATRP activation rate constant
k_{deact}	ATRP deactivation rate constant
k_t	ATRP termination rate constant
R_p	Rate of ATRP
Δn_{eff}	Effective change in refractive index
δ	Decay length of the evanescent field
$\Delta\Theta_{\text{SPR}}$	Change in SPR angle
$\Delta\Theta^*_{\text{SPR}}$	Compensated change in SPR angle
$\Delta\Theta_{\text{TIR}}$	Change in TIR angle
Δf	Change in oscillation frequency
ΔD	Change in energy dissipation
Δ_n	Penetration depth of QCM for n:th overtone
γ	Fractional surface coverage
Γ	Total surface coverage
Γ_{max}	Surface saturation limit
t	time
κ_{on}	Association rate constant
κ_{off}	Dissociation rate constant
C_0	Analyte bulk concentration
KD	Affinity constant

Contents

List of Figures

List of Tables

1

Introduction

Cell are highly advanced microreactors that serve as the fundamental building blocks of all known living organisms. They have selectively evolved mechanisms over millions of years to take on specialised functions. These specialisations have fascinated biologists and researchers since long ago and attempts to recreate these specialised functions with synthetic analogues have long been desired [2], and creating artificial cells allows us to create a simplified model of a living system. However, as natural cells are quite different from each other it would be impossible to mimic every specific function. Therefore, an artificial cell should be tailored to fulfil the specialised function it should replicate. When creating an artificial system, it is simpler to subdivide functions onto several systems, rather than create a large complex system. In this thesis a synthetic structure that resembles the nuclear membrane will be investigated and the functionality is the nuclear transport that shuttles biomolecules across the membrane and into the nucleus.

All structural elements of the cell can be seen as nanoscale compartments that each require its own chemical environment. A significant difference between the interior of a cells and solutions is the crowded environment inside the former. About 30% of the volume is occupied by biomolecules, and the ratios of these biomolecules has to be carefully controlled for the cell to maintain its biological activity [3]. The cell has evolved highly sophisticated methods to shuttle these biomolecules to where they need to be. Access to the nucleus of the cell, which is the inner engine of the microreactor, is regulated by the nuclear envelope. It is a double membrane that encloses the nuclear genome of a eukaryotic cell and separates it from the surrounding cytoplasm containing the other structural elements of the cell [4]. Having this nuclear membrane is a unique feature of eukaryotic cells.

However, it is important that biomolecules such as nuclear proteins and RNA are still able to move through the nuclear envelope to fulfil their specialised function. This is regulated by the numerous nuclear pores that perforate the nuclear envelope. They fulfil the role of a transport route, and are fully permeable to small molecules and proteins, but form a selective barrier against movement of large biomolecules [5]. Creating an artificial solid state construct that mimics the diffusion selectivity and efficiency of the nuclear pores has long been desired. Our hope is that the results presented in this thesis helps bring us one step closer to that goal.

1.1 Selective Nuclear Transport

The specialised function of the nuclear envelope is to allow a small selection of biomolecules to pass through the nuclear membrane, while acting as a passive diffusion barrier for those that are not supposed to cross over the nuclear membrane. The high selectivity is offered by a large proteinaceous assembly called the nuclear pore complex (NPC). The NPC is composed of intrinsically disordered scaffold proteins known as nucleoporins (Nups). These proteins form a highly flexible and amorphous mesh-like network inside the inner channel of the NPC. The intrinsic disorder arise from phenylalanine-glycine (FG) repeats nucleoporins (FG-Nups) that are proposed to interconnect the FG-Nups. This interconnection is proposed to both dictate the size exclusion limit of the permeability of the NPC as well as its selective transport capabilities [6, 7, 8, 9]. Smaller molecules, such as water, ions, and sugars, are able to freely move through the "gaps" of the Nups meshwork unhindered, while larger macromolecules will be stopped from entering the NPC [10]. The NPC has a large enough channel to allow proteins smaller than 40 kDa to passively diffuse through it [11], but studies that have shown that proteins up to a size of 230 kDa are able to passively diffuse through the NPC on a time scale of many hours [12, 13].

Figure 1.1 shows a schematic illustration of the structural elements of the NPC. It covers the entirety of the nuclear pores that perforate the nuclear envelope and is on average 100 nm wide. The general architecture of the nuclear pore complex is the same for all eukaryotes, with some differences in the mass and size from the expression of different nucleoporins between species [9]. The main interest in this thesis was the diffusion barrier inside the central pore of the NPC.

1.1.1 Shuttle-Cargo Translocation

While small molecules can move through the diffusion barrier by passive diffusion, any larger macromolecules have to undergo an active transport. In order to achieve this the macromolecules have to be able to interact with the FG-Nups or be attached to another macromolecule that is able to [10]. The bidirectional movement of cargo protein and RNA across the nuclear envelope is guided by chaperone proteins (shuttles) called karyopherins (Kaps), with subdivisions importins and exportins [8].

The Kaps will actively locate, bind, and shuttle macromolecules across the FG-Nups meshwork and through the NPC. In contrast to smaller molecules that are able to passively diffuse through the FG-Nups, the Kaps are larger than the size exclusion limit of the NPC. However, the Kaps are able to actively move through the FG-Nups and carry attached cargo along with them despite the Kaps-cargo complex being larger than the cargo is on its own [7, 8]. Early in vivo studies showed that gold particles up to 26 nm in diameter could be actively transported across the NPC [14], which resulted in the general belief that this diameter reflects the threshold size for macromolecules crossing the NPC. However, more recent studies have shown that macromolecular complexes as large as 39 nm in diameter could be actively transported across the NPC [15].

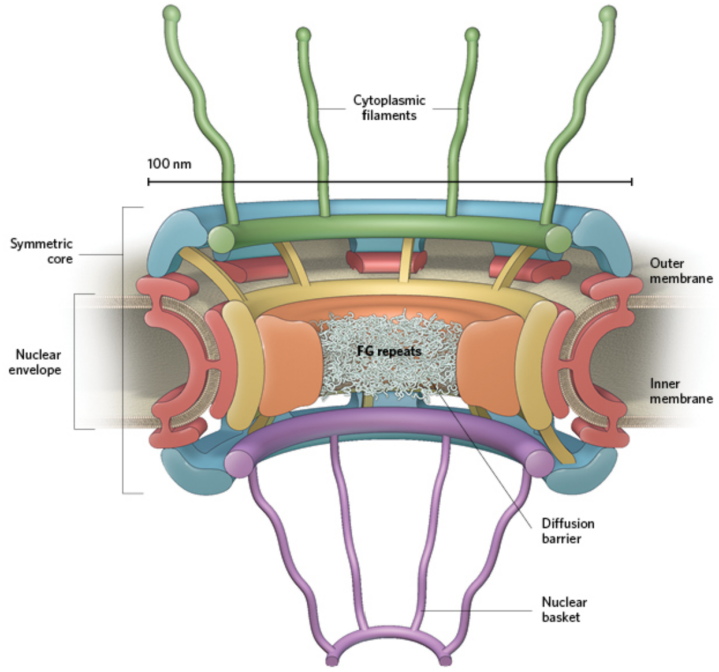

Figure 1.1: Illustration of the major components of the nuclear pore complex such as the cytoplasmic filament, the diffusion barrier at the pore, and the nuclear basket facing the interior of the nucleus. Image taken from Jena (2020) [9].

Although much is known of the shuttle-cargo translocation events from a biological viewpoint [16], the mechanism by which the Kaps shuttle cargo through the diffusion barrier is not well understood and continues to be a challenge. It has been suggested by Denning et al. [17], that it is the intrinsic disorder of the FG-Nups and the scattered distribution of FG-repeats that allow the Kaps to move through the NPC. According to this theory, once the shuttle-cargo complex has entered the NPC it will transverse through the FG-Nups meshwork by sequentially forming and breaking bonds with the FG repeat. This mechanism is also suggested by Rexach et al. [18] and Ribbeck et al. [19].

However, this does not explain how the much larger shuttle-cargo complex is able to enter the NPC while the smaller cargo cannot. This holds true despite the increase in entropic loss the larger volume of the shuttle-cargo complex generates. As an explanation, it has been proposed by Pulupa et al. [20] that nucleoporins inside the diffusion barrier are flexible enough to undergo conformational changes upon engaging with Kaps with and without attached cargo. This would mean that the FG-Nups move around the cargo and, as the shuttle-cargo complex transverses the pore, the FG-Nups network continuously changes it conformation to include the additional volume that the shuttle-cargo complex introduces to the meshwork.

1.1.1.1 The Nuclear Transport Cycle

The biomechanisms behind the shuttle-cargo translocation across the nuclear envelope are commonly known as the nuclear transport cycles. As mentioned earlier, the translocation of individual shuttle-cargo complexes through the diffusion barrier occurs by thermal diffusion that is modulated by the interactions with the FG-Nups. However, when the Kaps shuttle macromolecular cargo through the nuclear envelope it will always be against a concentration gradient of cargo. In terms of thermodynamics, this requires an energy input to the transport cycle. This energy is provided by the hydrolysis, and subsequent conversion, of guanosine triphosphate (GTP) to guanosine diphosphate (GDP) [8]. This hydrolysis leads to an induced conformational change in any attached proteins, such as the transition from Ras-GTP to Ras-GDP, a common molecular switch in signalling pathways [21]. Similar induced conformational change is what drives the shuttle-cargo conjugation and the subsequent cargo release on the other side of the nuclear envelope [8, 16].

While the nuclear transport cycles are complicated processes, they can be simplified into three distinct steps. First, a shuttle locates and binds to a cargo to form a conjugated shuttle-cargo complex. Second, the shuttle interacts with the FG-repeats inside the NPC, and this allows the shuttle-cargo complex to transverse the nuclear pore. Third, an enzyme interacts with the shuttle-cargo complex and triggers a release of the cargo [9]. This simplified mechanism encompasses both the importin and exportin cycles, and as such only the importin cycle will be discussed in more detail. Figure 1.2 shows a schematic illustration of the importin cycle. A more detailed schematic of the cycle is shown in Figure B.1 in Appendix B.

The regulator of the importin cycle is a small GTPase enzyme called Ras-related nuclear protein (Ran). GTPases are a large family of hydrolase enzymes that bind to the nucleotide GTP and hydrolyse it to GDP. When Ran is connected to either GTP or GDP, the conversion between GTP and GDP will change its conformation. This is what triggers the catch-and-release mechanism of the importin cycle. The GTP-bound Ran (RanGTP) is considered active, since it is what releases the cargo, while the GDP-bound Ran (RanGDP) is considered inactive. The catalytic nature of the nuclear transport means that a sub-mechanism exists to convert all GDP back to GTP inside the nuclear envelope to complete the cycle [16, 22].

As seen in Figure B.1 in Appendix B, in cytoplasm the shuttle exists as a heterodimer of two distinct groups of Kaps called importin α (Im_α) and importin β (Im_β). This complex, hereafter referred to as $\text{Im}_{\alpha\beta}$, is usually dissociated by the addition of RanGTP but is stable in the cytoplasm due to the low concentration of this activator. $\text{Im}_{\alpha\beta}$ is able to locate and bind to cargo proteins via a certain set of amino acids called the nuclear localisation sequence (NLS). The NLS is coded for a certain Im_α and is what gives the NPC its high selectivity for translocation. That is, Im_α acts as an adaptor whose purpose is to connect an NLS-protein cargo to an Im_β that mediates the interactions with the nucleoporins [16].

After an NLS-protein cargo has connected with an $\text{Im}_{\alpha\beta}$, the trimeric complex enters

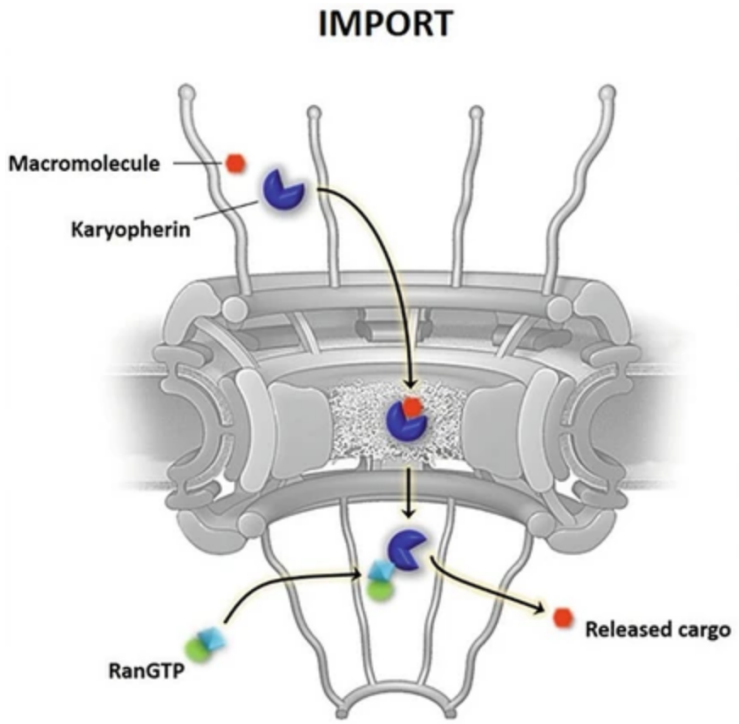

Figure 1.2: Illustration of the major steps of the importin cycle of the unidirectional transport mechanism such as shuttle-cargo conjugation, the shuttling through the diffusion barrier, and the cargo release. Image taken from Jena (2020) [9].

through the nucleoporins at the cytoplasmic fibres of the NPC and is translocated through the NPC. Inside the nucleus, the concentration of RanGTP is high when compared to in the cytoplasm. All Im_β have the ability to interact with Ran when bound to GTP, and when RanGTP binds to the Im_β it will trigger a conformational change. This will dissociate the trimeric complex and release the NLS-protein cargo inside the nucleus [16]. This completes the cargo shuttle mechanism.

Both Im_α and Im_β are shuttled back across the nuclear envelope as complexes with RanGTP, and this process also constantly depletes RanGTP from the nucleus. Recycling of Im_β is done directly while attached to the RanGTP that dissociated the trimeric complex, while recycling of Im_α is mediated by a nuclear export receptor known as a cellular apoptosis susceptibility protein (CAS) [23]. The CAS protein is a secondary Im_β with RanGTP attached to it. Once outside the nucleus, the RanGTP is hydrolysed to RanGDP. This changes the conformation of the Ran, and this triggers a release of both Im_β and Im_α from the export complexes [16].

Depleted Ran is actively re-imported into the nucleus via a transport factor NTF-2, which locates and binds selectively to RanGDP. Inside the nucleus, RanGDP will release from the transport factor, and this regenerates the RanGTP. This maintains the concentration gradient of RanGTP gradient across the NPC, which controls the formation and transport of trimeric cargo complexes. Assembly of this complex occurs in the cytoplasm where the concentration is low, and dissociation occurs in

the nucleus where the concentration is high. This is what controls the directionality of the cycle, as the complex is immediately dissociated inside the nucleus [16].

1.2 Constructing An Artificial NPC

The selectivity and efficiency of the NPC and the associated nuclear transport cycle has been perfected by evolution and natural selection over the span of billions of years. The complexity of the NPC has long driven scientists to try to recreate the selectivity of the shuttle-cargo mechanism. However, fabrication of a fully artificial nanostructures that mimic the transport selectivity is still far away. This thesis aims to take the research one step closer to that goal.

1.2.1 Review of Previous Literature

After reviewing previous literature regarding the construction of a pure artificial system that mimics the NPC and the nuclear transport system, only two examples where an artificial system was shown to selectively translocate cargo-shuttle complexes at a higher rate than cargo was found. In works by Caspi et al. [24], Jovanovic-Talisman et al. [25], and Kowalczyk et al. [26], each group managed to construct artificial shuttle-cargo transport systems for macromolecules. However, in the studies the systems had poor selectivity in terms of leakage and non-conjugated cargo biomolecules were able to slip through the nanopores without a shuttle.

One approach that has been previously employed when mimicking the selectivity of the NPC with a nanoporous structure, is the direct grafting of biological FG-Nups onto the inner walls of solid state nanopores. Using combinations of biological and artificial components have been proven to work in previous work, and was found to be selective against proteins with and without a transport carrier [25, 26]. In the work by Jovanovic-Talisman et al. [25], a device containing two chambers separated by a polycarbonate membrane containing 30 nm diameter nanopores coated with a 15 nm gold film on one side, was functionalised with one of two FG-Nups. Using optical detection, the diffusive flux of fluorescent-labelled protein was compared to that of an open pore. They found that transport proteins translocated at a much higher rate that the control proteins, and that proteins connected to their corresponding Kaps shuttle proteins experienced an enhanced translocation rate compared to the protein alone. This despite the much larger Stokes radii of the shuttle-cargo complex compared to only the cargo. This demonstrated that it was possible to replicate the shuttle-cargo mechanism through a solid state nanopore.

In the work by Kowalczyk et al. [26], the nuclear transport factor Im_β was shown to be selectively translocated through a single 44 ± 2 nm solid state nanopore in a 20 nm silicon nitride membrane, functionalised with two distinct kinds of FG-Nups. They showed that the translocation of the nuclear transport factor was not hindered by the grafting of the FG-Nups, whereas the control protein was significantly decreased once the FG-Nups had been grafted onto the nanopore. This could not be described by a simple difference in size, as the control protein had a lower molecular weight

of 66 kDa that that of Im_{β} at 97 kDa. Neither could it be attributed to differences in electrostatic forces, as the nuclear transport factor and the control protein had similar isoelectric points. Again, this demonstrates that the nuclear transport factor undergoes a selective transport through the nanopore because its interactions with the FG-Nups.

Finally, the work by Caspi et al. [24] is unique of the three in that it attempted, and succeeded, in creating a truly artificial and fully functioning mimic of the NPC transport. They showed that nanopores modified with poly(N-isopropylacrylamide) (PNIPAM) were able to selectively transport fluorescent labelled single stranded DNA. Using PNIPAM both to mimic the FG-repeat domains and the shuttle molecule, they took advantage of the hydrogen bonding interactions between the identical subunits in the two homopolymers to ensure specificity to the transport receptor. By measuring the change in the concentration of fluorescent species over the membrane, they noted that the single stranded DNA was transported at least twice as fast through the functionalised nanopores when conjugated to PNIPAM, then the control without a shuttle. However, and as was stated by the authors, the selectivity of the system was low, and serves to illustrate the possibility of a system that mimic the NPC transport. Furthermore, they suggested that the underlying mechanism of the selective transport was hindrance of the single stranded DNA, more than a preferential transport of the PNIPAM shuttle.

1.3 Motivation

This thesis will investigate the viability of using poly(methacrylic acid) and poly(N-(2-hydroxyethyl)acrylamide) as a shuttle and diffusion barrier for replicating the nuclear transport cycle of the nuclear pore complex. The interaction characteristics of the two polymers will be evaluated, and the ability of the artificial shuttle to transport fluorescent cargo through the artificial diffusion barrier will be investigated. The aim is that the results derived from this thesis will contribute to an increased understanding of the underlying soft matter chemistry and physics of the shuttle-cargo translocation, and to further investigate the potential of using the shuttle and diffusion barrier pair in a device for single molecule trapping. Figure 1.3 shows an illustration of a device, where a shuttle modified with a receptor would be able to capture a specific target protein from a complex mixture, transport them to the other side of a membrane with a nanopore covered with a selective diffusion barrier, and then release it inside a nanochamber on the other side.

An area in which a functioning artificial shuttle-cargo mechanism could be applied is in the use of confocal fluorescence microscopy for the study of protein structures and folding kinetics. While the use of a small confocal volume allows the characterisation of proteins on a single molecule level, the diffusion mobility of proteins via Brownian motion means that they will only remain within that volume for a few milliseconds. A device that could capture and trap a single protein within a nanoscale chamber would limit it to remain within that volume and thus extend the time it could be studied indefinitely, or until the fluorescent group on the protein is photobleached.

This would offer both additional and more detailed information on the protein [27], which would have great benefits for instance in medical research.

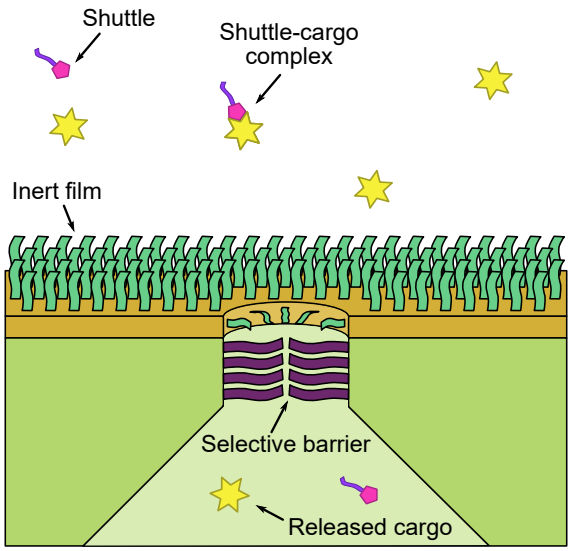

Figure 1.3: Illustration of a device that would use a functioning artificial shuttle-cargo mechanism to capture and isolate specific target proteins in a nanochamber.

1.4 Limitations

This thesis will limit the study of the proposed artificial shuttle-cargo mechanism to a system where poly(methacrylic acid) acts as a synthetic shuttle and poly(N-(2-hydroxyethyl)acrylamide) acts as a synthetic diffusion barrier. This thesis aim is to understand if this specific pair of polymers will work as a shuttle-barrier pair for use in transporting macromolecular cargo through solid state nanopores.

A limitation made was that the RanGTP controlled release mechanism was omitted. With this in mind, the receptor on the synthetic shuttle was covalently attached, as the separation of Im_{α} and Im_{β} in the heterodimer shuttle complex only plays a role in the release mechanism where RanGTP interacts with $\mathrm{Im}_{\alpha\beta}$ [16].

1.5 Mimicking the Nuclear Transport Cycle

With the limitations previously mentioned, we simplified the structure of the NPC and the associated shuttle-cargo mechanism into three fundamental components. Substituting each of these three components with an artificial construct would allow us to recreate the shuttle-cargo mechanism of the NPC. The nuclear envelope was substituted with a 50 nm thick silicon nitride (Si_3N_4) membrane. A 30 nm thick gold coating was deposited on this substrate and arrays of solid state nanopores were fabricated to substitute the supporting scaffolds of the NPC. These nanopores were made to be 80 nm in diameter, which is similar to the average size of outer channel of the NPC [8].

Substitutes for both the diffusion barrier and the selective shuttle were chosen to be polymers, as this would allow us to fine-tune the interaction between the synthetic shuttle and the synthetic diffusion barrier. The FG-Nups diffusion barrier was substituted by poly(N-(2-hydroxyethyl)acrylamide) (PHEAA) that was attached on the gold coating on the Si_3N_4 membrane. The selective shuttle protein was substituted by poly(methacrylic acid) (PMAA) with and without an end-group termination of a reactive amine that served as an anchoring point for molecular cargo.

1.5.0.1 Synthetic FG-Nups Diffusion Barrier

An important criterion when mimicking the functionality of the FG-Nups diffusion barrier is that the substitute exhibits non-interactive characteristics towards proteins and other large macromolecules, while still being able to incorporate a shuttle with attached cargo. A way to create a barrier on a membrane is to graft polymers on it. When polymers are grafted from a surface at a high surface coverage it promotes stretching of the chains perpendicular to the surface, forming a "brush" structure with a thickness that is significantly larger than the diameter of an isolated coil [28]. In water, hydrophilic brushes have been reported to serve as entropic barriers against proteins and other macromolecules by Emilsson et al. [29] and would thus make for a good barrier.

An ongoing discussion in the study of highly hydrated polymer brushes is the origin of their antifouling properties. The water barrier theory [30, 31], states that the antifouling properties arise from a strong association between the extended polymers and a hydration layer that forms a physical and energetic barrier to prevent protein adsorption on the surface. When a macromolecule enters the brush, water molecules associated to the brush will be released. This increases the entropy of the water molecules. However, it will also increase the enthalpy of the chains from the loss of favourable interactions with the coupled water as well as decrease the entropy of the chains as they need to move to accomodate the volume of the protein. An increase in enthalpy and a decrease in entropy is thermodynamically unfavourable. This is known as the steric repulsion theory, first proposed by De Gennes et al. [32]. So, as long as the free energy of the brush-water system is increased when the macromolecule approaches the brush structure, the insertion of the macromolecule into the brush will be unfavourable and the macromolecule is expelled from the brush [33, 34].

This is important when considering using a highly hydrated brush as a substitute for the FG-Nups diffusion barrier. The natively intrinsic disorder of a highly hydrated brush structure gives the barrier a high degree of flexibility, which is beneficial as it more easily incorporates the additional volume of the shuttle and its macromolecular cargo following its insertion into the brush. However, a higher degree of hydration could also increase its expelling properties against the macromolecular cargo, which would make it harder to incorporate the additional volume. Therefore, it is necessary that the shuttle replaces as many of the hydrogen bond opportunities as possible once inside the brush, to compensate for the increase in free energy from the insertion.

As a final criterion, it is important that the morphology and antifouling properties of the brush structure do not change when the shuttle is inserted. Even while the shuttles are actively carrying cargo through the selective barrier it should prevent all non-attached cargo from moving through the membrane. For this reason, PHEAA was chosen as a substitute, as it had been shown in early testing to interact with PMAA without changing its structural morphology. It had also been shown to have a high antifouling ability by Zhao et al. [35], and a high degree of hydration.

1.5.0.2 Synthetic Kaps Shuttle

An important criterion for mimicking the Kaps shuttle is that the substitute can exists in a state where it has good affinity for the barrier substitute and that it can form multiple bonds at different anchoring sites. Similar to how the Kaps move through the FG-Nups, it would then be able to diffuse through the barrier substitute via sequential association and dissociation. Figure 1.4 shows an illustration of the stochastic walk with which the shuttle substitute would be able to move itself, and any attached cargo, through a polymer brush barrier by sequential binding.

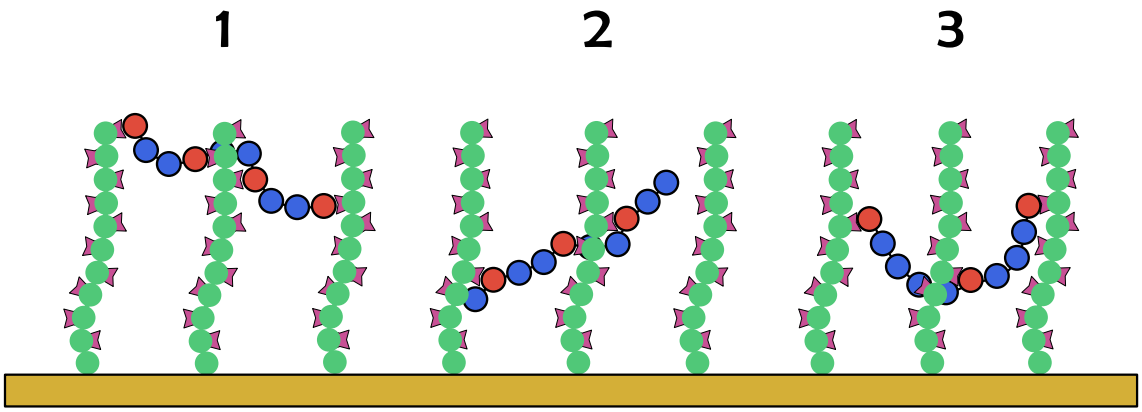

Figure 1.4: Illustration of the stochastic walk of PMAA through a PHEAA brush. Green dots represent PHEAA monomer units, blue dots represent inactive PMAA monomer units, and red dots represent active PMAA-PHEAA hydrogen bonds.

For a Kaps shuttle substitute to undergo this stochastic walk, it is necessary that it is able to form multiple simultaneous hydrogen bonds with the brush. Since PHEAA is a polymer, each monomer unit in the brush backbone would be able to form a hydrogen bond and function as an anchoring point for the shuttle. Similarly, each monomer unit in PMAA would be able to form a hydrogen bond and this would allow it to undergo a sequential diffusion through a PHEAA brush. Further, if the affinity between the shuttle and the brush could be tuned by an external trigger the same shuttle could be used as a reference to see if the transport is due to interactions between the shuttle and the brush or by the shuttle being pressed through the pore.

Being a polyelectrolyte, PMAA can exist in both a neutral protonated state where it is able to form hydrogen bonds with PHEAA, and a charged state where it is not able to interact with PHEAA. Which of these states PMAA is in depends on the solvent pH. At low pH, the acids on PMAA are protonated and PMAA is able to

form hydrogen bonds with PHEAA. This is a simple trigger to switch it from a high affinity state to a low affinity state. In the device mentioned in Figure 1.3, toggling on the affinity between PMAA and PHEAA would allow the shuttle-cargo complex to diffuse through the selective barrier and into the nanochamber. Once inside the nanochamber, the affinity is toggled off and the shuttle-cargo complex is trapped.

Controlling the degree of protonation via the solvent pH would also allow for fine-tuning of the rate of diffusion of the shuttle through the brush. With a higher degree of protonation, PMAA will form more hydrogen bonds with PHEAA, and this will increase the strength with which it binds. This will affect the rate at which it forms and breaks bonds with the brush, and thus the rate of diffusion through the brush.

The capability of PMAA to undergo hydrogen bonding complexation with other polymers have been shown in numerous studies, for instance, in the work by Fortier-McGill et al. [36] and Andersson et al. [37]. Importantly, Fortier-McGill et al. characterised the interactions between PMAA and poly(acrylamide) (PAAM) using NMR, and showed that the properties of the complex was due to weak hydrogen bond formations, and that the interaction between PMAA and PAAM also weakened the intrapolymer hydrogen bonding of PMAA [36]. This is important for this thesis project, as the PMAA shuttle must be able to undergo hydrogen bonding complexation with the PHEAA barrier, and preferentially bind with the shuttle more than with itself. While this was shown for a similar, but still different, polymer than what will be used as a barrier in this thesis project, it shows that it is possible for PMAA to form weak hydrogen bond complexes.

1.5.0.3 $\mathbf{Im}_{\alpha}$ Adaptor Substitute

As was mentioned for the biological system, NLS-protein cargo is attached to the shuttle proteins via Im_{α} that locates and binds to the NLS. In the synthetic shuttle this is substituted by addition of a reactive group on the α-terminal end group of the chain. Varying this reactive group, the shuttle can covalently attach to a specific cargo, while leaving non-compatible cargo without a shuttle. Due to the antifouling properties of the PHEAA brush, only the cargoes with an attached shuttle can enter the brush, while the non-specific cargoes are expelled by the brush.

2

Theoretical Background

2.1 Atom Transfer Radical Polymerisation

End-functionalized polymer chains may be grafted to the solid substrate (grafting-to), or the grafting can proceed by polymerisation from the surface (grafting-from). Using a grafting-from approach produces dense polymer brushes, while using a grafting-to approach produces thinner polymer brushes but with higher control of the polydispersity [38]. Methods for grafting brushes to a surface have been shown by Emilsson et al. to give a grafting density that was sufficiently high to make the brushes function as entropic barriers [29]. However, in this thesis brushes were grafted-from a gold surface with a variant of atom transfer radical polymerisation (ATRP) to achieve higher molecular weight.

Surface-initiated controlled radical polymerisation is an efficient method to synthesise brushes of desired functionality and molecular weight on various nanomaterials [39, 40, 41, 42]. Controlled radical polymerisation (CRP) is a method that uses a dynamic equilibrium between growing radicals and dormant species in a reaction to slow down the propagation steps and diminish the rate of termination of active radical species [40, 43]. In CRP, active radicals usually undergo a single addition of a monomer before converting back to a dormant state. It can thereafter be reactivated from the dormant state to continue polymerisation. This allows for a high degree of control over the polymer's molecular weight, molecular weight distribution, and composition [40].

Figure 2.1 shows a schematic of a general ATRP equilibrium. In ATRP, the dormant species are either initiating alkyl halides that has been grafted-to the surface prior to polymerisation or a polymer with a halide end-group. The mechanism of ATRP relies on the establishment of an equilibrium between the dormant species ($P_n{-}X$) and active species ($P_n^{\bullet}$). The active species are generated by cleaving the halide bond with a reversible redox process catalysed by a redox-active activator. The activators (Mt^n/L) are ligand-stabilised low-oxidation state transition metal complexes. After the active species have added a few monomer units they react with a deactivator, which reforms the dormant species. The deactivators ($X{-}Mt^{n+1}/L$) are ligand-stabilised high-oxidation state transition metal complexes, and once it deactivates

an active species the activator metal complex is regenerated [39, 40, 43].

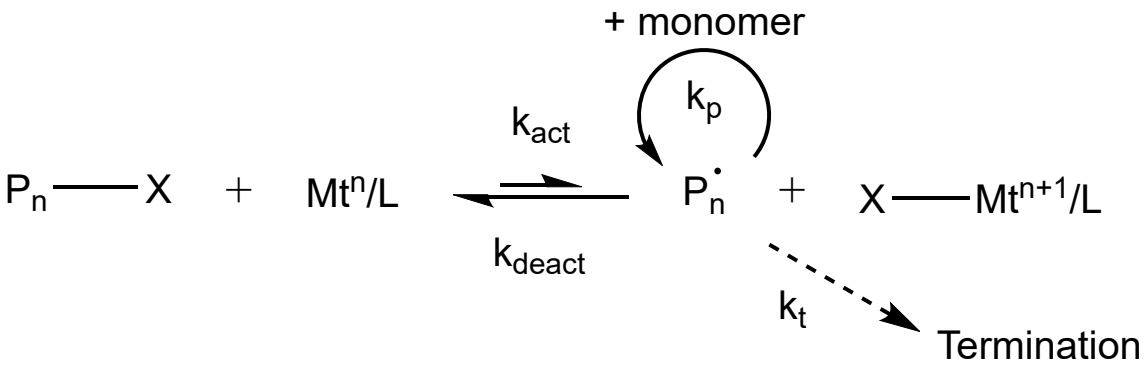

Figure 2.1: Schematic of a general ATRP equilibrium.

This process occurs with a rate constant of activation (k_{act}) and deactivation (k_{deact}) that are controlled by the rate of the redox-reactions between the dormant/active species and the ligand-stabilised transition metal complexes. Activation should be kept slower than deactivation to ensure that the number of active species are low. This reduces the rate of termination (k_{t}), as the number of active species is lowered and thus the probability of two active species reacting to terminate the process is lowered. While termination does occur in ATRP, as long as the reaction is well controlled no more than a few percent of all polymer chains should undergo premature termination [39, 40, 43].

On surfaces, termination is widely believed to be the result of a high grafting density of polymers in a brush, and that when two active chains are formed too close to one another might move through the brush, eventually finding and connecting and thus preventing further reactivation. However, due to a lack of surface information, a detailed study about the surface termination mechanism has never been carried out [44]. Using a simulation, Gao et al. [44] found that a lack of mobility of chains grafted to a surface made the common theory of termination unlikely. Instead, they suggested that termination was linked to the movement of radicals across the surface. That is, as the active chains are deactivated and new radicals are formed, it can be considered a migration of radicals from one chain to another. According to their theory, termination only occurs when two radicals migrate to adjacent chains, allowing the two adjacent chains to connect and thus prevent further reactivation. Furthermore, this explained the connection between the activation/deactivation rate and the termination rate, as a faster activation and deactivation cycle would lead to a more frequent migration of radicals on the surface, increasing the probability of two radicals being adjacent to one another on the surface [44].

Active species grow by addition of the intermediate radicals to monomers akin to conventional radical polymerisation. This is controlled by the rate constant of propagation (k_{p}), as well as the concentration of monomer and active species. The magnitude of the equilibrium constant, defined as the ratio $k_{\mathrm{act}}/k_{\mathrm{deact}}$, determines the rate of polymerisation R_{p}. ATRP will not occur if the equilibrium constant it too low. Instead, if the equilibrium constant is too high the amount of active species will

be too high and this will lead to termination [40, 43]. While each monomer has its own intrinsic rate of polymerisation, the catalytic nature of ATRP allows the equilibrium to be shifted by adjusting the amount and reactivity of the ligand-stabilised transition metal complex. The equilibrium constant increases with the strength of the X−Mt^{n+1} bonds and the halogenophilicity of the Mt^{n} complex [40, 45]. The latter is the activators' ability to attack the dormant species' halide [46].

The reaction can be stopped at any time by removing the activator from the reaction solution. When all activators are removed, any remaining active species will quickly be quenched, and the reaction stops.

2.1.1 ARGET ATRP

A limitation of ATRP is the large amount of catalyst required for the polymerisation to propagate over a long duration. Due to termination of the active species, which does not regenerate the activator, the concentration of activators will eventually decrease, and the reaction will stop. Using a large amount of metal catalyst also leaves residual metal that creates difficulties in purification of the final product [47]. However, the rate of polymerisation in ATRP does not depend on the total activator concentration, but the ratio of concentrations of activators and deactivators. This is shown in Equation 2.1, the rate of polymerisation in ATRP [40]. An increase in the ratio of activators and deactivators will increase the rate of polymerisation.

$$R_{\mathrm{p}} = k_{\mathrm{p}} \left(\frac{k_{\mathrm{act}}}{k_{\mathrm{deact}}} \right) \left(\frac{[\mathrm{Mt}^{n}/\mathrm{L}]}{[\mathrm{X} - \mathrm{Mt}^{n+1}/\mathrm{L}]} \right) [\mathrm{P}_{n}\mathrm{X}][\mathrm{Monomer}] \tag{2.1}$$

If the activators could be regenerated during the reaction despite the presence of radical termination, a lower total concentration of catalyst could be used, and the rate of polymerisation could be controlled by the concentration ratio of activator and deactivator. One such procedure is activators regenerated by electron transfer (ARGET) ATRP. When applying ARGET to ATRP the redox-active activator is constantly regenerated by reducing agents which compensate for any loss of activator as a result of termination [48]. Figure 2.2 shows a schematic of a general ARGET ATRP equilibrium. This is similar in mechanism to the general ATRP equilibrium shown in Figure 2.1, but with an additional regeneration step following termination.

Surface-initiated (SI)-ARGET ATRP have been shown to work for functionalisation of surfaces with polymer brushes [42, 49, 50]. Controlled polymerisation with SI-ARGET ATRP has been observed even with catalyst concentrations as low as 50 ppm relative to the amount of monomer [50]. Furthermore, when employing a copper catalyst, the process can be started with the oxidatively stable Cu(II) species instead of the oxygen-sensitive Cu(I) species used in conventional ATRP. The Cu(II) species is reduced by the addition of a reducing agent [48]. A proven effective reducing agent is ascorbic acid [51, 52, 53]. In this thesis the reaction conditions were based on previous results by Matyjaszewski et al. [52]. As each monomer has its own intrinsic

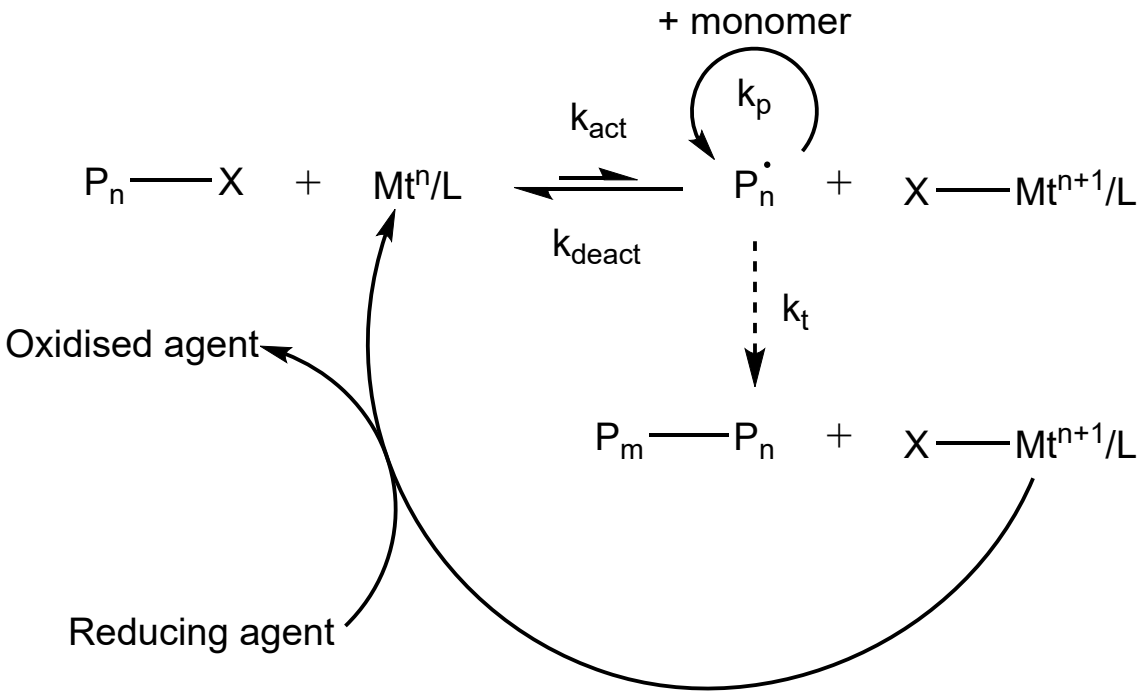

Figure 2.2: Schematic of a general ARGET ATRP equilibrium.

rate of polymerisation, the reaction conditions were optimised for PHEAA.

An additional benefit of ARGET ATRP is an improved oxygen tolerance compared to conventional ATRP. As the transition metal complex is used in ppm concentrations, the large excess of reducing agent will not only reduce the catalyst but will also eliminate oxygen and radical inhibitors in the solution. In ATRP, it is necessary to deoxygenate the solution. However, in ARGET ATRP this is not strictly necessary as long as a sufficient excess of reducing agent is used [48, 54, 55, 56]. However, the concentration of the reducing agent and related rate of reduction can influence the ARGET ATRP. In this thesis the reaction solution was deoxygenated prior to polymerisation to achieve a more consistent oxygen level in solution.

2.2 Surface Plasmon Resonance

Surface plasmon resonance (SPR) spectroscopy is a surface sensitive analysis technique that can be used to analyse binding affinities and kinetic parameters between a ligand and an analyte. It is label-free and allows monitoring of both covalent [57] and non-covalent molecular interactions in real time and in a non-invasive fashion. SPR measurements reflect the change in reflective index near the surface of the sensor as analytes bind to a given ligand. Measuring the change in reflective index over time generates a sensorgram that can be used to indicate if the analyte binds to the ligand or not, and what the kinetics of the interaction is [58, 59, 60, 61].

Surface plasmon resonance occurs when a photon of incident light hits a metal medium and interacts with electrons in the medium. At a certain angle of inci-

dence, the incident light undergoes total internal reflection (TIR) and generates an evanescent field that penetrates the metal film. Energy in the evanescent field will couple with the medium and induce oscillations in the free charge carriers of the metal film. This is reflected as a decrease in the intensity of the reflected light [60].

The resonance angle at which the decrease in reflected light intensity occurs is sensitive to changes in the refractive index within the evanescent field. Therefore, whenever there is a significant change in concentration of an analyte near the surface of the sensor it will change the resonance angle and disrupt the plasmon. In order to regenerate the plasmon the angle of the incident light must be changed and this change is measured and analysed when conducting experiments with SPR [60, 61].

2.2.1 Sensorgram Stages

When the change in SPR angle $\Delta\Theta_{\text{SPR}}$ (deg) and TIR angle $\Delta\Theta_{\text{TIR}}$ (deg) as a response to injection of an analyte is plotted over time, the resulting plot is called a sensorgram. It is commonly composed of the five stages shown in Figure 2.3. $\Delta\Theta_{\text{SPR}}$ is proportional to the concentration of analyte present within the evanescent field of the surface, while $\Delta\Theta_{\text{TIR}}$ is proportional to the concentration of analyte present throughout the entire bulk of the flow cell. As will be discussed in more detailed later, these two angle shifts give information on how much analyte has been attached to a surface, how fast it attached, and how fast it detached again [62].

At stage 1 an initial baseline is always established by rinsing the surface with a buffer. $\Delta\Theta_{\text{SPR}}$ is compared to this baseline when determining if an analyte interacts with the surface. At stage 2 the analyte is injected and associates with the surface. The rate at which the analyte associates R_{on} (s^{-1}) depends on the association constant κ_{on} ($\text{M}^{-1}\text{s}^{-1}$) and the concentration of analyte C_0 (M). A higher analyte concentration will give a faster association [62].

At stage 3 the analyte has reached an equilibrium distribution between the brush and the bulk. This distribution depends on the rate of association, and its dependence on the analyte concentration, as well as the rate of dissociation. A higher analyte concentration increases the equilibrium shift, until it reaches the point where the surface is saturated. How much of the surface is saturated at a given concentration is usually described by the affinity constant (KD [M]), which is defined as the ratio of the dissociation and association constants. It also describes the concentration at which 50% of the surface is saturated [62].

At stage 4 the injection is stopped, indicated by a fast decrease in $\Delta\Theta_{\text{TIR}}$, and the analyte is allowed to release from the surface. The dissociation rate R_{off} (s^{-1}) does not depend on the concentration of analyte that was injected in stage 2. It only depends on the dissociation constant κ_{off} (s^{-1}). Some analyte is usually left irreversible bound to the surface, indicated by a remaining $\Delta\Theta_{\text{SPR}}$ relative to the baseline after stage 4. This is removed in stage 5, where a regeneration solution is

injected to restore $\Delta\Theta_{SPR}$ to the baseline. In this thesis this was done by injecting a buffer at a high pH.

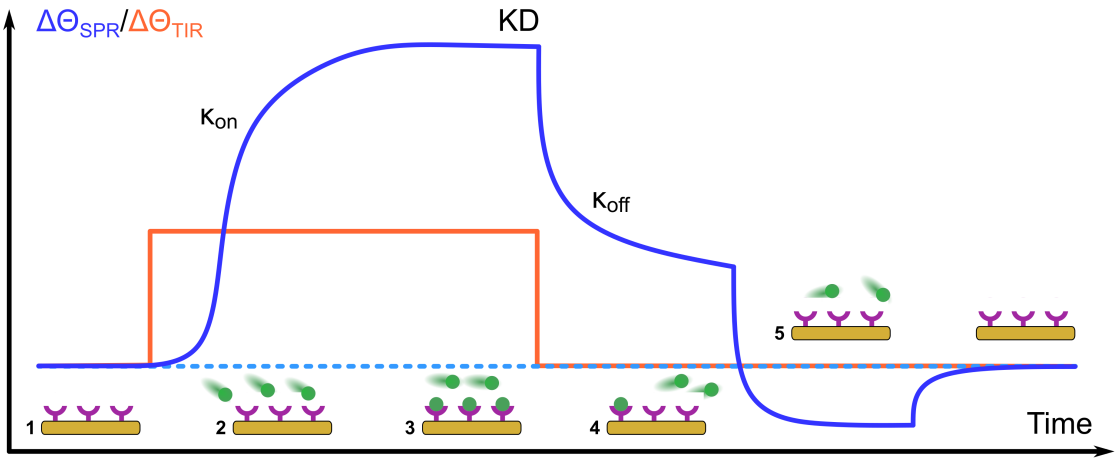

Figure 2.3: An illustration of the five stages of a conventional sensorgram. $\Delta\Theta_{SPR}$ is shown in blue, $\Delta\Theta_{TIR}$ is shown in red, and the SPR baseline in dashed light blue.

2.2.2 The Non-Interactive Probe Method

Determining the conformational structure of hydrated films was long an unresolved problem in SPR spectroscopy. However, by injecting a non-interactive probe that could sense the intrinsic exclusion volume of a molecular layer on the surface but not interact with it, the exclusion height of the surface could be determined. As the non-interactive probe does not interact with the surface layer it is non-invasive and allows for easy estimations of the films thickness. The exclusion height is the characteristic distance away from the surface at which the non-interactive probe is prevented from getting closer to the surface. If the surface has a thick polymer coating and the probe is completely unable to enter the brush, then that exclusion height would be the outermost height of the brushes [63].

In previous work, this method has been shown to work for determination of exclusion height of polymer brushes using the bulk signal from non-interactive macromolecular probes and fittings of Fresnel models [42, 49, 57, 37, 64]. The original method proposed by Schoch et al. compares the shift in resonance angle when non-interactive probe in high concentration (at least 10 mg/ml) is injected compared to a surface without the polymer brush. How much the resonance angle shifts depends on how deep into the evanescent field the non-interactive probe can penetrate. A thick brush will exclude a volume far away from the surface where the strength of the evanescent field is weak and the change in resonance angle is small. When the thickness of the brush exceeds the decay length of the evanescent field, usually defined as the distance over which the field decays to $1/e$ of its maximum intensity, the probe will no longer be easily detected [63]. When a non-interactive probe enters the evanescent field near a surface the effective refractive index n_{eff} will increase as shown in Equation 2.2 [63]. n_{p} is the refractive index of the non-interactive probe, n_{s} is the refractive

index of the solvent, d is the distance away from the surface and δ is the decay length of the evanescent field.

$$\Delta n_{\text{eff}} = (n_{\text{p}} - n_{\text{s}}) \exp(-2d/\delta) \tag{2.2}$$

In the absence of adsorption of the probe from solution the resonance response is from changes of the refractive index in the bulk solution. Therefore, the effective change in the refractive index can be correlated to the resonance response R and the slope relating to the change in resonance response due to changes in the bulk liquid. The latter is related to the TIR angle. An integrated solution for the distance away from the surface in relation to the decay length of the evanescent field is shown in Equation 2.3 [63]. Here d_0 is the distance away from a reference surface with a known height that the non-interactive probes are repelled, R_i is the SPR response resulting from the non-interacting molecules, and m_i is the slope relating the change in the SPR response to changes in Δn_{eff} in the bulk.

$$\frac{d}{\delta} - \frac{d_0}{\delta} = \frac{1}{2} \ln\left(\frac{R_1 m_2}{R_2 m_1}\right) \tag{2.3}$$

When determining the exclusion height of a surface the decay length of the evanescent field needs to be approximated. Equation 2.4 shows a rough approximation of the real part of the decay length where the finite thickness of the metal layer has been neglected [63]. Here ε'_m is the real part of the dielectric permittivity of the metal, ε_d is the dielectric permittivity of the nonabsorbing medium, i.e., water, and λ is the wavelength of the incident light. A more accurate estimate is achieved by solving Maxwell's equations, as has been shown by Johnston et al. [65, 66].

$$\delta \approx \frac{\lambda}{2\pi} \sqrt{\left(\frac{\varepsilon_d + \varepsilon'_m}{-\varepsilon_d^2}\right)} \tag{2.4}$$

2.2.2.1 Modified Non-Interactive Probe Method

In the modified method first used by Emilsson et al. [57], the inclusion of Fresnel modelling into the non-interactive probe method removes the need to approximate the decay length of the evanescent field. It also makes it possible to determine the exclusion height of less hydrated brushes, as a limitation of the original method is that the refractive index of the hydrated brush must be close to that of the solvent. Instead, the reflectivity spectra of each layer on the SPR sensor are fitted to standard Fresnel models using the additional information found in the TIR angle. This new method has been demonstrated to be effective in several works by Andersson et al. [37], Ferrand-Drake del Castille et al. [49, 64], and Svirelis et al. [67].

As a first step, a background model is obtained by fitting angular spectra, measured

at the incident light of interest, of planar gold surfaces in PBS. Then the bulk change in refractive index when injecting a solution of non-interactive macromolecules over the hydrated film is determined via the shift in the TIR angle using Fresnel models. Following this, the angular spectrum of the hydrated film in PBS is fitted by the addition of a new layers representing the initiation layer and the polymer.

By assuming several thickness values and varying the refractive index of the adhesion layer to fit the spectrum in each case, i pairs of thicknesses d and refractive indexes n (d_i, n_i) are generated. The same iterative fitting is then performed for the angular spectrum during the non-interactive probe injection, after compensating for the change in the bulk refractive index determined using the TIR angle, yielding another set of i pairs. The pair of d and n which best represents the adhesion layers is found at the intersection when plotting the two sets, yielding a unique solution that tells the thickness and effective refractive index of the brush [57].

2.2.2.2 Bulk Response Compensation

An inconvenient side effect of the evanescent field extending beyond the surface layer is that the SPR will not only detect analytes that interacts with the surface, but also analytes beyond the surface. While this is desirable for determination of the exclusion height of the surface coating using a non-interactive probe, it is not desirable when only the interaction between an analyte and the surface is of interest. Using a physical model presented by Svirelis et al. [67], it was possible to remove response coming from outside the polymer brush coating and this allowed them to reveal the true kinetics of the interaction between the analyte and the surface.

The TIR angle in a sensorgram will only increase when the bulk refractive index is changed [49]. The physical model utilises the change in TIR angle to compensate for the bulk response. This means that it only compensates for the bulk response while there is an enhanced concentration of analytes in the bulk. However, the compensation will act on $\Delta\Theta_{\mathrm{SPR}}$ during the entirety of the injection and this introduces additional noise from $\Delta\Theta_{\mathrm{TIR}}$ into the compensated signal.

Equation 2.5 shows the physical model and the compensated shift $\Delta\Theta^*_{\mathrm{SPR}}$ proposed by Svirelis et al. [67]. Here S_{SPR} and S_{TIR} are the sensitivities of the SPR and TIR angles (degrees per RI unit), $\Delta\Theta_{\mathrm{SPR}}$ and $\Delta\Theta_{\mathrm{TIR}}$ are the measured SPR and TIR angles, δ is the decay length of the evanescent field, and d is the surface exclusion height. The dependence on d tells us that in the limit where $d \to \delta$, it will be harder for the model to differentiate between bulk effects and surface interactions.

$$\Delta\Theta^*_{\mathrm{SPR}} = \Delta\Theta_{\mathrm{SPR}} - \Delta\Theta_{\mathrm{TIR}} \left(\frac{S_{\mathrm{SPR}}}{S_{\mathrm{TIR}}} \right) \exp(-2d/\delta) \tag{2.5}$$

This model can further be simplified when combined with the non-interacting probe method described earlier. Since the probe analyte does not interact with the surface, any resonance response that it generates in the SPR sensorgram must represent the

pure signal from the bulk. Thus, scaling the TIR compensation with a constant ω until the signal from the non-interactive probe cancels out in the SPR response will also correct the SPR response during analyte injections and return only the pure kinetics of the interaction. A modified model is shown in Equation 2.6.

$$\Delta\Theta^{*}_{\mathrm{SPR}} = \Delta\Theta_{\mathrm{SPR}} - \omega\Delta\Theta_{\mathrm{TIR}} \tag{2.6}$$

2.3 Quartz Crystal Microbalance

Quartz crystal microbalance (QCM) is an extremely sensitive technique that measures a mass variation per unit area down to an accuracy of a ng/cm^2. This is done this by measuring the change in oscillator frequency of a quartz resonator. Quartz is a piezoelectric material that can be made to oscillate at a defined frequency by applying a voltage. Whenever mass is added or removed from the quartz resonator, the oscillation frequency f will change in this can be monitored in real time to obtain information about molecular interactions of an analyte and a surface [68].

2.3.1 Energy Dissipation Monitoring

However, the relationship between adsorbed mass and frequency only holds true for dry and rigid systems. In a liquid environment, molecular adsorption measured by the resonator arise not only from analytes, but also includes the mass of the associated liquid molecules that are attached to the analytes. This additional mass usually comes from direct hydration of the analyte and/or from entrapment within the adsorbed film. This results in the adsorbed film not fully coupling to the resonator, which in turn can lead to an energy dissipation, i.e. loss, of the oscillation. Equation 2.7 shows the definition of oscillation energy dissipation. Here $E_{\mathrm{dissipated}}$ is the loss of energy per oscillation and E_{stored} is the amount of energy stored [69].

$$D = \frac{1}{2\pi}\left(\frac{E_{\mathrm{dissipated}}}{E_{\mathrm{stored}}}\right) \tag{2.7}$$

Whenever the adsorbed film on the resonator has associated liquid molecules, it will exhibit some viscoelastic characteristics. The mass of such films cannot be determined by measuring only the oscillation frequency change. Additional information from the dissipation change ΔD is required to accurately determine the mass change of a viscoelastic film. This is the key addition of dissipation monitoring (QCM-D). By monitoring both Δf and ΔD over time, information about the structure of the adsorbed film can be detected, such as conformational changes, crosslinking, and swelling [69]. A polymer brush is, by definition, hydrated in liquid [28], meaning that dissipation monitoring is necessary when investigating those kinds of systems.

In a QCM-D system the dissipation is monitored by exciting an oscillation with a short voltage pulse, and then measuring the oscillation decay over time after the

pulse is turned off. Equation 2.8 shows an expression for the exponentially dampened sinusoidal wave that this results in [70]. Here A is the oscillation amplitude, f_0 is the fundamental frequency of the oscillation, n is the active overtone, and τ is the decay time.

$$A(t) = A_0 \exp\left(\frac{t}{\tau}\right) \sin\left[2\pi n f_0 t\right] \tag{2.8}$$

The decay time depends on the rigidity or softness of the mass adsorbed on the crystal surface. When the adsorbed film is rigid, the oscillation in the film is highly coupled to that of the resonator and will thus take longer to decay. Similarly, when the adsorbed film is viscoelastic, the oscillation in the film is poorly coupled to the resonant and will rapidly decay. Equation 2.9 shows the relationship between the dissipation constant and the decay time. By measuring the change in decay time of the oscillation over every measurement cycle, the change in dissipation is obtained and can be used for information about molecular interactions.

$$D = \frac{1}{\pi n f_0 \tau} \tag{2.9}$$

2.3.1.1 Resonator Overtones

QCM-D measures both the oscillation frequency and dissipation at multiple overtones of oscillation [69]. These overtones must be odd, i.e., the third, the fifth, etc., relative to the fundamental overtone to ensure an antisymmetric pattern of motion of the acoustic wave. If the overtone order is even, the deformation is symmetric and there is no current between the electrodes [68]. Usually, the fundamental overtone is not used when modelling polymer films, and the third or fifth overtones are preferred. Most QCM-D systems allow measurements of up to the 13th overtone. Normally, for thin adlayers, the penetration depth is mostly determined by the solvent. However, as the height of the hydrated brush increases the properties of the polymer will begin to dominate.

As the overtone number increases, the penetration depth decreases, which allows for insight into certain vertical regions of the adhered film [69]. E.g., the penetration depth of the 13th overtone is much shallower than that of the 3rd overtone. This allows us to conclude that if a molecular interaction only occurs in the lower overtones, it is likely that the analyte had not moved deeply into the adsorbed film. Assuming it is thick enough. Equation 2.10 shows the characteristic penetration depth Δ of an acoustic wave in a liquid or soft adsorbed film [69]. Here ρ_m is the density of the adsorbed film, η_m is the viscosity of the adsorbed film, f_0 is the fundamental frequency, and n is the overtone.

$$\Delta_n = \sqrt{\frac{\eta_m}{\pi n f_0 \rho_m}} \tag{2.10}$$

Equation 2.10 can be used to estimate the penetration depth. However, due to the parabolic monomer concentration gradient throughout a polymer brush [71], the viscosity to density ratio of the hydrated film will not remain the same throughout. Where the monomer concentration of polymer is high, the viscosity to density ratio will also be high, as polymers in general have a much higher viscosity as water, while having a similar density. As the water content increases further away from the surface, the viscosity to density ratio will decrease and so will the effective penetration depth relative to that distance away from the surface. Calculating the penetration depth away from surface relative to the properties of pure PBS will yield the lowest possible penetration depths away from the surface, and gives the general progression of the overtones, demonstrating that the higher overtones have a shallower penetration depth than the lower overtones.

3

Experimental Section

The aim of this chapter is to describe the experimental techniques and calculations used within this thesis. Many SPR, QCM and fluorescent measurements were conducted in order to achieve the aim of the project, to investigate the viability of using PMAA and PHEAA as a shuttle and diffusion barrier for replicating the nuclear transport cycle of the nuclear pore complex. Subsequently, the results of the measurements were used to draw conclusions on the interactions between PMAA and PHEAA and the efficiency of the shuttle mechanism.

3.1 Materials and Chemicals

Gold coated SPR sensors were purchased from Bionavis, and QCM-D sensors were purchased from QuartzPro. H_2O_2 (35%) was purchased from SAFC. Sulfo-Cyanine3 NHS ester was purchased from Lumiprobe. α-amino terminated poly(methacrylic acid) was purchased from Polymer Source, Inc. NH_4OH (25%) and NHS-Fluorescein (5/6-carboxyfluorescein succinimidyl ester) was purchased from Fisher Scientific.

Chemicals purchased from Sigma-Aldrich include poly(methacrylic acid) sodium salt 30 wt% solution in H_2O (5.4 kg/mol and PDI of 1.76), avidin from egg white ($\geq$98% purified by sodium dodecyl sulfate–polyacrylamide gel electrophoresis), NaOH (anhydrous pellets), HCl (37 wt% solution), phosphate buffered saline (PBS) tablets, and polyethylene glycol (PEG, 35 kg/mol).

ASTM International research grade type 1 ultrafiltered water, hereon referred to as MQ-water, was used for diluting all aqueous solutions and for rinsing the sensors in the polymerisation stages and before measurements.

3.2 Surface Functionalisation

3.2.1 Immobilisation of ATRP Initiator

Gold-coated SPR and QCM-D sensor surfaces were cleaned prior to grafting of ω-mercaptoundecyl bromoisobutyrate by piranha wash (3:1 v/v of H_2SO_4/H_2O_2) for 20 minutes, followed by at least three volume exchanges of MQ-water, TL1 wash (5:1:1

v/v of $H_2O/H_2O_2/NH_4OH$ at 75°C) for 30 minutes, another three volume exchanges of MQ-water, and ultrasonication in anhydrous ethanol for at least 5 minutes.

Gold-coated MNW (multi-nanowells) and nanopore substrates were cleaned prior to grafting of ω-mercaptoundecyl bromoisobutyrate by washing in sodium hydroxide (10 mM), followed by at least three volume exchanges of MQ-water, TL1 wash (5:1:1 v/v of $H_2O/H_2O_2/NH_4OH$ at 75°C) for 30 minutes, another three volume exchanges of MQ-water, and one volume exchange of anhydrous ethanol. The MNW were further cleaned by ultrasonication in anhydrous ethanol for at least 5 minutes.

Clean surfaces were immersed in initiator solution (2 mM ω-mercaptoundecyl bromoisobutyrate in anhydrous ethanol). The substrates were exposed for 12–18 hours. After incubation, the substrates were thoroughly rinsed in analytical grade ethanol for 1 minute and then dried with N_2.

3.2.2 PHEAA Polymerisation

Surface-initiated activator regenerating electron-transfer ATRP was used to create PHEAA polymer brushes in a manner similar to standard ATRP protocols [72, 50, 57]. A binary solvent mixture of methanol and water (3:1 v/v of $MeOH/H_2O$) was added to a screw-top jar. In this mixture N-(2-hydroxyethyl)acrylamide monomer (3.0 g, 0.65 M) and $CuBr_2$ (2.5 mg, 280 µM) was dissolved and sonicated for 5 minutes. Afterwards Me_6TREN (30 µl, 2.8 mM) was injected into the vortex while stirring with a magnetic stirrer.

Surfaces coated with an initiator monolayer were placed into the jar containing the polymer solution, which was then equipped with a septa and wrapped in parafilm before degassing with N_2 for 60 min. L-Ascorbic acid (20 mg, 227 mM) was dissolved in 0.5 ml MQ-water in a separate round-bottom flask and degassed with N_2 for 10 minutes. The reaction was initiated by the addition of L-ascorbic acid using a needle.

To terminate the reaction, the surfaces were removed from the polymerisation mixture and immersed in anhydrous ethanol. This was followed by at least three volume exchanges of MQ-water and analytical grade ethanol, and then dried with N_2.

3.3 Surface Sensitive Techniques

3.3.1 SPR Measurements and Analysis

SPR measurements were performed with a Bionavis multiparameter SPR Navi 220A instrument equipped with 670, 785, and 980 nm laser diodes. Data in Figures and Tables are shown for either 670 nm or 785 nm. The decay length of the evanescent field is usually defined as the distance over which the wave decays to $1/e$, or about 37%, of its maximum intensity. It can be seen as the maximum effective distance away from the surface from which accurate measurements can be done. Using longer wavelength laser diodes increases the effective decay length [73].

As was mentioned earlier, Equation 2.4 can be used to estimate the decay length in water at various wavelengths. The dielectric permittivity of water ε_d for visible light is 1.77. The real part of the metal dielectric permittivity ε'_m, for a 53 nm gold thin film, at various wavelengths was obtained from Yakubovsky et al. [74]. This is a slightly thicker gold film then what was used in this thesis, but should not have a large impact. All SPR gold coatings in this thesis were 50 nm.

Table 3.1 shows the value of ε'_m at the different wavelengths, and the estimated decay lengths obtained from Equation 2.4. The estimated values are similar to what has been previously experimentally determined. For 670 nm the decay length was measured to 226 nm [67], while for 785 nm it was measured to 320 nm [75].

Table 3.1: Estimation of decay length of the evanescent field in water. Data on ε'_m was obtained from Yakubovsky et al. [74]. ε_d was assumed to be constant.

λ (nm)	ε'_m	δ (nm)
670	-15.80	226
785	-25.51	343
980	-44.38	575

Gold coated SPR sensors functionalised with PHEAA polymer brushes were cleaned prior to use by at least two volume exchanges each of analytical grade ethanol and MQ-water. This was followed by rubbing the backside with lens tissue soaked in analytical grade ethanol, another volume exchange of analytical grade ethanol, and drying with N_2. After use, the sensors were thoroughly cleaned with MQ-water and analytical grade ethanol, and dried with N_2.

PBS was used as a running buffer at a flow rate of either 25 µl/min or 100 µl/min. All measurements were performed at 25℃. PBS buffers were prepared the same day of each experiment, degassed under vacuum in an ultrasonication bath, and filtered with a 0.2 µm syringe filter. PBS buffers were adjusted to within 0.01 units of the target pH using 1 M HCl or NaOH, and corrected after the addition of analytes. At the start of each measurement 35 kDa PEG or bovine serum albumin (BSA) at a concentration of 10 mg/ml in PBS, or higher, was injected for use in bulk response compensation. Each injection that was performed in the SPR was corrected.

The dry thickness of PHEAA was determined by fitting Fresnel models implemented in MatLab as described in detail by G. Ferrand-Drake del Castillo et al. [49, 42, 64, 37]. At least two measurements in air were performed for all samples to verify no significant signal drift occurred due to adsorption of moisture. When calculating the exclusion heights, a sensor surface that had been treated identically with washing, but without any initiator SAM or polymer brush coating, was used as a reference when fitting the Fresnel models. Fresnel models were fitted relative to an averaged reflectivity spectrum selected before and after the injection of a non-interactive probe, as described in detail by Emilsson et al. [57].

3.3.2 QCM-D Measurements and Analysis

QMC-D measurements were performed with a Q-Sense E4 instrument (Biolin Scientific) and a peristaltic pump to both control the flow of running buffer and to inject the PMAA and protein samples. All injections were performed at a flow rate of 150 µl/min and a temperature of 25℃. PBS was used as a running buffer in all measurements. This was prepared the same way as for the SPR measurements. When analysing the data in the QCM-D chromatogram, the frequency change was normalised relative to the value of the overtone as $\Delta f = \Delta f_n/n$. The dissipation change was not normalised.

Gold coated QCM-D sensors functionalised with PHEAA brushes were cleaned prior to use by at least two volume exchanges each of analytical grade ethanol and MQ-water and drying with N_2. After use, the sensors were cleaned with at least five volume exchanges of MQ-water, followed by one volume exchange of analytical grade ethanol, and drying with N_2.

3.3.3 FTIR Measurements and Analysis

Fourier transform infrared spectroscopy (FTIR) measurements were performed with a PerkinElmer FT-IR Spectrometer. All measurements were performed in air, and a sensor surface that had been treated identically with washing, but without any immobilised initiator or polymer brush coating, was used as a reference when calculating the absorbance of the sensor coating.

3.4 Fluorescence Measurements

Fluorescence measurements were conducted using a Zeiss Axio Imager Z2 upright microscope equipped with a ZEISS Axiocam 305 Color Microscope Camera and an Andor iXon Ultra 888 EMCCD camera. The Zeiss Axiocam was used for darkfield imaging and the Andor camera was used for fluorescence detection. All continuous injections were performed with a NE-1000 syringe pump for flow control. Measurements were performed at room temperature at a flow rate of 150 µL/min unless otherwise noted. Images were taken either every 5 seconds or 10 seconds at either 25 ms, 100 ms or 200 ms exposure times depending on the fluorescent molecule used and whether the image was taken during or after injection. Images taken during an injection had lower exposure times to not oversaturate the camera.

Multi-nanowell and nanopore chips coated with PHEAA polymer brushes on the gold side were cleaned prior to use by at least two volume exchanges each of analytical grade ethanol and MQ-water and drying both sides with N_2. Subsequently, the chip was placed inside a flow cell and the chamber was filled with PBS.

3.4.1 NHS-Amine Coupling Reaction

NHS-modified fluorescent molecules were attached to PMAA by an NHS-Amine coupling reaction. Figure 3.1 shows the reaction mechanism of the NHS-amine coupling. 10.0 mg α-amino terminated PMAA (MW 5 kg/mol) was dissolved in 9 ml PBS at pH 7.5. Solution was sonicated for 5 minutes and filtered with a 0.2 µm syringe filter. The pH was adjusted to a pH between 8.3 and 8.5, which is the optimal range for the reaction [76], using 1 M HCl or NaOH. 0.5 mg NHS-modified Fluorescein or 0.3 mg NHS-modified Sulfo-Cyanine3 was dissolved 1 ml of dimethyl sulfoxide (DMSO). This corresponded to 2:1 molar excess of PMAA and 4:1 molar excess of PMAA respectively.

The PBS mixture was stirred at a rapid rate and the DMSO mixture was injected into the vortex. Reaction was conducted over at least 1 hour. Solution was filtered with a 0.2 µm syringe filter. The pH was adjusted to pH 4.0 or 7.5 after the reaction was complete for use in a measurement.

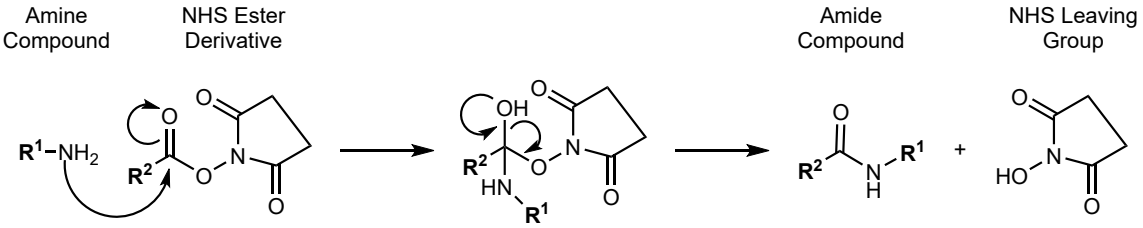

Figure 3.1: Reaction mechanism of the NHS-Amine coupling.

3.4.2 Nanowell Imaging

Interactions and molecular trappings in multi-nanowells were measured using a 50x objective. Injections were done on the gold side of the chip. During measurements, the camera was centred at the division between the side with nanowells and the side with plain gold. The fluorescence was analysed by defining a 20x20 µm^2 square on both sides and comparing the contrast between the two sides.

The nanowells were fabricated on a gold coated fused silica substrate using colloidal lithography, as described by Malekian et al. [77]. All samples were fabricated with 50/50 coverage of nanowells. Half of the sample consisted of multi-nanowells, while the other half was untreated gold. This allowed the untreated gold to function as an intrinsic reference for comparing any change in contrast over the nanowells. Contrast is in this thesis defined as the ratio of fluorescence intensity over the nanowells and over the intrinsic reference. Figure 3.2 shows SEM images of the multi-nanowells, including a cross-section of a single nanowell and an overview of the patterning.

When conducting fluorescence measurements, samples with both 120 nm diameter nanowells and 200 nm diameter nanowells were used. However, samples with 120 nm diameter nanowells were preferred as the total surface coverage of gold was the same. Equation 3.1 shows the relative change in surface area of gold when a hole is

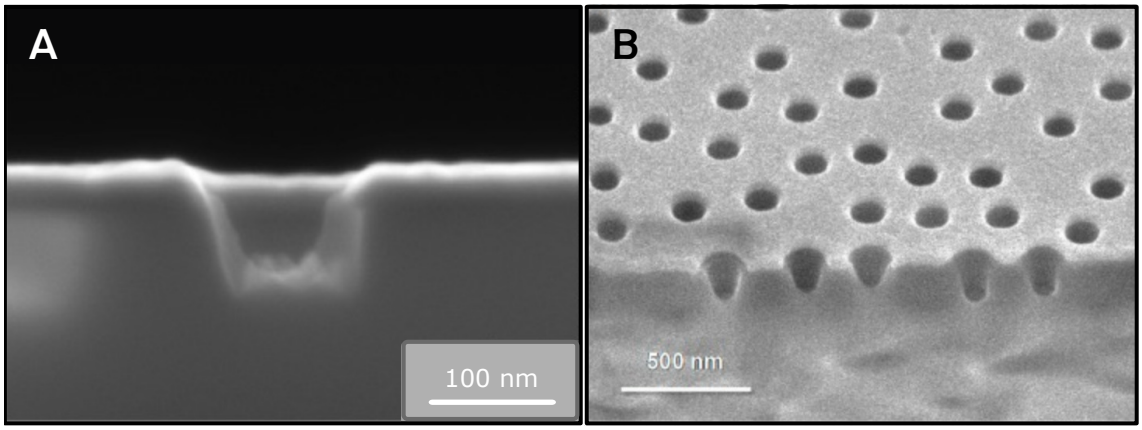

Figure 3.2: SEM images of multi-nanowells. Images were taken from Malekian et al. [77]. (A) Zoomed in image of the cross-section of one of the nanowells. (B) An overview of the multi-nanowell patterning.

introduced on the surface. Details on the derivation of this expression are given in Appendix A. Here r is the radius of the nanowell, and h is the thickness of the gold layer. All samples used in this thesis had a 30 nm thick gold film. Therefore, when $r = 60$ nm the area lost from creating the hole is the same as the area gained from the inside of the wall. Overall, the surface area of gold has not changed.

$$\frac{A_{\text{hole}}}{A_{\text{wall}}} = \frac{r}{2h} \tag{3.1}$$

Using the same fabrication protocol, Malekian et al. [77] characterised the 120 nm diameter nanowells to be 150 nm deep, and this was assumed to be the depth of the nanowells used in this thesis as well. No measurements were made for the 200 diameter nanowells. However, the vertical selectivity of the etching makes it highly likely that the 200 nm diameter nanowells were approximately 150 nm deep as well. This would give the 120 nm diameter nanowell an internal volume of 0.0017 μm^3, and the 200 nm diameter nanowell an internal volume of 0.0047 μm^3.

3.4.3 Nanopore Imaging

Transport through nanopores was measured using a PlanApochromat 63× water immersion objective (NA = 1.0) and a 50 µL droplet of PBS buffer was placed on top of the gold side. The injections were done on the Si_3N_4 side of the chip. The fluorescence was analysed by defining a 10x10 μm^2 square at set distances from the membrane edge and comparing the contrast on the gold side to that over the membrane. The fluorescence coming through the membrane represents the bulk fluorescence coming from fluorophores on the other side of the membrane. This should be relative constant and should thus serve as a good reference. If fluorescent cargo were able to move freely through the nanopores the concentration inside the droplet would reach the bulk concentration.

The nanopores were fabricated on 50 nm thick 140x140 μm^2 Si_3N_4 membranes using electron beam lithography, as described by Malekian et al. [78]. All samples were fabricated with 80 nm diameter nanopores. This is approximately the same size as the outer channel of the NPC and the nanopores were meant to give a comparative system. A 30 nm gold coating was deposited on the membrane to allow attachment of a PHEAA brush. Figure 3.3 shows SEM images of a nanopore array, including a cross-section of a single row of nanopores and an overview of the patterning.

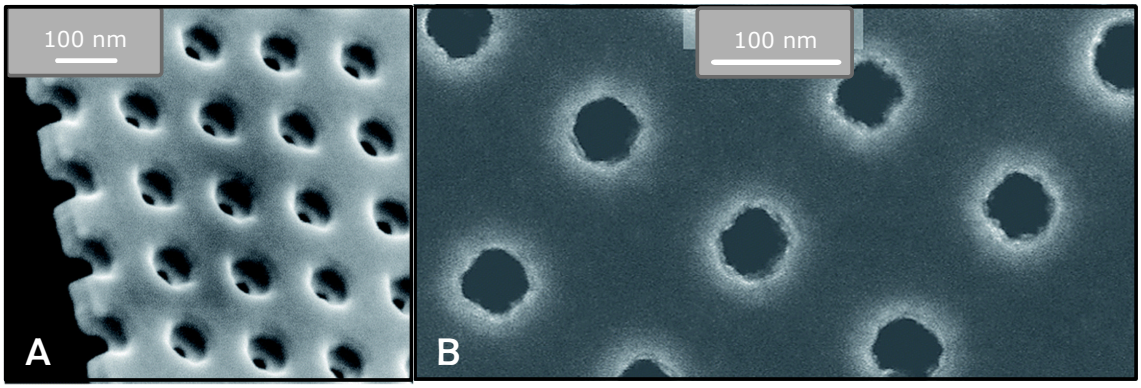

Figure 3.3: SEM images of nanopore arrays. Images were taken from Malekian et al. [78]. (A) The cross-section of a single row of nanopores. (B) An overview of the nanopore array patterning.

3.5 Molecular Interaction Kinetics

The interaction kinetics and equilibrium affinity between an analyte and a receptor can be determined by utilising Langmuir kinetics, assuming that the response from the equilibrated resonance response upon injection of the analyte is proportional to the surface coverage of the receptor. According to Langmuir an interaction process is a reversible process between adsorbent and adsorbate as shown in Equation 3.2 [79]. Here a complex AB is formed from an adsorbent A and an adsorbate B.

$$A + B \rightleftharpoons AB \tag{3.2}$$

interaction to a surface is driven by an associative process and desorption by a dissociative process. The association process is dependent on the concentration of analyte during the concentration, and a higher concentration will make the analyte adsorb faster. The concentration is assumed to be constant during interaction measurements as new analyte is constantly being supplied by a flow. With pure Langmuir kinetics, at any given time the change in surface coverage γ is shown in Equation 3.3 [62]. Here C_0 (M) is the concentration of analyte, κ_{on} ($M^{-1}s^{-1}$) the association rate constant and κ_{off} (s^{-1}) the dissociation rate constant.

$$\frac{d\gamma}{dt} = C_0\kappa_{on}\Big(1 - \gamma(t)\Big) - \kappa_{off}\gamma(t) \tag{3.3}$$

3.5.1 Two Independent Modes of interaction Model

A solution to this first-order differential equation has been shown in previous works [62, 67]. However, when modelling the interaction between PMAA and PHEAA in this work a lack of first-order kinetics was observed. This was believed to be caused by two independent modes of ternary interaction, i.e., interaction within the brush, between PMAA and PHEAA. To account for this lack of first-order kinetics, a two-state interaction model was used which assumed that PMAA could interact with PHEAA with two different affinities and configurations. This has been suggested to occur for macromolecular interactions in PEG [80, 81].

In the model the dynamics are described as a system of two independent binding processes. Equations 3.4a and 3.4b shows the time evaluation of the surface saturation of both configurations. Here $\gamma_i(t)$ is the fractional surface coverage of each mode of interaction at a given time, $\kappa_{\mathrm{on},i}$ are the association constants, and $\kappa_{\mathrm{off},i}$ are the dissociation constants. $\gamma_i(t)$ describes a segmental area of a total area, and is therefore dimensionless in all expressions.

$$\frac{d\gamma_1}{dt} = C_0\kappa_{\mathrm{on},1}\Big(1-\gamma_1(t)\Big) - \kappa_{\mathrm{off},1}\gamma_1(t) \tag{3.4a}$$

$$\frac{d\gamma_2}{dt} = C_0\kappa_{\mathrm{on},2}\Big(1-\gamma_2(t)\Big) - \kappa_{\mathrm{off},2}\gamma_2(t) \tag{3.4b}$$

The system of differential equations describes the total occupation Γ of binding sites on the surface. After the injection was over and PMAA began to dissociate from the surface the concentration in the liquid bulk was assumed to be $C_0 = 0$. This simplified the system of differential equations into two independent processes. The differential equations were integrated and combined as shown in Equation 3.5. Here Γ and A are both dimensionless and based on the response obtained during the SPR measurement. Details on the derivation of this expression are given in Appendix A.

$$\Gamma(t) = \mathrm{A}\exp\left(-\kappa_{\mathrm{off},1}t\right) + (1-\mathrm{A})\exp\left(-\kappa_{\mathrm{off},2}t\right) \tag{3.5}$$

At equilibrium, the association to the binding sites is equally fast as the dissociation from the binding sites for both processes. This generates a boundary condition that the change in either process is zero. The equilibrium distribution of the two processes were solved analytically as shown in Equations 3.6a and 3.6b. Here $\Gamma_i(t)$ is the total surface coverage, Γ_{max} is the saturation limit for a mode of interaction, C_0 is the bulk concentration and KD_i is the affinity constant of the mode. Details on the derivation of this expression are given in Appendix A.

$$\frac{\Gamma_1}{\Gamma_{\mathrm{max},1}} = \frac{C_0}{C_0 + \mathrm{KD}_1} \tag{3.6a}$$

$$\frac{\Gamma_2}{\Gamma_{\max,2}} = \frac{C_0}{C_0 + \mathrm{KD}_2} \tag{3.6b}$$

When combined, Equations 3.6a and 3.6b demonstrates the total response from simultaneous interaction to the two modes. Equation 3.7 shows this total response. Here Γ is the measured response, and $\gamma_{\max}$ is the sum of saturation limits of the two modes of interaction. This model can be further extended with more independent modes of adsorptions using the same method of derivation shown in Appendix A.

$$\frac{\Gamma}{\Gamma_{\max}} = \frac{C_0}{C_0 + \mathrm{KD}_1} + \frac{C_0}{C_0 + \mathrm{KD}_2} \tag{3.7}$$

When conducting measurements on molecular interactions, both $\gamma(t)$ and $\Gamma(t)$ are correlated to the measured response in either SPR or QCM-D. In this thesis, it is assumed that $\Delta\Gamma(t) \equiv \Delta\Theta_{\mathrm{SPR}}$ and that $\Delta\gamma(t)$ is the normalised $\Delta\Theta_{\mathrm{SPR}}$.

4

Results and Discussion

The following chapter presents and discusses the main results and findings of this thesis. A short insight into the synthesis and characterisation of the PHEAA brushes are displayed first. This is followed by both a physical and mathematical analysis of the modes of interaction between PMAA and PHEAA, and what this means for the configurations with which PMAA can arrange itself within PHEAA. Then, selective diffusion measurements made of PMAA with attached fluorescent cargo is presented with a discussion on what this means for the potential of applying the suggested shuttle-cargo mechanism for selective continuous transport.

4.1 Characterisation of PHEAA Brush

A large part of this thesis was spent developing a synthesis protocol for grafting PHEAA brushes on gold coated surfaces. However, only the final protocol and the characterisation of the PHEAA brushes will be presented in this thesis. PHEAA was grafted onto gold coated surfaces using a monolayer of ω-mercaptounde-cyl bromoisobutyrate as both an anchoring point for the PHEAA chains and as an initiator for the SI-ARGET ATRP. The monolayer was grafted-to the gold surface via the thiol group on the initiator. It was then characterised in SPR by calculating the dry height of three SPR sensors that had been immersed in anhydrous ethanol with 1 mM ω-mercaptoundecyl bromoisobutyrate for 24 hours at room temperature. Figure 4.1 shows the measured dry heights for incident light at 670 nm, and the height difference between the two channels that serve as a homogeneity benchmark.

Once grafted-to a surface, ω-mercaptoundecyl bromoisobutyrate will self-assemble into a dense monolayer, driven by the strong gold-sulphur covalent bond and van der Waals interactions between chains [82]. The three SPR sensors used in the monolayer characterisation were all prepared in the same way, and a dry scan was taken before immobilization of the initiator to be used as an intrinsic reference. It was observed that the monolayer height given by the two channels differed with an average value of 1.07 nm. As the gold-sulphur covalent bond limits the initiator to only form a monolayer on the surface, this difference must be the intrinsic error between the two channels. Therefore, it must also be the comparative difference in height that a polymer brush grown on the surface can have between the two channels

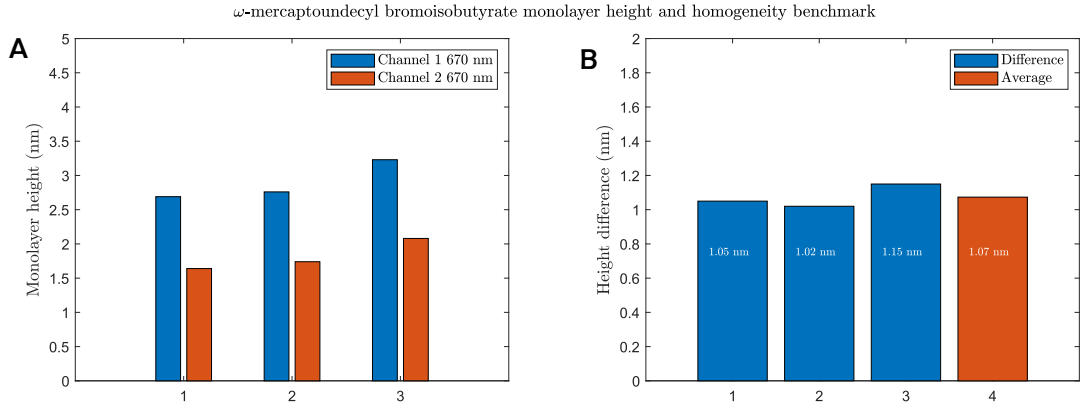

Figure 4.1: Measured dry heights of ω-mercaptoundecyl bromoisobutyrate in SPR. (A) Monolayer dry height ay 670 nm for both channels in the SPR. (B) Difference in dry height between the two channels that served as a benchmark for homogeneity.

and still be homogeneous. This served as the homogeneity benchmark.

As a confirmation that it was possible to graft PHEAA from a gold coated surface with ARGET ATRP, three surfaces with a PHEAA coating were characterised with FTIR. Figure 4.2 shows the FTIR spectra of three different SPR sensors that had been polymerised with ARGET ATRP for 30 minutes, 2 hours, and 3 hours, respectively. Note, these measurements were made before the reaction protocol was optimised, and therefore, are shorter than what would be expected from polymerisation's made later in the project.

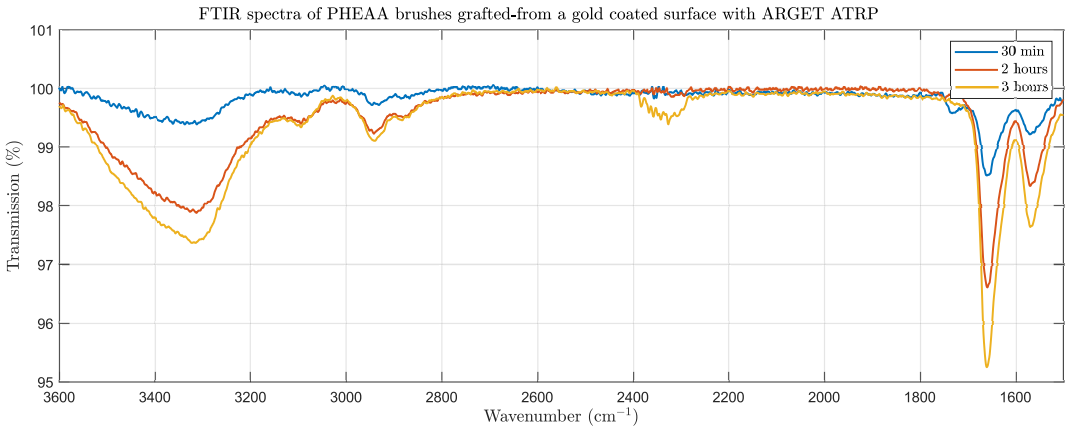

Figure 4.2: FTIR spectra of PHEAA brushes grafted-from a gold coated surface with ARGET ATRP. Three sensors were characterised that had been polymerised for 30 minutes (blue), 2 hours (red), and 3 hours (yellow).

The FTIR spectra showed a clear indication that PHEAA was present on the surface after 30 minutes polymerisation, when compared to a similar measurement done by Zhao et al. [83]. The two surfaces that had been polymerised for 2 and 3 hours gave a stronger absorbance. All measurements showed the same five distinct peaks at 3320 cm^{-1}, 3090 cm^{-1}, 2940 cm^{-1}, 1660 cm^{-1}, and 1570 cm^{-1}. These peaks

corresponded to N-H stretching in the acrylamide, O-H stretching in the alcohol, C-H stretching in the alkane, C=O stretch in the acrylamide, and N-H bending in the acrylamide [84]. The chemical structure of PHEAA is given in Appendix B. An additional peak was observed for the surface that had been polymerised for 3 hours at 2330 cm^{-1}. A broad peak in that FTIR region is often associated with O=C=O stretching in carbon dioxide and was likely an indication of contamination.

As FTIR measurements do not give quantitative information, it was not used further in this work other than to verify whether a polymerisation was successful or not. However, there are some potential uses of this technique, such as verification of whether proteins or other macromolecules had irreversibly bonded to the surface. Though, this avenue of analysis was not investigated further.

4.1.1 Optimisation of ARGET ATRP Protocol

When investigating how to optimise the PHEAA synthesis a general guideline by Zhu et al. was used [72]. It suggests that the most important parameters of a ARGET ATRP procedure is the ratios of copper catalyst, reducing agent, and catalyst ligand, as well as the polarity of the solvent. N-(2-hydroxyethyl)acrylamide was used as the monomer in all reactions at a concentration of 75 mg/ml in a mixture of anhydrous methanol and MQ-water. The reaction conditions were based on previous results by Matyjaszewski et al. [52], where ascorbic acid was successfully used as a reducing agent with $CuBr_2$ and Me_6TREN as a copper catalyst and ligand complex.

Me_6TREN was determined not to have a significant impact on the efficiency of ARGET ATRP and was chosen to be used in 1:10 molar excess relative to the $CuBr_2$ catalyst. In the continued optimisation, the effect of the amount of $CuBr_2$ catalyst, the amount of ascorbic acid, and the ratio of methanol/water in the solvent were investigated. Using a reduced factorial design, PHEAA was grafted-from gold coated surfaces for 60 minutes. Four replicates were made for each combination to give statistical significance. Table 4.1 shows the average dry height, and the swelling ratio, which is defined as the ratio of the measured wet height and dry height in SPR, that each combination gave.

Factorial effects were calculated using standard statistical methods, as described in Montgomery (2017) [85]. What can be derived from the continued investigation is that the overall height of PHEAA is equally dependent on the amount of $CuBr_2$, the amount of ascorbic acid, and the amount of MQ-water in the solvent. Since the goal of the optimisation was to achieve as high and dense brushes as possible, the optimal reaction conditions were with a low concentration of $CuBr_2$, a low concentration of ascorbic acid, and a large amount of MQ-water in the solvent. While the reaction conditions were expected to have a negative impact on the swelling ratio, the relative increase in brush height was deemed more significant.

Table 4.1: Dry heights and swelling ratios of PHEAA at four different combinations of $CuBr_2$ catalyst, ascorbic acid, and MQ-water, as well as the calculated effects of each of these three factors. Effects calculated according to Montgomery et al. [85].

$CuBr_2$ (mg)	Asc. Acid (mg)	MQ-water (%)	Height (nm)	Swelling
2.5	20	10	50.5	3.45
5.0	20	25	58.6	3.39
2.5	40	25	59.3	3.58
5.0	40	10	9.5	3.69

Effects	Height (nm)	Swelling
$CuBr_2$	-10.4	0.01
Asc. Acid	-10.1	0.11
MQ-water	14.5	-0.04

4.1.1.1 Further Optimisation

While the reaction protocol was not optimised more in this thesis, it is possible to optimise this reaction further to increase the accuracy with which the brush height and swelling ratio can be controlled. One way of achieving this would be to investigate the effect of exchanging the copper catalyst, the reducing agent, and the metal complex ligand, instead of the amounts of those factors. As was mentioned before, the reaction conditions were based on previous results by Matyjaszewski et al. [52], where $CuBr_2$, ascorbic acid and Me_6TREN was used successfully. However, different combinations of copper catalyst, reducing agent, and ligand could prove to be more successful than what was used in this thesis.

As was discussed with regards to Equation 2.1, decreasing the equilibrium constant will decrease the rate of polymerisation and offer more control to the reaction. With regards to the copper catalyst, the equilibrium constant increases with the strength of the X−Cu(II) bonds and decreases with the strength of the X−C bonds [40]. In Table 4.2 the bond strengths of X−Cu(II) and X−C when exchanging Br for Cl as a halogen [86]. $CuCl_2$ has been shown to work as a copper catalyst by Matyjaszewski et al. [87], and could serve as a replacement for $CuBr_2$.

Table 4.2: Bond strengths of X−Cu(II) and X−C with Br and Cl [86].

Halogen (X)	X−Cu(II) (kJ/mol)	X−C (kJ/mol)
Br	331.0 ± 25	318.0 ± 8.4
Cl	377.8 ± 7.5	394.9 ± 13.4

Exchanging $CuBr_2$ for $CuCl_2$ would increase the bond strength of both X−Cu(II) and X−C. Meaning, that it becomes both harder to regenerate the catalyst and stop the polymerisation, as well as harder to activate the dormant species and activate the polymerisation. However, the increase in the X−C bond strength is greater than the increase in the X−Cu(II) bond strength. Therefore, exchanging $CuBr_2$ for $CuCl_2$ as the copper catalyst could decrease the rate of polymerisation.

Another possibility for optimisation would be to exchange Me_6TREN for another ligand. $CuCl_2$ have been shown by Matyjaszewski et al. to function with TPMA, PMDETA and dNbpy as a ligand instead of Me_6TREN [87], and could allow more control over the PDI. For instance, PMDETA has been shown by Kwak et al. to give a lower polymerisation rate than Me_6TREN [88]. Similarly, TPMA has been shown by Jakubowski et al. to give a higher control over the polymerisation than Me_6TREN [48]. This was ascribed to a higher real concentration of Cu species in the system, since TPMA binds more strongly to Cu. Comparing PMDETA and TPMA, it has been shown Matyjaszewski et al. that $CuCl_2$ forms a more stable complex with TPMA than it does with PMDETA [87]. Therefore, exchanging Me_6TREN for TPMA as the ligand could increase the control of the PDI.

4.1.2 PHEAA Post-Injection Stability

As was mentioned earlier, one of the main criteria of the PHEAA brush is that it has a high degree of resistance against non-specific adsorption of proteins. In future research and application of the shuttle-cargo system proposed and investigated in this thesis it is of utmost importance that macromolecular cargo is unable to enter the brush, or undergo primary adsorption on the barrier, without being attached to a synthetic shuttle. PHEAA has been shown to exhibit a high degree of resistance against non-specific adsorption of proteins by Zhao et al. [35].

Whether the brush retains its conformation after the injection of a macromolecule can be investigated by injection of the same non-interactive probe before and after the experiment has been conducted. A solution of 15 mg/ml 35 kDa PEG in PBS buffer was injected both as the first and last injection and the measured heights were compared. These exclusion heights were determined to be 99.8 nm before injection and 99.6 nm after injection, respectively. This indicated that the polymer brush did not change its conformation. For reference, the dry height of the polymer brush on this specific sensor was 25.4 nm, with a degree of hydration at 75%.

4.1.3 pH Dependence of Exclusion Height

In this work injections were performed at different pH's, ranging from 4.0 to 7.5, It was, therefore, important that the PHEAA brush retained its height and properties at all pH's. While changes in thickness upon variation of the pH has been observed for polyelectrolyte brushes [49], it is not expected from neutral brushes like PHEAA. To verify this a solution of 15 mg/ml 35 kDa PEG in PBS buffer was injected in the SPR at both pH 4.0 and pH 7.5 and the responses were measured. All injections

were done at a flow rate of 20 µl/min and the data were obtained at 670 nm. Figure 1.7 shows the results of these injections, as well as the plot in SPR vs TIR angle for one injection at each pH.

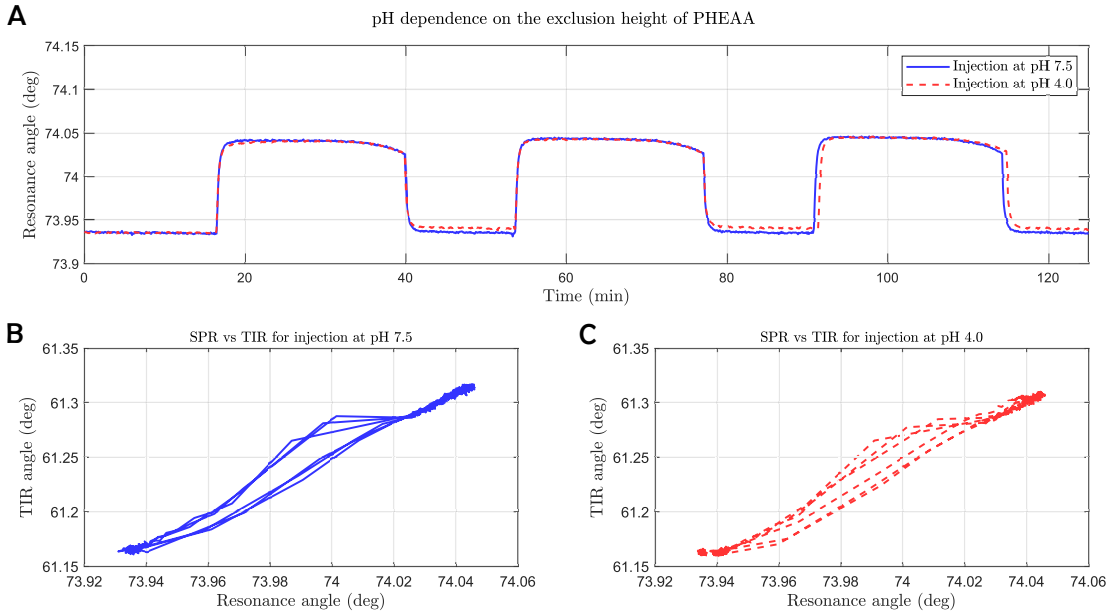

Figure 4.3: pH dependence on the exclusion height of PHEAA. (A) SPR sensorgram of three injections at both pH 7.5 and pH 4.0. (B) SPR vs TIR diagram for 35 kDa PEG at pH 7.5. (C) SPR vs TIR diagram for 35 kDa PEG at pH 4.0.

No apparent change in the bulk response was observed at either of the two pH's, and both gave linear SPR vs TIR diagrams that indicated that no interaction occurred. At pH 7.5 the exclusion height was calculated to be 100.8 nm, and at pH 4.0 the exclusion height was calculated to be 100.0 nm. This was within the error of margin of the non-interactive probe method.

4.2 PMAA-PHEAA Interaction Study

As a reminder, the aim of this thesis was to investigate the viability of using PMAA and PHEAA as a shuttle and diffusion barrier for replicating the nuclear transport cycle of the nuclear pore complex. To do this, the interaction characteristics of the two polymers had to be evaluated. This was done using non-functionalised PMAA (PDI 1.8, M_N 5 kDa) and the interaction with PHEAA was evaluated using SPR and QCM-D measurements. All measurements made with SPR were compensated with a non-interactive probe, a solution of either 15 mg/ml 35 kDa PEG in PBS or 15 mg/ml BSA in PBS, according to the method suggested by Svirelis et al. [67].

4.2.1 pH Dependence of PMAA-PHEAA Affinity

As was mentioned before, the degree of protonation of the acidic monomers in PMAA directly affects the degree of interaction between PMAA and PHEAA. By actively

controlling the degree of protonation, and by effect the affinity of PMAA to PHEAA, the associative and dissociative processes could be fine-tuned to optimise the diffusion characteristics of the synthetic shuttle through the diffusion barrier. In theory, the shift in affinity was expected to occur at, or slightly below, the pKa value of the methacrylic acid monomer, where the carboxylic acid groups transform from primarily being in a charged state to a protonated state. The pKa value of a methacrylic acid monomer is 4.65 [89]. However, it has been shown by Dong et al. that the effective pKa of an acid group can be changed by incorporation into a macromolecule such as a polymer [90]. Furthermore, it has been shown by Haines et al. that when carboxylic acids are anchored close to one another, such as in a polymer, that the pKa can change. This was ascribed to hydrogen bonding between the acid and the conjugated base [91]. So, the effective pKa of PMAA is not known. However, it was assumed to be close to that of the methacrylic acid monomer.

To determine the pH range over which the PMAA shuttle begins to interact with the PHEAA polymer brush, a solution of 0.10 mg/ml PMAA in PBS was injected at a flow rate of 200 μl/min at sequentially lower pH's. In the QCM-D chromatogram, both the change in frequency and energy dissipation was measured. A 180 nm hydrated PHEAA brush was grafted-from a gold coated QCM-D sensor to allow the different overtones to be used to compare how deep into the brush PHEAA was able to penetrate. Figure 4.4 shows three injections made between pH 4.5 and pH 4.1. Δf_n was normalised as per its overtone to better represent the relative change in frequency at each penetration depth. At pH's above the pKa of the methacrylic acid monomer, no interactions were observed.

No apparent change in frequency nor dissipation was observed at pH 4.5. The small drop in frequency did not show any hysteresis once the flow cell was rinsed with buffer at the same pH, which indicated that the drop was due to liquid exchange. The liquid exchange rate was estimated by measuring the time it took the TIR angle to return to the baseline after the injection stopped. At a flow rate of 20 ml/min the liquid exchange rate was 30 seconds. This change was restored when rinsing at pH 7.5. At pH 4.3 there was no apparent change in energy dissipation, and the frequency change was mostly negligible. However, a small hysteresis was observed in the third and fifth overtones, but not in the higher overtones, which indicated that PMAA was able to enter the outmost layers of the PHEAA brush where the degree of hydration is higher. The difference in hydration throughout the brush is because of the parabolic distribution of monomer units [28]. A lower concentration of monomer units near the edge of the brush allows more water to surround the polymer chains.

At pH 4.1, an apparent drop and hysteresis in both frequency and energy dissipation was observed for all overtones. This indicated that PMAA had entered the PHEAA brush, and that the resulting crosslinking between PMAA and the PHEAA chains had decreased the viscoelasticity of the adsorbed film. At pH 4.1 the degree of protonation is high enough to allow PMAA to form enough hydrogen bonds with PHEAA to not be rejected by it. The interaction was reversible, and rinsing at the

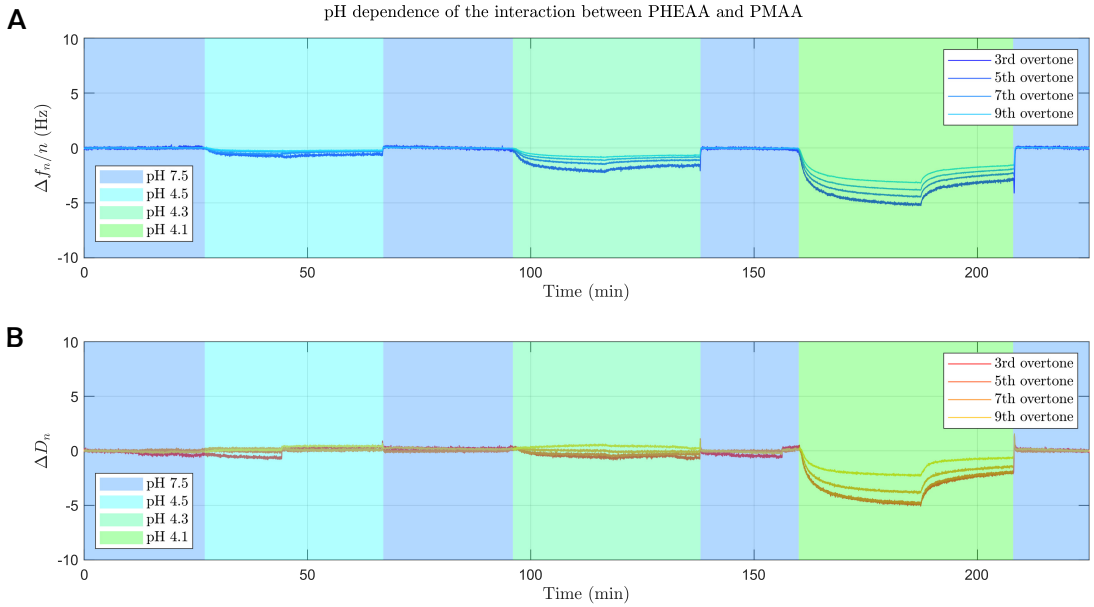

Figure 4.4: QCM-D chromatogram of injection of PMAA over PHEAA at sequentially lower pH's. (A) Normalised frequency change at the third, fifth, seventh and ninth overtones. Higher overtones have a brighter shade of blue, and lower pH's are coloured with greener shades. (B) Energy dissipation change at the third, fifth, seventh and ninth overtones. Higher overtones have a brighter shade of red.

same pH led to an increase in both frequency and energy dissipation. This should allow PMAA to continuously form and break bonds and, by doing so, diffuse through the brush. At lower pH's, the interaction was observed to be even stronger, and the dissociation from the brush took longer. Eventually, PMAA was irreversibly bound to the brush. pH 4.0 was chosen at the working pH for the interactions for the remainder of this thesis, as it both allowed a lot of PMAA to bind, while still having a good dissociative ability.

4.2.2 Dissociation Model Fitting

As previously established, PMAA interacted and bound strongly with a PHEAA brush at pH's below 4.1, while repulsed and released from the brush at pH 7.5. A kinetics study was conducted to determine and fit statistical models for the association and dissociation of said interactions. This was measured in the SPR using sensors with a 200 nm thick PHEAA brush. In the SPR, the 785 nm laser diode was used for the measurements instead of the usual 670 nm laser diode, since the decay length of the 670 nm laser diode, i.e., 226 nm, was on the same size scale as the height of the brush. The 785 nm laser diode has a decay length of 343 nm, which was sufficiently long for the experiments. The benefit of having a high polymer was the additional volume offered in the brush structure.

Solution of PMAA in PBS were injected at a flow rate of 100 μl/min in the SPR at

sequentially higher concentrations. Figure B.4 in Appendix B shows the overlapping sensorgrams from these injections. Two observations were made from the sensorgrams. One, that the dissociation had two distinct regions, where one fast initial dissociation was followed by a much slower dissociation. Two, that the resonance angles during the slower dissociation converged at a concentration above 4.0 mg/ml.

Figure 4.5 shows the dissociation model fitting of the sensorgrams in Figure B.4 in Appendix B. The dissociative phases of the sensorgrams were normalised based on the value when the TIR angle reached the baseline, ensuring that only the pure diffusion out into buffer was considered, and the last five values before the dissociation was terminated by injecting PBS at pH 7.5. At a flow rate of 100 μl/min, the liquid exchange rate was calculated to be 10 seconds. This was deemed sufficiently short as to not mask any short residence time interactions. A model that only allowed one mode of interaction and a model that allowed two independent modes of interaction were fitted to the dissociation.

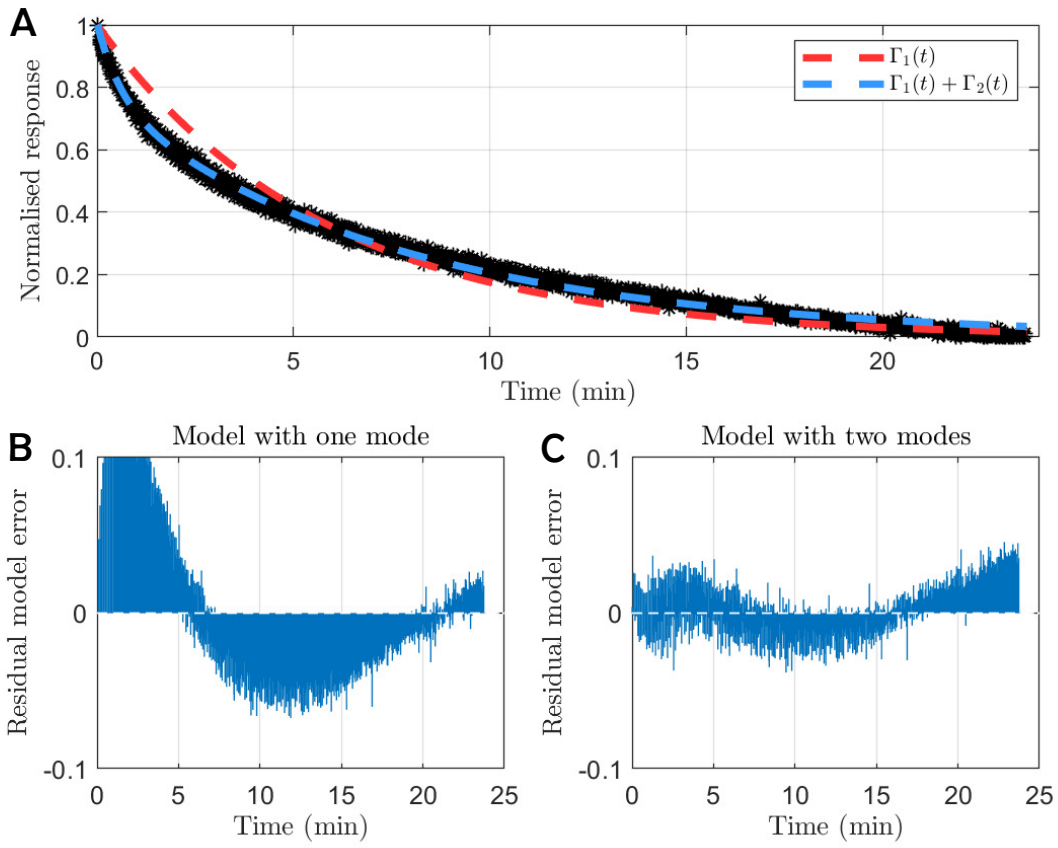

Figure 4.5: Model fitting and residuals of PMAA dissociating from PHEAA. (A) Normalised sensorgrams during the dissociative phase fitted with both a one-mode model and a two-mode model. (B) Residual model errors from the one-mode model. (C) Residual model-errors from the two-mode model.

It was observed that the dissociation had a distinct lack of first-order kinetics during

the first 5 to 10 minutes of dissociation. As shown in Figure 4.5B, the model with one state of interaction had a clear residual deviation during the initial dissociation. When a model that allowed two independent modes of interaction was fitted to the data, the residual deviation in that time interval improved. However, a significant linear deviation was still observed in the latter stages of the dissociation.

Usually, a linear deviation in an SPR sensorgram arise from a mass transport limitation [92]. The observed linear deviation could be explained by the PMAA entangling itself within the PHEAA brush. The additional time it takes PMAA to untangle from PHEAA and then release would facilitate a diffusion limitation. Figure B.6 in Appendix B shows the two-mode model with and without an additional linear compensation. Fitting the model with an additional linear term eliminated the linear increase in the residual error as well as some of the exponential residual error that remained in Figure 4.5C. The source of the linear deviation was not investigated further. However, it is possible that a more sophisticated differential model could be developed to increase the knowledge of the system. For instance, Emilsson et al. suggested that a two-mode model with an additional sequential transition from the harder binding mode to the weaker binding mode could be used to describe higher-order kinetics of multivalent interactions with polymer brushes [81]. Also, if the linear contribution were from a much slower exponential component, which would appear linear, it could also indicate that there exists a third mode of interaction.

Table 4.3 shows the model parameters of the one-mode model and two-mode model. For reference, the names of the parameters are based on Equation 3.5. The two-mode model showed a higher goodness-of-fit at 99.4%, compared to 94.9%.

Table 4.3: Model parameters for the one-mode and two-mode models.

Modes	A	κ_1 (min^{-1})	κ_2 (min^{-1})
1	1.0000	0.1741	0.0000
2	0.7639	0.1315	1.6150

What could be interpreted for the two-mode model fitting was that there were two concurrent dissociation processes occurring. Furthermore, the one-mode model primarily describes the slower dissociation, as the rate constant is similar to what was achieved with the two-mode model. A slower rate constant indicated that PMAA had undergone a stronger binding in that mode. In the two-mode model, approximately 3 out of 4 of all PMAA occupies one of the stronger modes of binding. The residence time of PMAA in that mode, defined as the reciprocal of the associated rate constant, was 7 minutes and 36 seconds. Meanwhile, 1 out of 4 of all PMAA occupies one of the weaker modes of binding. The residence time of PMAA in that mode was 37 seconds. This shows that there are two different modes of interaction. The numerical values of the model were based on the value that was reached in the plateau in Figure B.4 before injection of PBS at pH 7.5.

A dissociation measurement was performed over 6 hours, and over that time the

resonance angle decreased to 40% of the initial value. A model was fitted to it and extrapolated, and a full dissociation was predicted to take up to 100 hours. Since the predicted residence time is on the scale of days, it would not contribute to PMAA's ability to diffuse through PHEAA. In fact, it could counteract PMAA's ability to move through a nanopore with a PHEAA barrier as the irreversible binding could lead to clogging. Diffusion over longer times were not investigated further.

4.2.3 Langmuir Equilibrium Model

The equilibrium characteristics of PMAA and PHEAA was investigated using SPR. A solution of PMAA in PBS at sequentially higher concentrations were injected at a flow rate of 25 µl/min. A slower flow rate was chosen to fully saturate the brush with PMAA. At the lower flow rate the liquid exchange rate was 25 seconds, which was on the same time scale that was observed for the fast dissociation mode. Therefore, the injections could not be used to compare the dissociation characteristics of the previous measurements. Ideally, when comparing affinity constants and dissociation constants the same measurements should be used. Figure B.5 in Appendix B shows the overlapping sensorgrams from these injections. Three observations were made from the sensorgrams. The two first were the same as was observed in Figure B.4; that the dissociation had two distinct regions, and that the resonance angles during the slower dissociation converged at a concentration above 4.0 mg/ml. Furthermore, it was observed that an injection at 0.1 mg/ml did not lead to a discernible fast dissociation, but instead immediately entered a plateau.

Figure 4.6 shows the equilibrium resonance shifts, and a fitted two-mode equilibrium model. A two-mode model gave a good fit, which confirmed that there exist two distinct modes of interaction. Furthermore, as shown in Figure 4.6B, at low concentrations only one of the two modes of interaction contributes to the equilibrium. This explains the observations made in Figure B.5, where the injection of a solution of 0.1 mg/ml PMAA in PBS immediately entered a plateau. That would correlate that equilibrium mode with the slower dissociation process, and indicate that PMAA attached stronger to PHEAA at low concentrations. A similar mode of interaction has been reported by Lim et al. with regards to the NPC [93], with what is called the Kaps-centric control model. It was found that low Kaps concentrations yielded long interaction times and low transport efficiency, whereas high Kaps concentrations yielded short interaction times and high transport efficiency.

Table 4.4 shows the model parameters of the two-mode equilibrium model. For reference, the names of the parameters are based on Equation 3.5. Since the modes were independent, it was possible to separate them in Figure 4.6B.

Table 4.4: Model parameters for the two-mode equilibrium model.

A_1	KD_1	A_2	KD_2
0.5512	0.5113	2.6430	43.480

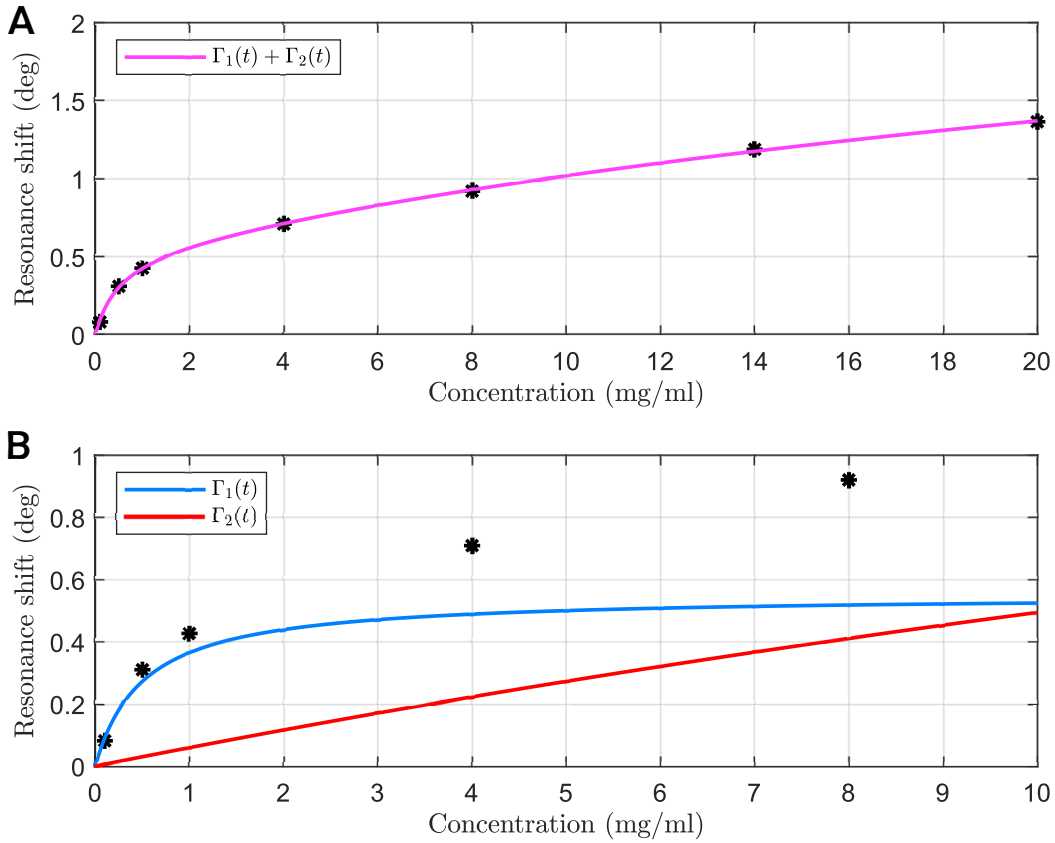

Figure 4.6: Equilibrium resonance shifts at sequentially higher concentrations of PMAA. (A) Two-mode model fitting to equilibrium resonance shifts. (B) Zoomed-in model fitting at low concentrations with the two modes separated.

What could be interpreted from the equilibrium model fitting was that the modes of interaction have two vastly different affinity constants. The stronger mode of interaction had an affinity constant of 0.5 mg/ml; meaning that at a concentration of 0.5 mg/ml, half of the active sites of that mode was occupied. It was observed in Figure 4.6B that the stronger mode of interaction was fully saturated at a concentration of 5 mg/ml. Furthermore, it explained the convergence in the plateaus that were observed in Figures B.4 and B.5 in Appendix B. At concentration higher than 5 mg/ml, all PMAA bonded in the weaker mode of interaction. The weaker mode of interaction had an affinity constant of 43.5 mg/ml. The model predicted that the PHEAA brush would be saturated, with a total resonance shift of 3.2 degrees, when the injected amount of PMAA reached a concentration of over 1 g/ml.

At low concentration, at which the transport would be conducted, it was assumed that the stronger mode of interaction dominated the effective equilibrium.

4.2.3.1 Suggested PMAA-PHEAA Interaction Mechanism

Based on the measurements made of the equilibrium and dissociation characteristics of PMAA and PHEAA, and in combination with the observations made when measuring the pH dependence on the affinity, an interaction mechanism between PMAA and PHEAA was suggested. As was observed in Figure 4.4, PMAA appeared to enter the outmost layers of the brush at a higher pH than it would enter the interior of the brush. An explanation for this is that PMAA is required to form more hydrogen bonds to enter the deeper areas of the brush. Furthermore, this would still be true when PMAA enters the brush fully at pH 4.0. As there is more coupled water where the monomer concentration is low, it would lead to less hydrogen bonding with the brush, and thus a weaker mode of interaction with the brush. Deeper inside the brush, it would form more hydrogen bonds with the brush, which in turn would mean a stronger mode of interaction and a slower dissociation.

Assuming that the proposed interaction mechanism was correct, it would make sense that as the PMAA was released from the stronger mode of interaction it would occupy a site of the weaker mode of interaction on its way out of the brush. This would explain, in part, the long dissociation time.

4.3 Nanowell Trapping

As shown in the previous section, PMAA selectively interacted with PHEAA at pH 4.0, while being rejected by PHEAA at pH 7.5. Substrates of fused silica with either 120 nm or 200 nm diameter nanowells were used to study if the interactions between PMAA and PHEAA would allow it to act as a shuttle, and move through a barrier of PHEAA polymer brushes and into a confined volume underneath. PHEAA was attached to a 30 nm gold film deposited on one side of the substrate. Nanowells were fabricated through the gold film and etched 150 nm into the substrate using colloidal lithography, as described by Malekian et al. [77].

Sensors were coated with PHEAA synthesised to dry heights that at least covered the radius of the nanowell. This ensured that all nanowells were covered and would prevent any macromolecules from moving through the barrier. PHEAA dry heights were determined with an SPR sensor that had been polymerised at the same time as the substrates. A notable exception was made for one substrate, which was used to analyse the response when the nanowell was not fully covered.

Fluorescent cargo covalently attached to PMAA was injected at pH 4.0 and pH 7.5. Transport was measured using an Andor iXon Ultra 888 EMCCD camera capable of capturing fluorescence intensity in a flow cell where liquid was injected over the gold side of the nanowells. PMAA that moved through the PHEAA polymer brush would be entrapped inside the nanowells and could be detected by the fluorescence camera. An illustrated example of the experimental setup is shown in Figure 4.7. Fluorescence intensity over the nanowells, coming from the fluorophores trapped inside the nanowells, was compared to the fluorescence intensity on the plain gold. In

analysis, the measured fluorescence was normalised relative to the intensity during injection. The fluorescence contrast was calculated as the percentual increase in fluorescence over the nanowells, relative to the gold. When the contrast was greater than a few percent there was fluorescent cargo trapped inside the nanowells.

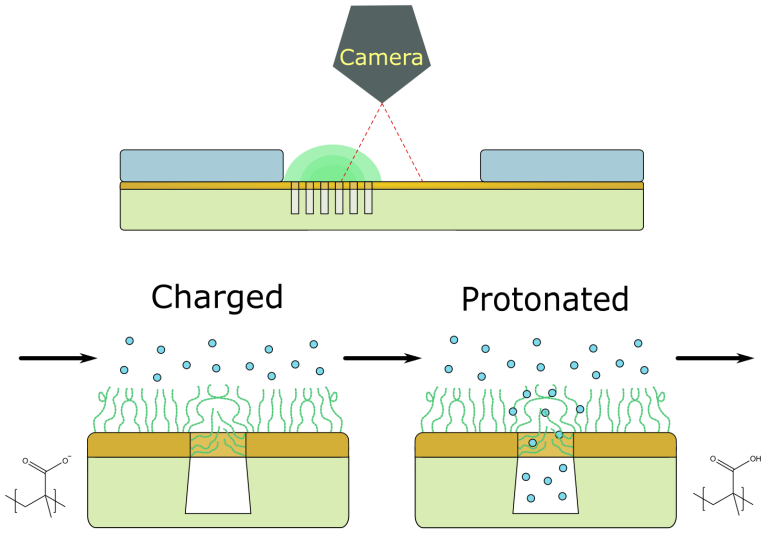

Figure 4.7: An Andor iXon Ultra 888 EMCCD camera was situated over the sensor so that it covered an equal amount of nanowells and plain gold. Images were taken of fluorescence coming from both the nanowells and from the gold reference. At pH 7.5 the nanowells were expected to not entrap any fluorescent cargo since the PHEAA brushes repels the PMAA, while at pH 4.0 the nanowells were expected to be open and allow access for the PMAA.

4.3.1 Coupling of Fluorescent Cargo

NHS-modified Fluorescein was attached to amine terminated PMAA using an NHS-Amine coupling reaction [76]. In the reaction PMAA was used in 2:1 molar excess to ensure that the Fluorescein coupled fully to PMAA. This minimised the total amount of uncoupled fluorophore adsorbed on the surface. The fluorescence was compared at pH 7.5 because of the lower fluorescence quantum yield of Fluorescein at pH below 6, as is shown in Figure B.7 in Appendix B. Any fluorescence at pH 4.0 was deemed to be diminished.

As confirmation that coupling the cargo did not prevent the shuttle from interacting with the barrier a series of injections with and without the shuttle was performed on the SPR. Shown in Figure 4.8 is the peak-to-peak comparison and dissociation curves of the injections with and without cargo. Three replicates of each sample were performed, and the average responses were used in the analysis. A solution of 1.0 mg/ml PMAA in PBS was used for injections, with PMAA in 2:1 molar excess in the sample with Fluorescein. At equilibrium, this correlated to a concentration inside the nanowells of $2 \cdot 10^{-19}$ mol/μm^3, which for the 120 nm diameter nanowells

and their internal volume of 0.0017 μm^3 gives $3.4 \cdot 10^{-22}$ mol shuttles inside each nanowell. This is the same as 205 polymer shuttles inside each nanowell, of which half are functionalised.

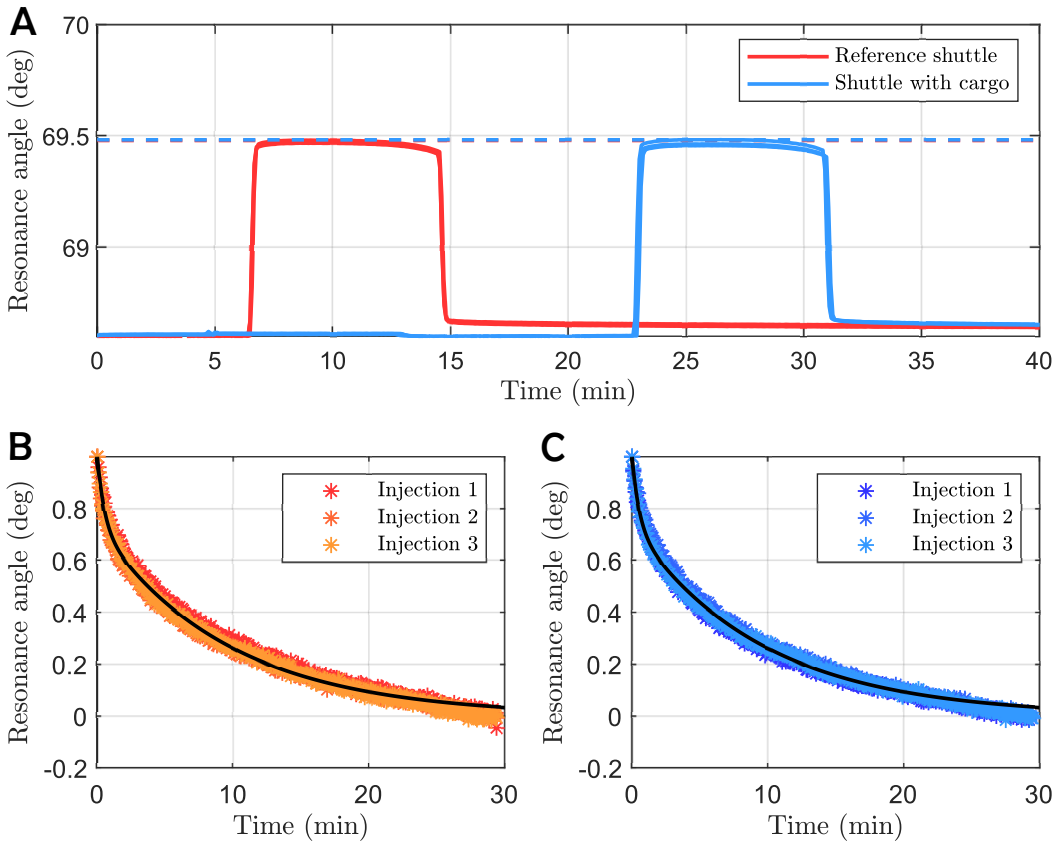

Figure 4.8: Sensorgrams and model fittings of PMAA on PHEAA with (red) and without (blue) attached NHS-modified Fluorescein cargo. (A) Three injection peaks each of PMAA on PHEAA with and without attached NHS-modified Fluorescein cargo. (B) Normalised dissociation without attached Fluorescein. (C) Normalised dissociation with attached Fluorescein.

It was noted in Figure 4.8A that there was no distinct difference in either the peak of the resonance shift nor the amount of retained signal after rinsing at pH 4.0. Any variation in the data could be explained in the small difference in concentration that may have been present between the two samples. This means that the attachment of NHS-modified Fluorescein did not prevent PMAA from being inserted into the PHEAA polymer brush. Note that PMAA was used in 2:1 molar excess in the NHS-amine coupling reaction. Therefore, the concentration of Fluorescein-modified PMAA was 0.5 mg/ml with an additional 0.5 mg/ml of amine terminated PMAA that had not reacted with an NHS-modified Fluorescein. However, this was assumed not to have an impact on the equilibrium peak shift or dissociation rate as even a slight change in affinity of half the analytes would be noticeable.

Normalised dissociation curves shown in Figures 4.8B and 4.8C were analysed with the same methods that were previously described. Normalisations were performed from the response where the TIR angle returned to its initial value, which indicated that no PMAA remained in the bulk liquid, and an average of the 5 last data points before the rinse stopped. A parallel dissociation model was fitted to the dissociation curves of amine terminated PMAA without attached Fluorescein, as shown in Figure 4.8B. The model was superimposed over the dissociation curves of Fluorescein-modified PMAA, as shown in Figure 4.8C. No difference in dissociation was observed before and after the amine terminated PMAA was modified.

When compared to the two-mode dissociation model fitted in the previous section, as shown in Table 4.3, the modes of dissociation were similar. 1 out of 4 PMAA dissociated from a weaker bond and 3 out of 4 PMAA dissociated from a stronger bond. The model parameters are given in Table 4.5. It was noted that the rate constants were shifted. While the fast dissociation was unchanged, the slow dissociation had decreased by almost 20%. However, it should be kept in mind that the rate constants determined in Table 4.5 were for a PHEAA brush with 100 nm exclusion height, while the rate constants determined in Table 4.3 were for a PHEAA brush with 200 nm exclusion height. Proteins have been shown to exhibit different dynamics when interacting with brushes of different thickness by Emilsson et al. [81]. However, it still interacted with two distinct modes of interaction.

Table 4.5: Normalised parallel dissociation model fitted to the dissociation curves of amine terminated PMAA on PHEAA with 100 nm exclusion height. The model showed two modes of dissociation. A slower mode which 2 out of 3 PMAA occupied and a faster mode which 1 out of 3 PMAA occupied.

A	κ_1 (min^{-1})	κ_2 (min^{-1})
0.7416	0.1061	1.6840

4.3.2 Analysis of Trapping

The substrates with nanowells mentioned at the beginning of this section were used to measure and analyse the ability of PMAA to move fluorescent cargo through a PHEAA brush, into a small enclosure and trap it on the other side. The substrates were inserted in a flow cell and mounted on the microscope. Injections of buffer and Fluorescein-modified PMAA were made using a syringe pump at a flow rate of 150 µl/min. Fluorescein-modified PMAA was injected at both pH 7.5 and pH 4.0 and the changes in fluorescence from the nanowell side and the gold side of the substrate were compared when analysing the amount of trapped fluorescent cargo.

Injections at pH 4.0 were done over four stages, as shown in Figure 4.9. Images were taken with 10 ms, 50 ms, and 250 ms exposure time after each stage. A solution of 0.5 mg/ml Fluorescein-modified PMAA in PBS with PMAA in 2:1 molar excess was used for injections at both pH 4.0 and pH 7.5. Buffer was injected at pH 7.5 and reference images were taken. Fluorescein-modified PMAA was then injected

at pH 4.0. The PMAA inserted itself into the PHEAA brush and diffused into the nanowells. Buffer was then injected at pH 4.0 to remove Fluorescein-modified PMAA from the bulk. Buffer was lastly injected at pH 7.5 to remove Fluorescein-modified PMAA from the PHEAA brush, which only left fluorescent material inside the nanowells. Comparisons made before and after injection of PMAA were all done at pH 7.5. This because of the lower fluorescence quantum yield of Fluorescein at pH below 6, as was mentioned earlier.

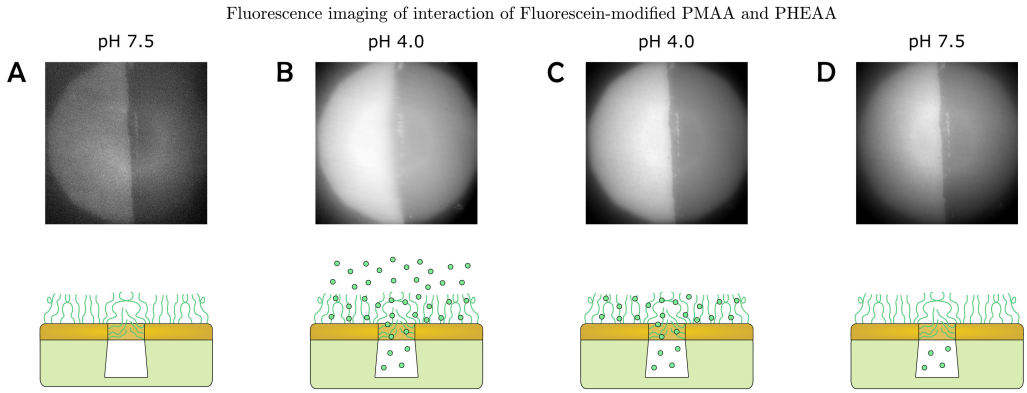

Figure 4.9: The stages of the fluorescence trapping measurements. In all images, the right side consists of gold, and the left side consists of nanowells. (A) Buffer was injected at pH 7.5 as a background reference. (B) Fluorescein-modified PMAA was injected. It inserted itself into the PHEAA brush and diffused into the nanowells. (C) Buffer was injected at pH 4.0 and washed away PMAA in the bulk liquid and loosely bound within the PHEAA brush. (D) Buffer was injected at pH 7.5 and washed away PMAA still inside the PHEAA brush.

To show that the transport was selective with regards to the protonation state of PMAA, which was controlled by changing the pH, Fluorescein-modified PMAA was injected at pH 7.5 and pH 4.0 and the nanowell-gold contrast before and after the injections were compared. A solution of 0.1 mg/ml Fluorescein-modified PMAA with PMAA in 2:1 molar excess was used for injections at both pH 4.0 and pH 7.5. As this was a reference to ensure that fluorescence originating from the nanowells was from Fluorescein attached to PMAA and not Fluorescein that had failed to undergo NHS-amine coupling, Fluorescein was used at both pH 4.0 and pH 7.5 despite the lower quantum yield of Fluorescein at the low pH. This was compensated for by using a longer exposure time of 200 ms and EM gain on the microscope. A comparison of injections at pH 4.0 and pH 7.5 is shown in Figure 4.10.

It was observed in Figure 4.10A that an injection of Fluorescein-modified PMAA at pH 7.5 did not lead to a discernible increase in contrast between the gold and the nanowells. This means that the PHEAA brushes behaved as a strong entropic barrier against PMAA in its charged state and thus disallowed access to the nanowells. In contrast, the injection at pH 4.0 led to a large shift in the contrast compared to the starting value. This suggests that the PMAA was able to insert itself into the barrier and into the nanowells. Additionally, the measured fluorescence during

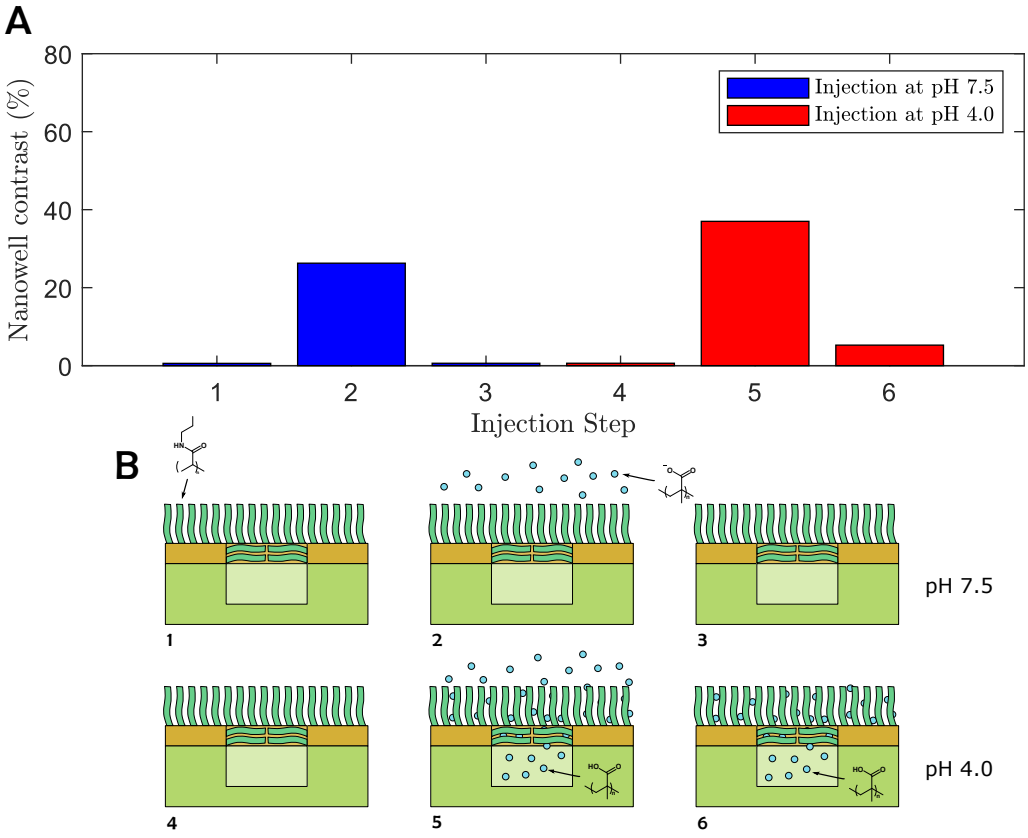

Figure 4.10: Measurements that demonstrate the selective transport and trapping capabilities of a PHEAA brush. (A) Measurements were conducted at pH 7.5 (blue) and at pH 4.0 (red). No discernible increase in contrast was observed for the injection at pH 7.5, while a significant increase in contrast was observed for the injection at pH 4.0. (B) Illustration of the selective trapping.

injection at pH 4.0 was higher than the one measured during injection at pH 7.5. This despite the lower quantum yield of Fluorescein at low pH. It was hypothesised that this was because of the high concentration of fluorophores in solution during the injection reduced the accuracy of the measurement by potentially partially saturating the camera. When comparing the shift in fluorescence intensity before and after injection, the values with no fluorophores in the bulk should be used.

Substrates with 120 nm diameter nanowells were used in Figure 4.10. As was discussed earlier, these substrates have the same surface area of gold on both the nanowell side and the plain gold side of the substrate. Therefore, an increase in fluorescence on the nanowell side of the substrate should originate from fluorophores located inside the nanowells. The contrasts from Figure 4.10A are given in Table 4.6.

Table 4.6: Measured contrast between the nanowells and gold in the experiment shown in Figure 4.7. No discernible increase in contrast was observed over stages 1 through 3, which was the injection at pH 7.5. A significant increase in fluorescence both during the injection in stage 5 and 6 was observed at pH 4.0.

Step 1	Step 2	Step 3	Step 4	Step 5	Step 6
1	26	1	1	37	5

4.3.3 Analysis of the Brush Heights Impact on Trapping

Having showed that it was possible to move and trap cargo inside nanowells using PMAA as a shuttle the impact the exclusion height of the PHEAA brush had on the ability of PMAA to move fluorescent cargo was investigated. It was hypothesised that the exclusion height of the brush had to cover the radius of the nanowell to trap fluorescent cargo on the other side. If true, covering the substrate with a layer of PHEAA brush shorter than the radius of the nanowell would not give a change in contrast before and after injection. It was also hypothesised that a brush with an exclusion height much larger than the radius of the nanowell would increase the resistance the PMAA would face when diffusing into the nanowell. If true, a greater exclusion height would lead to less trapping.

To show that the brush height affected the amount of trapped fluorescent cargo, Fluorescein-modified PMAA was injected at pH 4.0 and the intensity before and after injection was compared at pH 7.5. A solution of 0.5 mg/ml Fluorescein-modified PMAA with PMAA in 2:1 molar excess was used for injections. A higher concentration than in the previous experiment was chosen to increase the degree of saturation and amount of fluorescent cargo that would be trapped inside the nanowells.

Measurements were performed on 120 nm diameter nanowells and 200 nm diameter nanowells with a PHEAA brush that was grafted to various heights. As a reference for substrate where the PHEAA brush did not close the nanowells a 50 nm brush was grown on a substrate with 120 nm diameter nanowells. As this was lower than the radius of the nanowell, the brushes were expected not to prevent the fluorophores to leave the nanowell upon rinsing out the flowcell, similar to what was observed by Emilsson et al. [29] where thiol-grafted PEG did not prevent access through a nanopore when it did not fully extend over the nanopore. Also, PMAA readily adsorbs onto plain gold, which has been shown by J. Andersson et al. [37]. Grafting a short PHEAA brush onto the substrate would prevent adsorption of PMAA at pH 7.5. Figure 4.11 shows two measurements comparing trapping of Fluorescein-modified PMAA on a substrate with 120 nm nanowells with a 50 nm PHEAA brush and a substrate with 200 nm nanowells with a 100 nm PHEAA brush.

When the PHEAA brush did not fully close the nanowell, as was the case in Figure 4.11A, there was no discernible change in contrast after injection of Fluorescein-modified PMAA. This was made more apparent when comparing injection steps 2 and 3 between Figures 4.11A and 4.11B. As illustrated in Figure 4.11A, during

injection at pH 4.0 the PHEAA brush was saturated with PMAA and the nanowells were filled with Fluorescein-modified PMAA. It was the fluorescent cargo inside the nanowells that led to the increase in contrast during injection step 2. After rinsing with buffer at pH 4.0 the contrast returned to unity when the nanowells were rinsed.

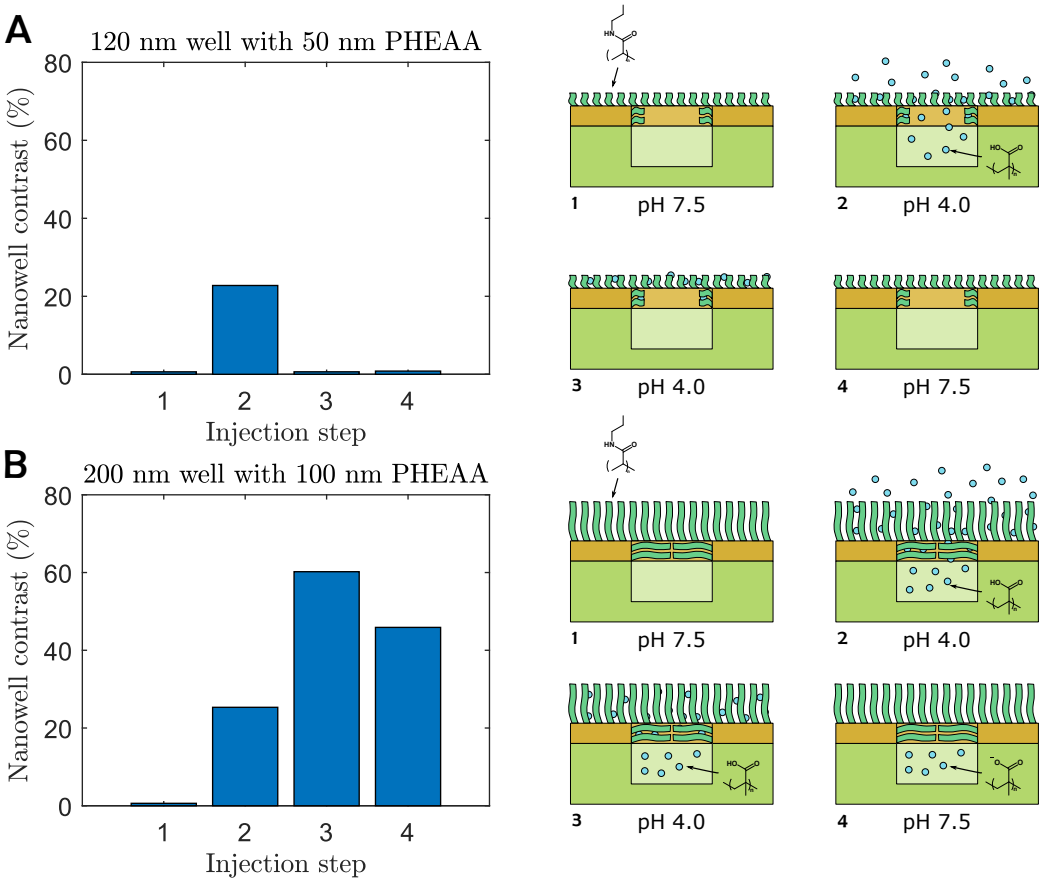

Figure 4.11: Measurements that detail the relation between the PHEAA height and the amount of trapped fluorescent cargo. (A) When the height of the PHEAA brush was insufficient to fully close the nanowell, no discernible change in contrast over the nanowells was observed after the injection. This indicated that the cargo had diffused into the buffer. (B) When the PHEAA brush fully closed the nanowell, a significant increase in the contrast over the nanowells was observed. This indicated that fluorescent cargo was trapped inside the nanowells.

However, while the contrast returned to unity after rinsing, an increase in fluorescence relative injection step 1 was observed. This suggested that the grafting density on the gold inside the opening of the nanowells was equal to, or close to, that on the plain gold surface. As was discussed earlier, when the substrates have 120 nm diameter nanowells they have the same surface area of gold on both the nanowell side and the plain gold side of the substrate. If there is an equal amount of fluorescence originating from both sides of the substrate, the amount of grafted PHEAA onto which Fluorescein-modified PMAA had been inserted must also be in equal amount.

When the PHEAA brush fully closed the nanowell, as was the case in Figure 4.11B where the exclusion height of PHEAA was more than the radius of the nanowell, a substantial increase in contrast was observed after injection of Fluorescein-modified PMAA. The contrast was increased further after rinsing with PBS at pH 7.5 and removing the PMAA that was inserted into the PHEAA brush. Compared to the reference in Figure 4.11A the increased contrast at injection step 3 had to originate from Fluorescein-modified PMAA inside the nanowells. An increase in the fluorescence over the nanowells was observed after rinsing with buffer at pH 4.0, despite the reduced quantum yield of Fluorescein at the low pH. Measured contrasts during the injections are shown in Table 4.7.

Table 4.7: Measured contrasts for substrates with different nanowell diameter and PHEAA brush heights at each step of the injection. A noticeable similarity between different substrates was observed during injection step 2. Additionally, it was noted that the 200 nm diameter nanowells showed a higher contrast than the 120 nm diameter with identical brush heights in the final injection step.

		Nanowell contrast (%)			
Nanowell (nm)	Brush (nm)	Step 1	Step 2	Step 3	Step 4
120	50	1	23	1	1
120	80	1	35	40	13
120	100	1	24	46	6
200	100	1	25	60	46
200	180	0	23		23

When the measurements shown in Table 4.7 were compared, it was observed that the contrast in step 4 was increased for each height of PHEAA brush other than the one that was shorter than the radius of the nanowell. This coincides with the hypothesis that the brush height limits the ability of trapping fluorescent cargo inside the nanowells. Additionally, it was observed that the thicker the PHEAA brush was relative to the diameter of the nanowell, the less the contrast would increase. This is shown during step 4 in Table 4.7. This would suggest that as the PHEAA brush continued to grow after closing the nanowell, it began to extend further into solution and created a denser barrier. This would create more anchoring points and could prevent PMAA from diffusing into the nanowell.

On an intermolecular level, a higher monomer density at the opening of the nanowell would shift the ratio of the modes of interaction suggested in the previous section. A thicker brush would offer a larger volume in which Fluorescein-modified PMAA could be inserted, as is shown during step 3 in Table 4.7. Note, step 3 of the 200 nm diameter nanowell with a 180 nm PHEAA brush is missing due to an experimental error. If the PMAA was bound too strong deeper inside the brush it might not have been able to diffuse as easily into the nanowells. All injections were performed over

30 minutes, which had been confirmed by both SPR and QCM-D measurements to be more than sufficient time to saturate PHEAA brushes of similar heights.

Another explanation could be that the PHEAA brushes had grown down inside and started to fill up the nanowell. This would reduce the total volume in the nanowell in which PMAA could be trapped. However, as was shown by P. Polanowski et al. the available number of monomers inside the confined volume of a nanowell would lead to a reduced rate of polymerisation [94], but the limited volume of the 30 nm thick nanopore would make this reduction unlikely. Furthermore, simulations by Peleg et al. [95] shows that polymers grown inside nanopores become restricted once the radius of the pore is met, and will as a result extended into solution at either side of the openings. Due to the more restricted geometry of the nanowell, compared to the opening out into the bulk, it would be more likely for the brush to extend out into solution.

The limitations the PHEAA brush places on the ability of PMAA to move molecular cargo is a factor that needs to be investigated further. As was shown in Figure 4.11, there exist a critical exclusion height of PHEAA necessary to prevent Fluorescein-modified PMAA from leaving the nanowell once the affinity for PHEAA is changed. This would also suggest that when PHEAA was below this critical exclusion height that cargo would have been able to freely diffuse in and out of the nanopore without the aid of PMAA. This was similar to what was observed by G. Emilsson et al. [29]. When the PHEAA brush increases in height it was observed in Table 4.7 that the access was prevented for PMAA, reducing the diffusion.

When transporting material through nanopores, which are identical to the nanowells in all ways except it fully pierces the substrate [81], this is important to consider. It suggests that there exists an interval of PHEAA brush heights allowed access for PMAA while still preventing access for other macromolecules, and at high brush heights PHEAA prevented access for everything.

4.4 Solid State Nanopore Transport

As was observed in the previous section it was possible to attach NHS-modified fluorescent cargo to amine terminated PMAA, move the shuttle-cargo complex through a PHEAA brush and into a nanowell, and then trap it on the other side. Substrates with 80 nm diameter nanopores in 50 nm thick 140x140 μm^2 silicon nitride membranes were used to verify that the same principle can be used to move fluorescent cargo through a nanopore covered with a PHEAA brush. PHEAA was attached to a 30 nm gold film deposited on one side of the membrane. Nanopores were fabricated using electron beam lithography, as described by B. Malekian et al. [78].

Sensors were coated with PHEAA synthesised to a dry height of 31.2 nm (exclusion height 126.7 nm, swelling ratio 4.1). This ensured that all nanopores were covered and sufficiently prevented any macromolecules from moving through the barrier. A solution of 0.25 mg/ml Cyanine3-modified PMAA in PBS with PMAA in 4:1 molar

excess was used for injections at pH 4.0. A solution of 0.50 mg/ml Fluorescein-modified PMAA in PBS with PMAA in 2:1 molar excess was used for injections at pH 7.5. Two different fluorescent molecules were used because of the lower quantum yield of Fluorescein at pH below 6, as is shown in Figure B.7. Sulfo-Cyanine3 is insensitive to pH between 3 and 10 and was therefore used for measurements at pH 4.0 [96]. All injections of fluorescent cargo were done at a flow rate of 150 µl/min.

Transport was measured using a water immersion objective and a 50 µl droplet of PBS buffer was placed on top of the gold side. PMAA that was able to move through the PHEAA brush would end up inside the water droplet and could be detected by the fluorescent camera. An illustrated example of the experimental setup is shown in Figure 4.12. Transport was measured at both pH 4.0 and pH 7.5. Fluorescence intensity at the membrane, from the fluorophores on the other side, was compared to the fluorescence intensity 40 µm away from the membrane edge.

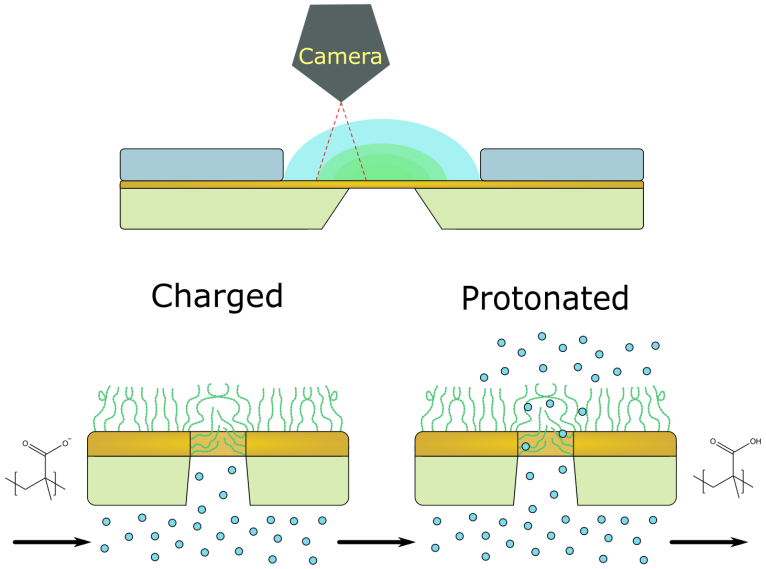

Figure 4.12: An Andor iXon Ultra 888 EMCCD camera was situated over the sensor so that it covered half of the membrane and part of the gold side. Images were taken of fluorescence coming through the membrane and coming from the fluorescent cargo that had moved through the membrane. At pH 7.5 the membrane was expected to be closed since the PHEAA brushes repels the PMAA, while at pH 4.0 the membrane was expected to be open and allow access for the PMAA.

4.4.1 Transport Measurements

Transport was measured at pH 7.5 and pH 4.0 and the change in contrast was compared for the images taken after the injection was completed. Figure 4.13 shows reference images taken before and after injection.

It was observed when looking at the images before and after injection in Figure 4.13 that only the injection at pH 4.0 led to an increase in fluorescence on the gold

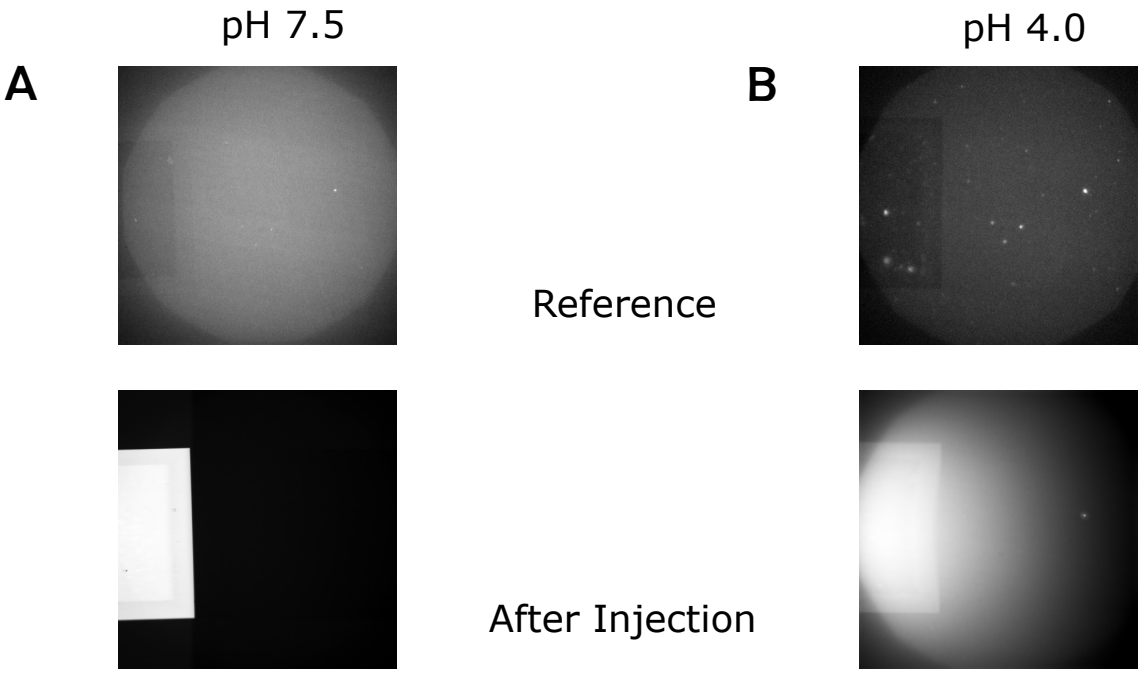

Figure 4.13: Comparative images before and after injection at pH 7.5 and pH 4.0. Images were taken of fluorescence coming through the membrane and coming from the fluorescent cargo that had moved through the pore. (A) At pH 7.5 the PHEAA brushes blocked access for PMAA and a sharp contrast between the membrane and the gold was observed. (B) At pH 4.0 the PHEAA brushes allowed access for PMAA, and fluorescence was observed on the gold side after injection.

side of the substrate. Figure 4.13A shows an injection at pH 7.5. At pH 7.5, an increase in fluorescence was only observed through the membrane. No increase on the gold side was observed. This meant that the PHEAA brush successfully blocked the fluorescent cargo at pH 7.5 and did not allow it to access the other side of the membrane.

The sharp contrast that was observed along the edge in Figure 4.13A showed that all fluorescence originated from the other side of the membrane at pH 7.5. Meanwhile, the saturated contrast that was observed to stretch out from the edge in Figure 4.13B showed that fluorescent cargo had migrated through the membrane and onto the gold side. Since all cargo was attached to PMAA shuttles, the observation of fluorescence only at pH 4.0, and not pH 7.5, concluded that the diffusion through the membrane was directed by the PMAA-PHEAA interaction. Additionally, it proved that the shuttle-cargo mechanism worked for molecular cargo and that the access and affinity through the membrane was controlled by PMAA's protonation state.

4.4.2 Analysis of Continuous Diffusion

Averaged fluorescence intensities from 10x10 μm^2 squares were measured at 40 µm, 80 µm and 120 µm away from the edge of the membrane. As was observed in Figure 4.13A, no transport of fluorescent cargo occurred at pH 7.5. Because of this only the

averaged fluorescence intensities positioned 40 µm from the edge of the membrane was considered for pH 7.5. All measured intensities were normalised based on the maximum intensity that was recorded from the membrane during the span of the experiment and are shown in Figures 4.14A and 4.14C. Additionally, the change in intensity is visualised as a change in contrast between the gold away from the edge of the membrane and the center of the membrane, as shown in Figure 4.14B. This contrast was calculated by comparing the intensity over the gold to the intensity over the membrane at each measuring point, instead of the maximum intensity over the membrane overall.

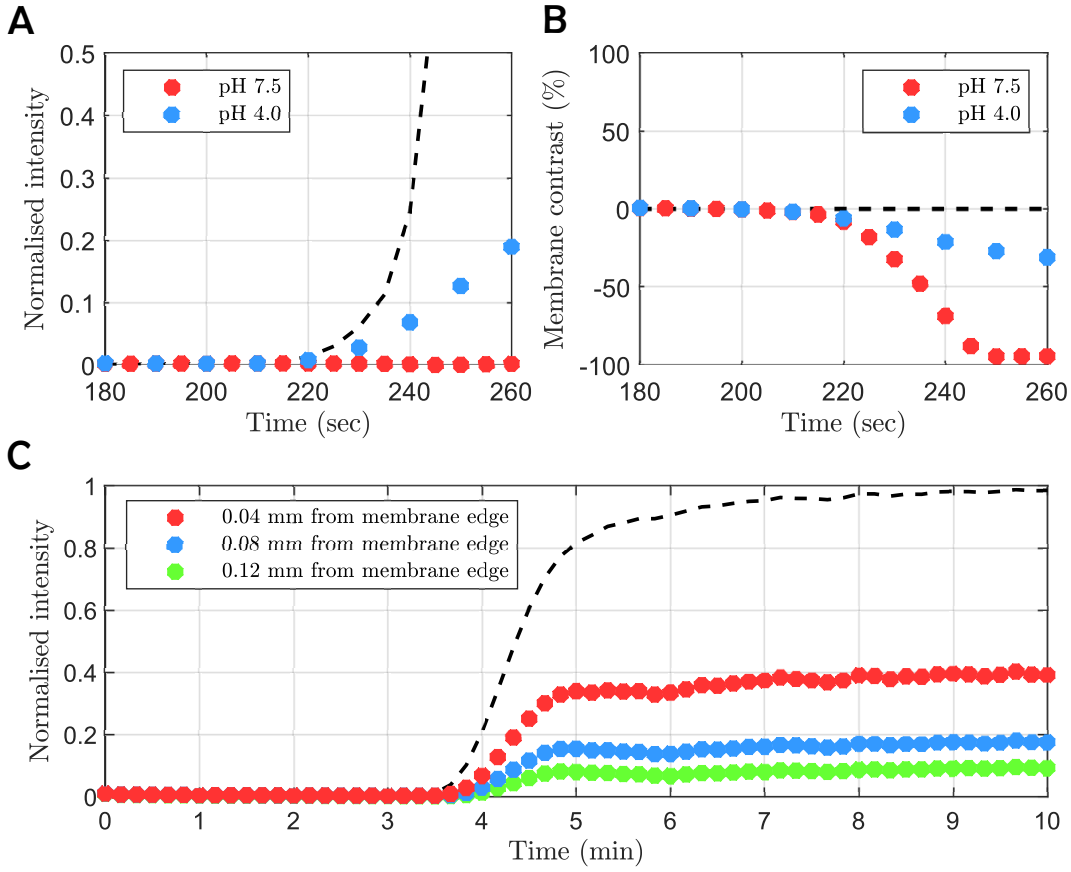

Figure 4.14: Measured averaged fluorescence intensity at pH 4.0 and pH 7.5 relative to the membrane maximum and the contrast between the gold side and the membrane at pH 4.0 and pH 7.5. Normalised average fluorescence intensity at pH 4.0 was shifted to overlap with the initial value at pH 7.5. Normalised fluorescence intensity over the membrane is shown as a black dashed line. (A) Measured fluorescence intensity on the gold side, 0.04 mm from the edge of the membrane. No increase in fluorescence intensity was observed at pH 7.5 (red). A correlated increase to that of the membrane intensity was observed at pH 4.0 (blue). (B) Measured contrast in fluorescence intensity between the gold side and the membrane. (C) Measured fluorescence intensity in a 10x10 μm^2 square located 0.04 mm (red), 0.08 mm (blue), and 0.12 mm (green) away from the membrane edge. Relative increase in fluorescence intensity was diminished farther away from membrane edge.

Looking at the change in fluorescence in Figure 4.14A, it was confirmed that the fluorescent cargo was only able to move through the membrane at pH 4.0. No change in fluorescence was observed when fluorescent cargo was injected at pH 7.5, whereas at pH 4.0 the fluorescence was observed to increased proportional to the fluorescence coming through the membrane. Further comparing the contrast between the membrane and the gold in Figure 4.14B showed a clear difference between transport at pH 4.0 and no transport at pH 7.5.

When comparing the fluorescence at 40 µm, 80 µm and 120 µm away from the edge of the membrane in Figure 4.14C, it was observed that the fluorescence increase was diminished the farther away from membrane edge the measurement was taken. 10 minutes after injection the fluorescence had reached 58% of the intensity that was observed at the membrane 40 µm from the edge. Similarly, it had reached 43% of the intensity 80 µm from the edge and 38% of the intensity 120 µm from the edge. This suggested that the access and ability of PMAA to diffuse freely inside the droplet was limited by the PHEAA brush. If fluorescent cargo were able to freely diffuse through the membrane it would quickly spread out and remove all contrast in the volume near the membrane. This did not occur even after 30 minutes.

It was observed in Figure 4.14C that the fluorescence measured at 40 µm, 80 µm and 120 µm away from the edge of the membrane did not increase identically. The region just before and just after the injection of fluorescent cargo was enhanced and is shown in Figure 4.15. An increase in fluorescence at the membrane was observed after 200 seconds. A noticeable increase in fluorescence 40 µm away from the edge of the membrane was observed 20 seconds after this, at 220 seconds. This was slower than the rate at which images were taken. Similarly, an increase was observed 80 µm away after 30 seconds, and 120 µm away after 40 seconds.

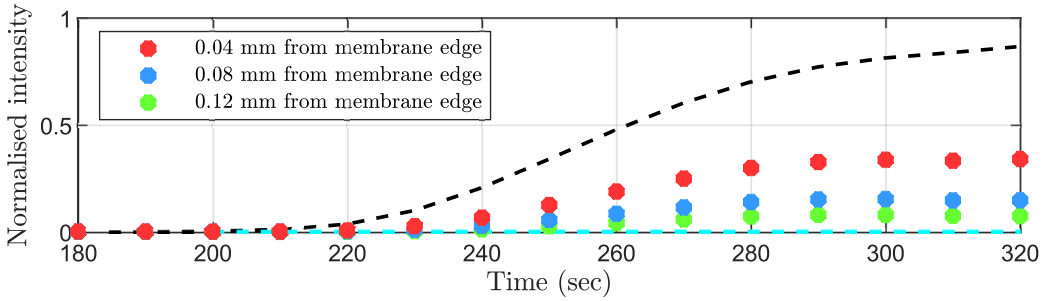

Figure 4.15: Measured fluorescence intensity in a 10x10 µm^2 square located 0.04 mm (red), 0.08 mm (blue), and 0.12 mm (green) away from the membrane edge. Relative increase in fluorescence intensity was diminished farther away from membrane edge. The observed increase on the membrane is shown as a black dotted line. The fluorescence on the gold side before injection is shown as a dashed cyan line.

PMAA has a characteristic diffusion constant of approximately 100 µm^2/s. This value was estimated using the Stokes-Einstein equation [97, 98]. Based on Brownian motion it should take the shuttle-cargo complex approximately 3 seconds to diffuse 40 µm, 10 seconds to diffuse 80 µm, and 24 seconds to diffuse 120 µm. While the

initial increase 40 µm away from the edge of the membrane was observed to be much slower than this, the subsequent distances followed diffusion on the same time scale. However, it was deemed possible that the interactions between PMAA and PHEAA hindered the diffusion and lowered to characteristic diffusion constant of PMAA as it was migrating through PHEAA.

After the fluorescent cargo reached the membrane, which was shown as an increase in the fluorescence at the membrane in Figure 4.15, the fluorescence increased on the gold side for a few minutes until a sudden decrease in the growth rate of fluorescence was observed. This occurred approximately five minutes after the injection started. After this point the PHEAA brushes had been saturated with PMAA, as was observed to occur after only a few minutes in SPR in Figure B.5. Once saturated, it was believed that the rate with which PMAA was able to move through the nanopore was diminished. This would explain the change in slope that was observed in Figure 4.15. When the nanopore is saturated, i.e., clogged, by PMAA, the polymer could only move through the membrane at the same rate as it dissociated from the PHEAA on the other side.

5

Conclusions and Outlook

In this work a method of replicating the nuclear transport of biomolecules facilitated by the nuclear pore complex was developed, studied, and tested. Taking inspiration from the transport of biomolecules through the nuclear envelope of eukaryotic cells via the nuclear pore complex, an artificial biological shuttle-cargo mechanism was envisioned using poly(methacrylic acid) and poly(N-(2-hydroxyethyl)acrylamide) as a shuttle and barrier for selective transport of macromolecules through nanopores.

This work has investigated the functionalisation of gold-coated surfaces and membrane with PHEAA polymer brushes for use as a selective barrier. The barrier of PHEAA was shown to have antifouling properties against proteins and other macromolecules, while allowing PMAA to reversibly insert itself. This interaction was also proven to be controllable by changing the protonation state of the polymer shuttle. In a protonated state PMAA was shown to interact with PHEAA and form a two-state equilibrium where it could bind to PHEAA via either of two independent adsorption processes. In a charged state it was shown to be repelled by PHEAA and be released from PHEAA if already inserted into the brush.

In order to further optimise the interaction between PMAA and PHEAA the strongly bound fraction after injection of PMAA should be reduced. This could be accomplished by reducing the hydrogen bonding possibilities of PMAA and PHEAA. Further investigation into the pH dependence of the interaction between PMAA and PHEAA could lead to the discovery of a certain degree of protonation of PMAA where the fraction of charged and protonated sub-units on PMAA are just enough to both offer enough interaction for PMAA to insert itself into PHEAA while preventing it from getting stuck in the brush. A similar effect could be achieved by changing the composition of the PMAA backbone and introducing comonomer subunits that will not interact with PHEAA. Water soluble random co-polymers of methacrylic acid have successfully been synthesised [99], and modifying the shuttle with new comonomers could decrease the interactions with PHEAA and increase the reversibility.

Using Fluorescent-modified PMAA, the ability of PMAA to diffuse through a barrier of PHEAA and move fluorescent cargo through a nanopore was investigated. PMAA was shown to actively transport fluorescent cargo into nanosized wells in a

protonated state, while being rejected by the barrier in a charged state. Additionally, it was shown that shifting the protonation state of PMAA once it had moved the fluorescent cargo into the nanowell would change its affinity for the PHEAA barrier and trap it on the other side. This was also shown to be true for continuous transport through solid state nanopores, where PMAA diffused through a PHEAA barrier in its protonated state while being rejected by it in its charged state.

In order to achieve long-term and continuous shuttle-cargo transport the tendency of PMAA to clog the pore and diminish the rate of transport should be reduced. This is likely related to the strong degree of hydrogen bonding between PMAA and PHEAA that resulted in the very slow dissociation after injections in SPR. However, further investigation into the effect of the exclusion height of the barrier once attached to a nanopore could lead to the discovery of a critical exclusion height where the degree of saturation of the lightly bound fraction is minimised. Emilsson et al. have shown that a certain exclusion height exists for PEG where it just begins to reject macromolecules from nanopores [29], and it is likely that a similar critical exclusion height exists for PHEAA. Another solution could be to increase the degree of hydration of the diffusion barrier. This could reduce the number of hydrogen bonding sites between PMAA and PHEAA, and thus reduce the transport limitation. Schüwer et al. have shown that immobilisation of inactive initiators on the surface reduce the effective grafting density, which in turn increases the water content of the polymer brush [100].

To the best of my knowledge, this work is the first study to demonstrate the use of PMAA and PHEAA as an artificial shuttle-and-barrier pair that mimics the selective transport barrier of the nuclear pore complex. This work can be further extended by conjugation of macromolecular cargo, such as proteins or DNA, for single-molecule transport and capture. Other shuttle-and-barrier pairs that interact with the same hydrogen bond possibilities are likely to exist and could further extend the potential and flexibility of this selective transport method.

Bibliography

[1] Martin W Goldberg. "Nuclear pore complex tethers to the cytoskeleton". In: *Seminars in cell & developmental biology*. Vol. 68. Elsevier. 2017, pp. 52–58.

[2] Bastiaan C Buddingh' and Jan CM van Hest. "Artificial cells: synthetic compartments with life-like functionality and adaptivity". In: *Accounts of chemical research* 50.4 (2017), pp. 769–777.

[3] Chen Wang, Junzhu Yang, and Yuan Lu. "Modularize and unite: toward creating a functional artificial cell". In: *Frontiers in Molecular Biosciences* 8 (2021).

[4] Clare M O'Connor, Jill U Adams, and Jennifer Fairman. "Essentials of cell biology". In: *Cambridge, MA: NPG Education* 1 (2010), p. 54.

[5] Susan R Wente and Michael P Rout. "The nuclear pore complex and nuclear transport". In: *Cold Spring Harbor perspectives in biology* 2.10 (2010), a000562.

[6] Martin Beck and Ed Hurt. "The nuclear pore complex: understanding its function through structural insight". In: *Nature reviews Molecular cell biology* 18.2 (2017), pp. 73–89.

[7] George J Stanley, Ariberto Fassati, and Bart W Hoogenboom. "Biomechanics of the transport barrier in the nuclear pore complex". In: *Seminars in cell & developmental biology*. Vol. 68. Elsevier. 2017, pp. 42–51.

[8] Tijana Jovanovic-Talisman and Anton Zilman. "Protein transport by the nuclear pore complex: simple biophysics of a complex biomachine". In: *Biophysical journal* 113.1 (2017), pp. 6–14.

[9] Bhanu P Jena. "Nuclear pore: a bidirectional transport machinery". In: *Cellular Nanomachines*. Springer, 2020, pp. 71–77.

[10] Michael P Rout et al. "The yeast nuclear pore complex: composition, architecture, and transport mechanism". In: *The Journal of cell biology* 148.4 (2000), pp. 635–652.

[11] Mary Christie et al. "Structural biology and regulation of protein import into the nucleus". In: *Journal of molecular biology* 428.10 (2016), pp. 2060–2090.

[12] Ruiwen Wang and Michael G Brattain. "The maximal size of protein to diffuse through the nuclear pore is larger than 60 kDa". In: *FEBS letters* 581.17 (2007), pp. 3164–3170.

[13] Petra Popken et al. "Size-dependent leak of soluble and membrane proteins through the yeast nuclear pore complex". In: *Molecular biology of the cell* 26.7 (2015), pp. 1386–1394.

[14] Steven I Dworetzky and Carl M Feldherr. “Translocation of RNA-coated gold particles through the nuclear pores of oocytes.” In: *The Journal of cell biology* 106.3 (1988), pp. 575–584.

[15] Nelly Panté and Michael Kann. “Nuclear pore complex is able to transport macromolecules with diameters of 39 nm”. In: *Molecular biology of the cell* 13.2 (2002).

[16] Junona Moroianu. “Nuclear import and export pathways”. In: *Journal of cellular biochemistry* 75.S32 (1999), pp. 76–83.

[17] Daniel P Denning et al. “Disorder in the nuclear pore complex: the FG repeat regions of nucleoporins are natively unfolded”. In: *Proceedings of the National Academy of Sciences* 100.5 (2003), pp. 2450–2455.

[18] Michael Rexach and Günter Blobel. “Protein import into nuclei: association and dissociation reactions involving transport substrate, transport factors, and nucleoporins”. In: *Cell* 83.5 (1995), pp. 683–692.

[19] Katharina Ribbeck and Dirk Görlich. “Kinetic analysis of translocation through nuclear pore complexes”. In: *The EMBO journal* 20.6 (2001), pp. 1320–1330.

[20] Joan Pulupa et al. “Conformation of the nuclear pore in living cells is modulated by transport state”. In: *Elife* 9 (2020), e60654.

[21] Brian E Hall, Dafna Bar-Sagi, and Nicolas Nassar. “The structural basis for the transition from Ras-GTP to Ras-GDP”. In: *Proceedings of the National Academy of Sciences* 99.19 (2002), pp. 12138–12142.

[22] Pieter FW Stouten et al. “How does the switch II region of G-domains work?” In: *FEBS letters* 320.1 (1993), pp. 1–6.

[23] Juane Lu et al. “Types of nuclear localization signals and mechanisms of protein import into the nucleus”. In: *Cell communication and signaling* 19.1 (2021), pp. 1–10.

[24] Yaron Caspi et al. “Synthetic mimic of selective transport through the nuclear pore complex”. In: *Nano letters* 8.11 (2008), pp. 3728–3734.

[25] Tijana Jovanovic-Talisman et al. “Artificial nanopores that mimic the transport selectivity of the nuclear pore complex”. In: *Nature* 457.7232 (2009), pp. 1023–1027.

[26] Stefan Kowalczyk et al. “Single-molecule transport across an individual biomimetic nuclear pore complex”. In: *Nature nanotechnology* 6.7 (2011), pp. 433–438.

[27] Zdeněk Farka et al. “Advances in Optical Single-Molecule Detection: En Route to Supersensitive Bioaffinity Assays”. In: *Angewandte Chemie International Edition* 59.27 (2020), pp. 10746–10773.

[28] Wei-Liang Chen et al. “50th anniversary perspective: Polymer brushes: Novel surfaces for future materials”. In: *Macromolecules* 50.11 (2017), pp. 4089–4113.

[29] Gustav Emilsson et al. “Polymer brushes in solid-state nanopores form an impenetrable entropic barrier for proteins”. In: *Nanoscale* 10.10 (2018), pp. 4663–4669.

[30] Jie Zheng et al. “Molecular simulation study of water interactions with oligo (ethylene glycol)-terminated alkanethiol self-assembled monolayers”. In: *Langmuir* 20.20 (2004), pp. 8931–8938.

[31] Teiji Tsuruta. “On the role of water molecules in the interface between biological systems and polymers”. In: *Journal of Biomaterials Science, Polymer Edition* 21.14 (2010), pp. 1831–1848.

[32] SI Jeon et al. “Protein—surface interactions in the presence of polyethylene oxide: I. Simplified theory”. In: *Journal of colloid and interface science* 142.1 (1991), pp. 149–158.

[33] Shenfu Chen et al. “Surface hydration: Principles and applications toward low-fouling/nonfouling biomaterials”. In: *Polymer* 51.23 (2010), pp. 5283–5293.

[34] Lingyan Li et al. “Protein adsorption on oligo (ethylene glycol)-terminated alkanethiolate self-assembled monolayers: the molecular basis for nonfouling behavior”. In: *The Journal of Physical Chemistry B* 109.7 (2005), pp. 2934–2941.

[35] Chao Zhao and Jie Zheng. “Synthesis and characterization of poly(N-hydroxyethylacrylamide) for long-term antifouling ability”. In: *Biomacromolecules* 12.11 (2011), pp. 4071–4079.

[36] Blythe Fortier-McGill, Violeta Toader, and Linda Reven. “1H solid state NMR study of poly (methacrylic acid) hydrogen-bonded complexes”. In: *Macromolecules* 45.15 (2012), pp. 6015–6026.

[37] John Andersson et al. “Control of polymer brush morphology, rheology, and protein repulsion by hydrogen bond complexation”. In: *Langmuir* 37.16 (2021), pp. 4943–4952.

[38] Tian Zhou et al. “Towards controlled polymer brushes via a self-assembly-assisted-grafting-to approach”. In: *Nature communications* 7.1 (2016), pp. 1–8.

[39] Krzysztof Matyjaszewski and Nicolay V Tsarevsky. “Macromolecular engineering by atom transfer radical polymerization”. In: *Journal of the American Chemical Society* 136.18 (2014), pp. 6513–6533.

[40] Amir Khabibullin et al. “Surface-initiated atom transfer radical polymerization”. In: *Controlled Radical Polymerization at and from Solid Surfaces* (2015), pp. 29–76.

[41] Justin O Zoppe et al. “Surface-initiated controlled radical polymerization: state-of-the-art, opportunities, and challenges in surface and interface engineering with polymer brushes”. In: *Chemical reviews* 117.3 (2017), pp. 1105–1318.

[42] Gustav Ferrand-Drake del Castillo et al. “Enzyme immobilization in polyelectrolyte brushes: High loading and enhanced activity compared to monolayers”. In: *Langmuir* 35.9 (2019), pp. 3479–3489.

[43] Krzysztof Matyjaszewski and Jianhui Xia. “Atom transfer radical polymerization”. In: *Chemical reviews* 101.9 (2001), pp. 2921–2990.

[44] Xiang Gao et al. “Kinetic modeling of surface-initiated atom transfer radical polymerization”. In: *Macromolecular Reaction Engineering* 4.3-4 (2010), pp. 235–250.

[45] Krzystof Matyjaszewski. “1 New catalysts for controlled/living atom transfer radical polymerization (ATRP)”. In: *Studies in Surface Science and Catalysis* 145 (2003), pp. 3–11.

[46] Petr K Sazonov, Galina A Artamkina, and Irina P Beletskaya. “Nucleophilic substitution at the halogen atom (halogenophilic reactions)”. In: *Russian Chemical Reviews* 81.4 (2012), p. 317.

[47] Nicolay V Tsarevsky and Krzysztof Matyjaszewski. ““Green” atom transfer radical polymerization: from process design to preparation of well-defined environmentally friendly polymeric materials”. In: *Chemical reviews* 107.6 (2007), pp. 2270–2299.

[48] Wojciech Jakubowski and Krzysztof Matyjaszewski. “Activators regenerated by electron transfer for atom-transfer radical polymerization of (meth) acrylates and related block copolymers”. In: *Angewandte Chemie International Edition* 45.27 (2006), pp. 4482–4486.

[49] Gustav Ferrand-Drake del Castillo, Gustav Emilsson, and Andreas Dahlin. “Quantitative analysis of thickness and pH actuation of weak polyelectrolyte brushes”. In: *The Journal of Physical Chemistry C* 122.48 (2018), pp. 27516–27527.

[50] Stefan M Paterson et al. “The synthesis of water-soluble PHEMA via ARGET ATRP in protic media”. In: *Journal of Polymer Science Part A: Polymer Chemistry* 48.18 (2010), pp. 4084–4092.

[51] Antonina Simakova et al. “Aqueous arget atrp”. In: *Macromolecules* 45.16 (2012), pp. 6371–6379.

[52] Ke Min, Haifeng Gao, and Krzysztof Matyjaszewski. “Use of ascorbic acid as reducing agent for synthesis of well-defined polymers by ARGET ATRP”. In: *Macromolecules* 40.6 (2007), pp. 1789–1791.

[53] Anjana Dhar, Bishnu P Koiry, and Dhruba J Haloi. “Synthesis of poly (methyl methacrylate) via ARGET ATRP and study of the effect of solvents and temperatures on its polymerization kinetics”. In: *International Journal of Chemical Kinetics* 50.10 (2018), pp. 757–763.

[54] Daewha Hong et al. “Achieving ultralow fouling under ambient conditions via surface-initiated ARGET ATRP of carboxybetaine”. In: *ACS Applied Materials & Interfaces* 9.11 (2017), pp. 9255–9259.

[55] Wonwoo Jeong et al. “Surface-Initiated ARGET ATRP of antifouling zwitterionic brushes using versatile and uniform initiator film”. In: *Langmuir* 35.41 (2019), pp. 13268–13274.

[56] Su Youn Kim et al. “Formation of Various Polymeric Films via Surface-Initiated ARGET ATRP on Silicon Substrates”. In: *Bulletin of the Korean Chemical Society* 42.5 (2021), pp. 761–766.

[57] Gustav Emilsson et al. “Surface plasmon resonance methodology for monitoring polymerization kinetics and morphology changes of brushes—evaluated with poly (N-isopropylacrylamide)”. In: *Applied Surface Science* 396 (2017), pp. 384–392.

[58] Ray Bakhtiar. “Surface plasmon resonance spectroscopy: a versatile technique in a biochemist’s toolbox”. In: *Journal of Chemical Education* 90.2 (2013), pp. 203–209.

[59] Jiří Homola. “Surface plasmon resonance sensors for detection of chemical and biological species”. In: *Chemical reviews* 108.2 (2008), pp. 462–493.

[60] Erik Helmerhorst et al. “Real-time and label-free bio-sensing of molecular interactions by surface plasmon resonance: a laboratory medicine perspective”. In: *The Clinical Biochemist Reviews* 33.4 (2012), p. 161.

[61] Hoang Hiep Nguyen et al. “Surface plasmon resonance: a versatile technique for biosensor applications”. In: *Sensors* 15.5 (2015), pp. 10481–10510.

[62] Yu Liu and Liang Shen. “From Langmuir kinetics to first-and second-order rate equations for adsorption”. In: *Langmuir* 24.20 (2008), pp. 11625–11630.

[63] Rafael L Schoch and Roderick YH Lim. “Non-interacting molecules as innate structural probes in surface plasmon resonance”. In: *Langmuir* 29.12 (2013), pp. 4068–4076.

[64] G Ferrand-Drake Del Castillo et al. “Generic high-capacity protein capture and release by pH control”. In: *Chemical Communications* 56.44 (2020), pp. 5889–5892.

[65] Linda S Jung et al. “Quantitative interpretation of the response of surface plasmon resonance sensors to adsorbed films”. In: *Langmuir* 14.19 (1998), pp. 5636–5648.

[66] Kyle S Johnston et al. “New analytical technique for characterization of thin films using surface plasmon resonance”. In: *Materials chemistry and physics* 42.4 (1995), pp. 242–246.

[67] Justas Svirelis et al. “Accurate Correction of the “Bulk Response” in Surface Plasmon Resonance Sensing Provides New Insights on Interactions Involving Lysozyme and Poly (ethylene glycol)”. In: *ACS sensors* 7.4 (2022), pp. 1175–1182.

[68] Diethelm Johannsmann. “The quartz crystal microbalance in soft matter research”. In: *Soft and Biological Matter* (2015), pp. 191–204.

[69] Alexandra D Easley et al. “A practical guide to quartz crystal microbalance with dissipation monitoring of thin polymer films”. In: *Journal of Polymer Science* 60.7 (2022), pp. 1090–1107.

[70] Matthew C Dixon. “Quartz crystal microbalance with dissipation monitoring: enabling real-time characterization of biological materials and their interactions”. In: *Journal of biomolecular techniques: JBT* 19.3 (2008), p. 151.

[71] Michael Murat and Gary S Grest. “Structure of a grafted polymer brush: a molecular dynamics simulation”. In: *Macromolecules* 22.10 (1989), pp. 4054–4059.

[72] Bocheng Zhu and Steve Edmondson. *Applying ARGET ATRP to the Growth of Polymer Brush Thin Films by Surface-initiated Polymerization*. Jan. 2022. URL: `https://www.sigmaaldrich.com/SE/en/technical-documents/technical-article/materials-science-and-engineering/polymer-synthesis/applying-arget-atrp-to-the-growth-of-polymer-brush-thin-films`.

[73] W Lukosz. “Principles and sensitivities of integrated optical and surface plasmon sensors for direct affinity sensing and immunosensing”. In: *Biosensors and Bioelectronics* 6.3 (1991), pp. 215–225.

[74] Dmitry I Yakubovsky et al. “Optical constants and structural properties of thin gold films”. In: *Optics express* 25.21 (2017), pp. 25574–25587.

[75] Deborah LM Rupert et al. “Dual-wavelength surface plasmon resonance for determining the size and concentration of sub-populations of extracellular vesicles”. In: *Analytical chemistry* 88.20 (2016), pp. 9980–9988.

[76] Greg T Hermanson. *Bioconjugate techniques*. Academic press, 2013.

[77] Bita Malekian et al. “Fabrication and characterization of plasmonic nanopores with cavities in the solid support”. In: *Sensors* 17.6 (2017), p. 1444.

[78] Bita Malekian et al. “Optical properties of plasmonic nanopore arrays prepared by electron beam and colloidal lithography”. In: *Nanoscale Advances* 1.11 (2019), pp. 4282–4289.

[79] Irving Langmuir. “The adsorption of gases on plane surfaces of glass, mica and platinum.” In: *Journal of the American Chemical society* 40.9 (1918), pp. 1361–1403.

[80] A Halperin and M Kroger. “Ternary protein adsorption onto brushes: strong versus weak”. In: *Langmuir* 25.19 (2009), pp. 11621–11634.

[81] Gustav Emilsson et al. “Gating protein transport in solid state nanopores by single molecule recognition”. In: *ACS central science* 4.8 (2018), pp. 1007–1014.

[82] C Vericat et al. “Self-assembled monolayers of thiols and dithiols on gold: new challenges for a well-known system”. In: *Chemical Society Reviews* 39.5 (2010), pp. 1805–1834.

[83] Chao Zhao et al. “Synthesis and characterization of pH-sensitive poly (N-2-hydroxyethyl acrylamide)–acrylic acid (poly (HEAA/AA)) nanogels with antifouling protection for controlled release”. In: *Soft Matter* 8.30 (2012), pp. 7848–7857.

[84] IR Spectrum Table. “Chart”. In: *Sigma-Aldrich https://www. sigmaaldrich. com/technical-documents/articles/biology/ir-spectrum-table. html* (2019).

[85] Douglas C Montgomery. *Design and Analysis of Experiments*. John Wiley & Sons, 2017.

[86] Yu-Ran Luo and J Alistair Kerr. “Bond dissociation energies”. In: *CRC handbook of chemistry and physics* 89 (2012), p. 89.

[87] Krzysztof Matyjaszewski et al. “Diminishing catalyst concentration in atom transfer radical polymerization with reducing agents”. In: *Proceedings of the National Academy of Sciences* 103.42 (2006), pp. 15309–15314.

[88] Yungwan Kwak, Andrew JD Magenau, and Krzysztof Matyjaszewski. “ARGET ATRP of methyl acrylate with inexpensive ligands and ppm concentrations of catalyst”. In: *Macromolecules* 44.4 (2011), pp. 811–819.

[89] PubChem. *Methacrylic acid*. Jan. 2022. URL: `https://pubchem.ncbi.nlm.nih.gov/compound/Methacrylic-acid`.

[90] Haitao Dong et al. “The Effects of Chemical Substitution and Polymerization on the pKa Values of Sulfonic Acids”. In: *The Journal of Physical Chemistry B* 113.43 (2009), pp. 14094–14101.

[91] Thomas H Haines. “Anionic lipid headgroups as a proton-conducting pathway along the surface of membranes: a hypothesis”. In: *Proceedings of the National Academy of Sciences* 80.1 (1983), pp. 160–164.

[92] Peter Schuck and Huaying Zhao. “The role of mass transport limitation and surface heterogeneity in the biophysical characterization of macromolecular

binding processes by SPR biosensing". In: *Surface plasmon resonance* (2010), pp. 15–54.

[93] Roderick YH Lim, Binlu Huang, and Larisa E Kapinos. "How to operate a nuclear pore complex by Kap-centric control". In: *Nucleus* 6.5 (2015), pp. 366–372.

[94] Piotr Polanowski, Jeremiasz K Jeszka, and Krzysztof Matyjaszewski. "Polymer brushes in pores by ATRP: Monte Carlo simulations". In: *Polymer* 211 (2020), p. 123124.

[95] Orit Peleg et al. "Morphology control of hairy nanopores". In: *ACS nano* 5.6 (2011), pp. 4737–4747.

[96] AAT Bioquest. *Sulfo-Cyanine 3 NHS ester*. 2022. URL: `https://www.aatbio.com/products/sulfo-cyanine-3-nhs-ester` (visited on 06/01/2022).

[97] Ron Milo and Rob Phillips. *Cell biology by the numbers*. Garland Science, 2015.

[98] Albert Einstein. *Investigations on the Theory of the Brownian Movement*. Courier Corporation, 1956.

[99] Milan Marić, Chi Zhang, and Daniel Gromadzki. "Poly (methacrylic acid-ran-2-vinylpyridine) statistical copolymer and derived dual pH-temperature responsive block copolymers by nitroxide-mediated polymerization". In: *Processes* 5.1 (2017), p. 7.

[100] Nicolas Schüwer and Harm-Anton Klok. "Tuning the pH sensitivity of poly (methacrylic acid) brushes". In: *Langmuir* 27.8 (2011), pp. 4789–4796.

[101] EA Slyusareva et al. "Spectral and fluorescent indication of the acid-base properties of biopolymer solutions". In: *Russian Physics Journal* 54.4 (2011), pp. 485–492.

A

Appendix: Derivations

Nanowell Surface Area Change

Equation 3.1 gave an expression for the ratio of relative surface area and its change when a hole is introduced on a thin film. From basic geometry, Equation A.1a equates to the area lost when introducing a hole on a surface and Equation A.1b equates to the area that is gained from the inside of the cylinder that is formed after the hole is introduced. Taking the ratio of these two areas gives Equation A.1c.

$$A_{\text{hole}} = \pi r^2 \tag{A.1a}$$

$$A_{\text{wall}} = 2\pi r h \tag{A.1b}$$

$$\frac{A_{\text{hole}}}{A_{\text{wall}}} = \frac{r}{2h} \tag{A.1c}$$

Two-Mode Dissociation Model

Equation 3.5 gave an expression for the decrease in analyte when it desorbed from a surface. During the dissociative process, no analyte was injected, and any desorbed material was assumed to be removed fast enough from the surface that the bulk concentration could be approximated to be $C_0 = 0$. This simplifies Equations 3.4a and 3.4b in Equations A.2a and A.2b.

$$\frac{d\gamma_1}{dt} = -\kappa_{\text{off},1}\Gamma_1(t) \tag{A.2a}$$

$$\frac{d\gamma_2}{dt} = -\kappa_{\text{off},2}\Gamma_2(t) \tag{A.2b}$$

The new system of differential equations describes the total dissociation of analytes from binding sites on the surface. By integration, each separate differential equation can be solved and simplified as shown in Equation A.3.

$$\gamma(t) = \mathrm{A}_1 \exp\left(-\kappa_{\mathrm{off},1} t\right) + \mathrm{A}_2 \exp\left(-\kappa_{\mathrm{off},2} t\right) \tag{A.3}$$

Lastly, the sum of the exponential coefficients A_i has to be summed to the initial value, i.e., 1. Substitution $\mathrm{A}_1 = \mathrm{A}$ and $\mathrm{A}_2 = 1 - \mathrm{A}$ results in Equation A.4. Normalised measurements during the dissociation phase can be fitted to this model to draw conclusions on the rate of dissociation and the distribution between the two modes.

$$\gamma(t) = \mathrm{A}_1 \exp\left(-\kappa_{\mathrm{off},1} t\right) + \mathrm{A}_2 \exp\left(-\kappa_{\mathrm{off},2} t\right) \tag{A.4}$$

Two-Mode Equilibrium Model

Equation 3.7 gave an expression for the equilibrium distribution at an analyte concentration of C_0 for both modes of adsorption. Derivation is based on the system of differential equations shown in Equations 3.4a and 3.4b. As the system approaches equilibrium, the time gradient approaches zero. This simplifies the system of differential equations into a system of linear equation. However, as both modes of the model are independent, they can be solved identically to the first-order model. Solving Equation 3.3 at equilibrium for $\gamma(t \to \infty)$ results in Equation A.5.

$$\gamma(t \to \infty) = \frac{C_0 \kappa_{\mathrm{on}}}{C_0 \kappa_{\mathrm{on}} + \kappa_{\mathrm{off}}} \tag{A.5}$$

Per definition, the affinity constant (KD) is the ratio of κ_{off} and κ_{on}. Substituting $\kappa_{\mathrm{off}} = \kappa_{\mathrm{on}} \times \mathrm{KD}$ in Equation A.5 allows both rate constants to be removed from the expression. The partial surface coverage $\gamma(t \to \infty)$ can further be expanded as the ratio of the total surface coverage $\Gamma(t \to \infty) \equiv \Gamma$ and the saturation limit Γ_{max}. This results in Equation A.6.

$$\frac{\Gamma}{\Gamma_{\mathrm{max}}} = \frac{C_0}{C_0 + \mathrm{KD}} \tag{A.6}$$

B

Appendix: Additional Figures

The Nuclear Transport Cycle

Figure B.1 shows a detailed schematic of the importin cycle of NLS-containing proteins and their shuttling through the NPC. In summary, importin β (Im_β) binds cargo in the cytoplasm via an importin α (Im_α) adaptor protein and transports it through the NPC, in which the Im_β can interact with the FG-repeats of the FG-Nups. In the nucleoplasm, RanGTP binds to Im_β and dissociates the trimeric complex of Im_β, Imα and cargo, which releases the cargo inside the nucleus. After the completion of the importin mechanism, Im_β and Im_α are exported back across the NPC through separate pathways and the cycle repeats.

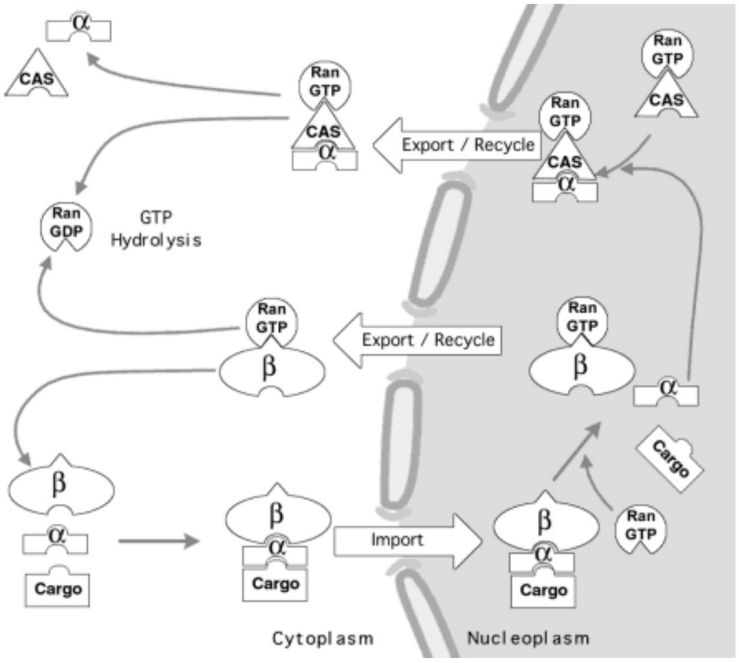

Figure B.1: Illustration of the importin cycle of NLS-containing proteins and their shuttling through the NPC. Image taken from Moroianu (1999) [16].

Chemical Structures

Figure B.2 shows the chemical structure of PMAA.

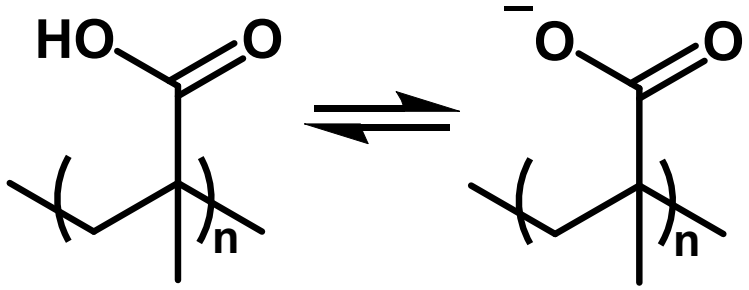

Figure B.2: Chemical structure of PMAA in its protonated state (left) and in its charged state (right).

Figure B.3 shows the chemical structure of PHEAA.

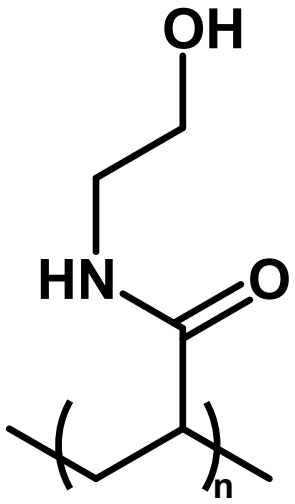

Figure B.3: Chemical structure of PHEAA.

Overlapping sensorgrams from interaction study

Figure B.4 shows the sensorgrams of injection of a solution of PMAA in PBS at various concentrations. Injections were performed at a flow rate of 100 µl/min.

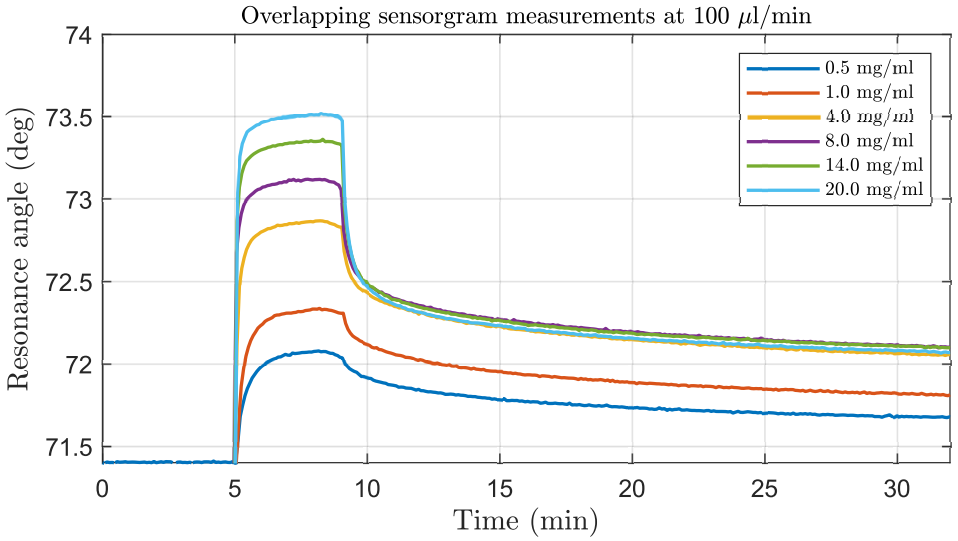

Figure B.4: Overlapping sensorgrams from PMAA injections at 100 µl/min.

Figure B.5 shows the sensorgrams of injection of a solution of PMAA in PBS at various concentrations. Injections were performed at a flow rate of 25 µl/min.

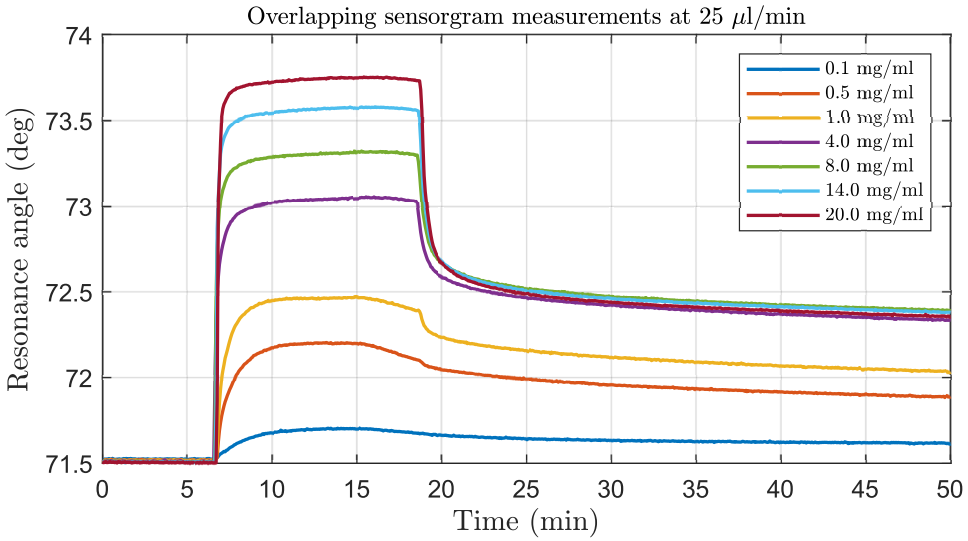

Figure B.5: Overlapping sensorgrams from PMAA injections at 25 µl/min.

Dissociation model with linear addition

Figure B.6 shows the effect of addition on a linear term to the dissociation model, and Equation B.1 shows the linear addition to the dissociation model.

$$\Gamma(t) = \mathrm{A}\exp(-\kappa_1 t) + (1-\mathrm{A})\exp(-\kappa_2 t) + \kappa_t t \tag{B.1}$$

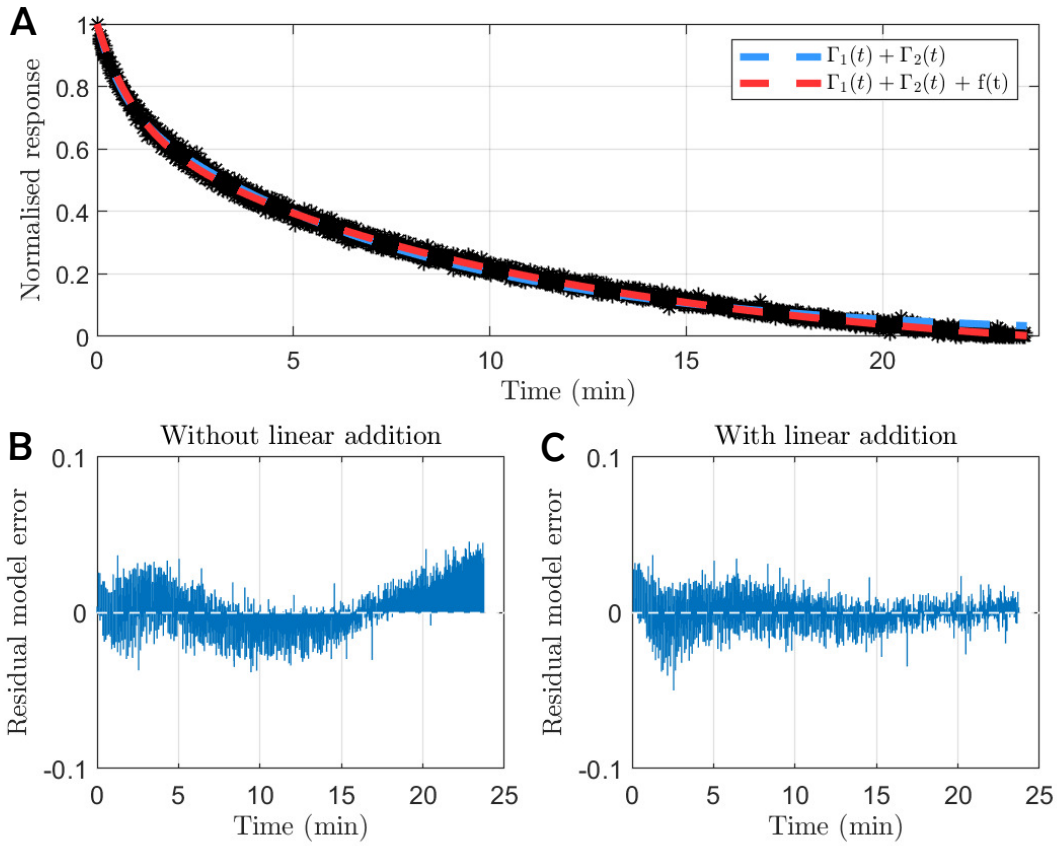

Figure B.6: Dissociation model with two modes and a linear compensation. (A) Normalised sensorgrams during the dissociative phase fitted with a two-mode model with and without an additional linear compensation. (B) Residual model errors from the two-mode model without a linear compensation. (C) Residual model-errors from the two-mode model with a linear compensation.

Table B.1 shows the model parameters of the model in Equation B.1.

Table B.1: Model parameters of the linearly compensated model.

A	κ_1 (s^{-1})	κ_2 (s^{-1})	κ_t (s^{-1})
0.6765	0.1028	1.0370	0.002404

Fluorescein fluorescence quantum yield

Figure B.7 shows the pH dependence of the fluorescence intensity and quantum fluorescence yield of Fluorescein. At lower pH's, the fluorescence quantum yield and the fluorescence intensity decreases significantly [101], and Fluorescein is therefore not as efficient to use as a fluorescent cargo at low pH as pH-insensitive fluorophores.

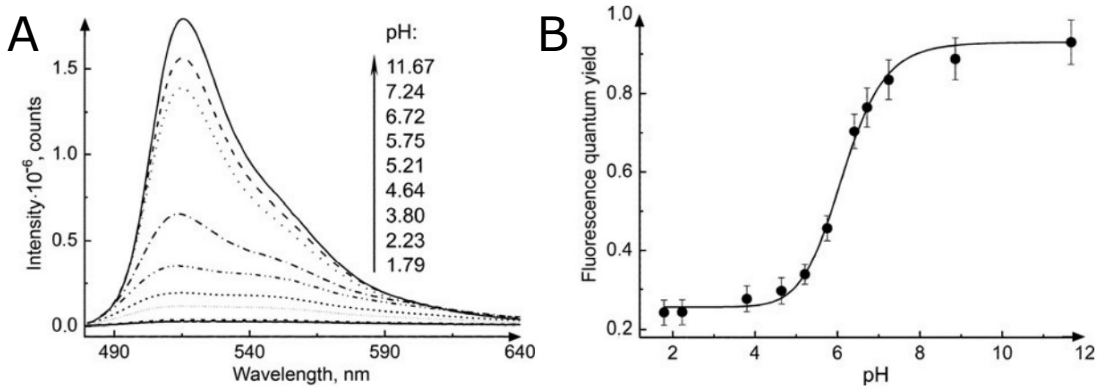

Figure B.7: Data on the fluorescence spectra and quantum yield of Fluorescein. (A) Dependence on pH on the fluorescence intensity. (B) Dependence on pH on the quantum fluorescence yield. Image taken from E. Slyusareva et al. [101].

DEPARTMENT OF CHEMISTRY AND CHEMICAL ENGINEERING
CHALMERS UNIVERSITY OF TECHNOLOGY
Gothenburg, Sweden
www.chalmers.se

CHALMERS
UNIVERSITY OF TECHNOLOGY